

AD-A124 682

THE HIGH TEMPERATURE VISCOPLASTIC FATIGUE BEHAVIOR OF A 1/2

COMPACT TENSION S. (U) AIR FORCE INST OF TECH

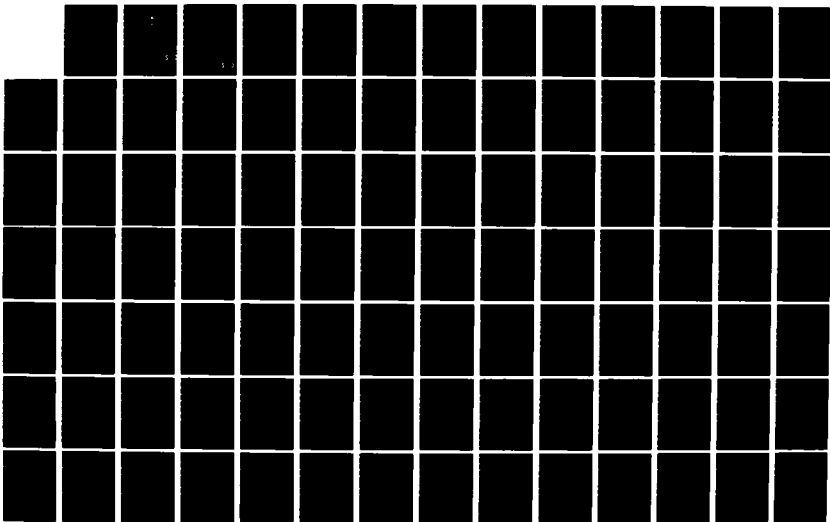
WRIGHT-PATTERSON AFB OH SCHOOL OF ENGI. J E KECK

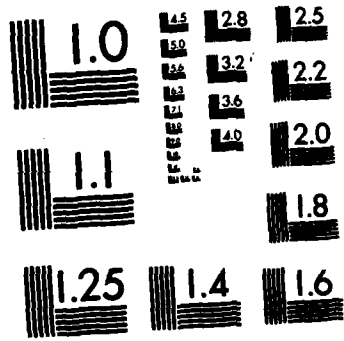
UNCLASSIFIED

DEC 82 AFIT/GAE/AA/82D-17

F/G 11/6

NL





MICROCOPY RESOLUTION TEST CHART
NATIONAL BUREAU OF STANDARDS-1963-A



1

ADA 124682

THE HIGH TEMPERATURE VISCOPLASTIC FATIGUE
BEHAVIOR OF A COMPACT TENSION SPECIMEN
USING THE BODNER-PARTOM FLOW LAW
THESIS
James E. Keck
Major USAF
FIT/GAE/AA/82D-17

DISTRIBUTION STATEMENT A
Approved for public release
Distribution Unlimited

DTIC
ELECTE
FEB 22 1983

JTC FILE COPY

DEPARTMENT OF THE AIR FORCE
AIR UNIVERSITY (ATC)
AIR FORCE INSTITUTE OF TECHNOLOGY

B

Wright-Patterson Air Force Base, Ohio

AFIT/GAE/AA/82D-17

THE HIGH TEMPERATURE VISCOPLASTIC FATIGUE
BEHAVIOR OF A COMPACT TENSION SPECIMEN
USING THE BODNER-PARTOM FLOW LAW
THESIS

James E. Keck

AFIT/GAE/AA/82D-17

Major USAF

Approved for public release; distribution unlimited.

DTIC
ELECTE
FEB 22 1983
S B D

AA
AFIT/GAE/82D-17

THE HIGH TEMPERATURE VISCOPLASTIC FATIGUE
BEHAVIOR OF A COMPACT TENSION SPECIMEN USING
THE BODNER-PARTOM FLOW LAW

THESIS

Presented to the Faculty of the School of Engineering
of the Air Force Institute of Technology
Air University

In Partial Fulfillment of the
Requirements for the Degree of
Master of Science

by

James E. Keck

Major USAF

Graduate Aerospace Engineering

December 1982

Approved for public release; distribution unlimited.

Contents

	<u>Page</u>
Acknowledgements.	iii
List of Symbols	iv-v
List of Figures	vi-ix
List of Tables.	x
Abstract.	xi
I. Introduction.	1
Approach	2
II. Viscoplasticity Theory.	4
Bodner-Partom Constitutive Model	7
III. Method of Analysis.	11
The Computer Program	11
Computer Program Verification and Uniaxial Studies	13
Computer Computational Time.	14
Compact Tension Finite Element Modeling.	15
IV. Results and Discussion.	21
Uniaxial Tests	21
Compact Tension Specimen Tests	46
V. Conclusions	95
Bibliography.	97
Appendix A: Computer Program Modifications	100
Vita.	105

Acknowledgements

I wish to express my sincere thanks and gratitude to Dr. A.N. Palazotto for his guidance during this course of study. Thanks go to Dr. T. Nicholas and Capt Michael H. Bohun of the AFVAL Materials Laboratory, for their many helpful suggestions, as well as sponsoring this study. Without the help of these individuals this study would have been fruitless.

I would especially like to thank my wife, Judy, and my daughter Cheryl. My wife provided immeasurable support and encouragement during my long hours of research. My daughter, Cheryl, kept me smiling even when things were black by wanting me to make "more discoveries". Without their support this project would have been impossible to complete.

James E. Keck

Accession For	
NTIS GRA&I	<input checked="" type="checkbox"/>
DTIC TAB	<input type="checkbox"/>
Unannounced	<input type="checkbox"/>
Justification	
By _____	
Distribution/	
Availability Codes	
Dist	Avail and/or Special
A	



List of Symbols

$(\dot{})$	Time rate of change ()
a	Crack length in compact tension specimen
C	Compliance
B	Compact tension specimen thickness
D_2^P	Second invariant of plastic strain rate
D_0	Bodner material constant
E	Elastic modulus
G	Shear modulus
H, λ	Proportionality constants
I_1, I_2, I_3	Stress invariants
i, j	Indices
J_2, J_3	Second and third invariant of deviatoric stress tensor
K	Stress intensity factor
k	Hardening parameter
m	Bodner material constant
n	Bodner material constant
p	Applied load
r	Bodner material constant
S_{ij}	Deviatoric stress
U_d	Distortion strain energy
W_p	Plastic strain energy density
Z	Bodner model internal state variable
Z_0, Z_1, Z_2	Bodner material constant

List of Symbols (Cont'd.)

ϵ	Total uniaxial strain
ϵ_{ij}	Components of total strain
ϵ_{ij}^e	Elastic components of total strain
ϵ_{ij}^p	Plastic components of total strain
σ	Uniaxial stress
σ_{ij}	Components of stress
σ_{ys}	Uniaxial material yield stress
$\dot{\epsilon}_{rec}$	Rate of work hardening recovery
Hz	Frequency cycles per second

List of Figures

<u>Figure</u>		<u>Page</u>
3.1	Typical Cyclic Load.	12
3.2	Uniaxial Finite Element Model.	13
3.3	Compact Tension Specimen Geometry.	17
3.4	Compact Tension Specimen Finite Element Mesh	18
3.5	Uniform Mesh Ahead of Crack Tip.	19
3.6	Cyclic Load Cases and Stress Intensity Factors	20
4.1	Uniaxial Stress-Strain Curve 2.5Hz 130KSI Max Stress.	22
4.2	Uniaxial Stress-Strain Curve 2.5Hz 150KSI Max Stress.	23
4.3	Uniaxial Stress-Strain Curve 2.5Hz 165KSI Max Stress.	24
4.4	Uniaxial Stress-Strain Curve 2.5Hz 180KSI Max Stress.	25
4.5	Uniaxial Stress-Strain Curve 2.5Hz 200KSI Max Stress.	26
4.6	Uniaxial Stress-Strain Curve 2.5Hz 220KSI Max Stress.	27
4.7	Uniaxial Stress-Strain Curve .167Hz 130KSI Max Stress.	28
4.8	Uniaxial Stress-Strain Curve .167Hz 150KSI Max Stress.	29
4.9	Uniaxial Stress-Strain Curve .167Hz 165KSI Max Stress.	30
4.10	Uniaxial Stress-Strain Curve .167Hz 180KSI Max Stress.	31
4.11	Uniaxial Stress-Strain Curve .167Hz 200KSI Max Stress.	32
4.12	Uniaxial Stress-Strain Curve .167Hz 220KSI Max Stress.	33
4.13	Uniaxial Stress-Strain Curve .03Hz 130KSI Max Stress.	34

List of Figures (Cont'd.)

<u>Figure</u>		<u>Page</u>
4.14	Uniaxial Stress-Strain Curve .03Hz 150KSI Max Stress.	35
4.15	Uniaxial Stress-Strain Curve .03Hz 165KSI Max Stress.	36
4.16	Uniaxial Stress-Strain Curve .03Hz 180KSI Max Stress.	37
4.17	Uniaxial Stress-Strain Curve .03Hz 200KSI Max Stress.	38
4.18	Uniaxial Stress-Strain Curve .03Hz 220KSI Max Stress.	39
4.19	Z Hardness vs. Time .03Hz	41
4.20	Z Hardness vs. Time 2.5 Hz	42
4.21	Z Hardness vs. Time .167Hz.	43
4.22	Plastic Strain vs. Time 2.5Hz	45
4.23	Effective Stress vs. Total Strain at the Crack Tip 2.5Hz $K=45\text{KSI}\sqrt{\text{in}}$	49
4.24	Effective Stress vs. Total Strain at the Crack Tip 2.5Hz $K=35\text{KSI}\sqrt{\text{in}}$	50
4.25	Effective Stress vs. Total Strain at the Crack Tip .167Hz $K=35\text{KSI}\sqrt{\text{in}}$	51
4.26	Effective Stress vs. Total Strain at the Crack Tip .03Hz $K=35\text{KSI}\sqrt{\text{in}}$	52
4.27	Y Stress vs. Distance Ahead of Crack Tip 2.5Hz $K=45\text{KSI}\sqrt{\text{in}}$	53
4.28	Y Strain vs. Distance Ahead of Crack Tip 2.5Hz $K=45\text{KSI}\sqrt{\text{in}}$	54
4.29	Z Hardness vs. Distance Ahead of Crack Tip 2.5Hz $K=45\text{KSI}\sqrt{\text{in}}$	55
4.30	Y Stress vs. Distance Ahead of Crack Tip 2.5Hz $K=35\text{KSI}\sqrt{\text{in}}$	56
4.31	Y Strain vs. Distance Ahead of Crack Tip 2.5Hz $K=35\text{KSI}\sqrt{\text{in}}$	57
4.32	Z Hardness vs. Distance Ahead of Crack Tip 2.5Hz $K=35\text{KSI}\sqrt{\text{in}}$	58

List of Figures (Cont'd.)

<u>Figure</u>		<u>Page</u>
4.33	Y Stress vs. Distance Ahead of Crack Tip .167Hz $K=35\text{KSI}/\sqrt{\text{in}}$	59
4.34	Y Strain vs. Distance Ahead of Crack Tip .167Hz $K=35\text{KSI}/\sqrt{\text{in}}$	60
4.35	Z Hardness vs. Distance Ahead of Crack Tip .167Hz $K=35\text{KSI}/\sqrt{\text{in}}$	61
4.36	Y Stress vs. Distance Ahead of Crack Tip .03Hz $K=35\text{KSI}/\sqrt{\text{in}}$	62
4.37	Y Strain vs. Distance Ahead of Crack Tip .03Hz $K=35\text{KSI}/\sqrt{\text{in}}$	63
4.38	Z Hardness vs. Distance Ahead of Crack Tip .03Hz $K=35\text{KSI}/\sqrt{\text{in}}$	64
4.39	Y Stress vs. Distance Ahead of Crack Tip Considering Overstress.	65
4.40	Y Strain vs. Distance Ahead of Crack Tip Considering Overstress.	66
4.41	Z Hardness vs. Distance Ahead of Crack Tip Considering Overstress.	67
4.42	Y Displacement vs. Distance Behind Crack Tip During Unload 2.5Hz $K=35\text{KSI}/\sqrt{\text{in}}$	68
4.43	Y Displacement vs. Distance Behind Crack Tip During Unload 2.5Hz $K=35\text{KSI}/\sqrt{\text{in}}$	69
4.44	Y Displacement vs. Distance Behind Crack Tip During Unload .167Hz $K=35\text{KSI}/\sqrt{\text{in}}$	70
4.45	Y Displacement vs. Distance Behind Crack Tip During Unload .03Hz $K=35\text{KSI}/\sqrt{\text{in}}$	71
4.46	Average Effective Stress vs. Average Total Strain Near Crack Tip 2.5Hz $K=35\text{KSI}/\sqrt{\text{in}}$	73
4.47	Average Effective Stress vs. Average Total Strain Near Crack Tip .03Hz $K=35\text{KSI}/\sqrt{\text{in}}$	74
4.48	Elastic Zone After 0.5 Cycles 2.5Hz $K=35\text{KSI}/\sqrt{\text{in}}$	76

List of Figures (Cont'd.)

<u>Figure</u>		<u>Page</u>
4.49	Plastic Zone After 2.5 Cycles 2.5Hz $K=35\text{KSI}/\sqrt{\text{in.}}$	77
4.50	Plastic Zone After 15 Minute Hold Period $K=35\text{KSI}/\sqrt{\text{in.}}$	78
4.51	Plastic Zone After Node Release $K=35\text{KSI}/\sqrt{\text{in.}}$	79
4.52	Y Stress vs. Distance Ahead of Crack Tip After 15 Minute Hold $K=35\text{KSI}/\sqrt{\text{in.}}$	80
4.53	Y Strain vs. Distance Ahead of Crack Tip After 15 Minute Hold $K=35\text{KSI}/\sqrt{\text{in.}}$	81
4.54	Z Hardness vs. Distance Ahead of Crack Tip After 15 Minute Hold $K=35\text{KSI}/\sqrt{\text{in.}}$	82
4.55	Plastic Zone After 0.5 Cycles 2.5Hz $K=45\text{KSI}/\sqrt{\text{in.}}$	83
4.56	Plastic Zone After 2.5 Cycles 2.5Hz $K=45\text{KSI}/\sqrt{\text{in.}}$	84
4.57	Plastic Zone After 0.5 Cycles .167Hz $K=35\text{KSI}/\sqrt{\text{in.}}$	85
4.58	Plastic Zone After 2.5 Cycles .167Hz $K=35\text{KSI}/\sqrt{\text{in.}}$	86
4.59	Plastic Zone After 0.5 Cycles .03Hz $K=35\text{KSI}/\sqrt{\text{in.}}$	87
4.60	Plastic Zone After 2.5 Cycles .03Hz $K=35\text{KSI}/\sqrt{\text{in.}}$	88
4.61	Crack Mouth Displacement vs. Percent Load 2.5Hz $K=45\text{KSI}/\sqrt{\text{in.}}$	90
4.62	Crack Mouth Displacement vs. Percent Load 2.5Hz $K=35\text{KSI}/\sqrt{\text{in.}}$	91
4.63	Crack Mouth Displacement vs. Percent Load .167Hz $K=35\text{KSI}/\sqrt{\text{in.}}$	92
4.64	Crack Mouth Displacement vs. Percent Load .03Hz $K=35\text{KSI}/\sqrt{\text{in.}}$	93

List of Tables

<u>Table</u>		<u>Page</u>
2.1	Bodner Coefficients for In-100 At 1350°F.	10
3.1	Uniaxial Test Loads and Frequencies	13
3.2	Compact Tension Specimen Loads and Stress Intensity Factors	16

Abstact

↓

Few studies have been made concerning the effects of low cycle fatigue on the stress/strain field or the plastic zone size ahead of a crack tip in a high temperature environment. Experiments using a superalloy IN-100 at 732°C have shown crack growth during fatigue is slower than the growth rate during long periods of sustained load. These investigations also show that crack growth rates during hold periods after fatigue cycling are dependent on the cycle frequency.

This study focuses on fatigue as it effects the changing stress field and plastic zone ahead of a crack tip. Finite element modeling was accomplished using an in-house computer program named VISCO, which was modified to incorporate load cycling. A compact tension specimen geometry was modeled using the Bodner-Partom viscoplastic constitutive equations to describe the material behavior. Load spectra consisted of constant amplitude saw toothed patterns with non-zero mean load having a ratio of minimum to maximum load of 0.1.

→ Results show that material behavior near a crack tip closely correlates to uniaxial material response data under stress controlled loading. During cyclic loading, the greatest plastic deformation near the crack tip occurs in the first load cycle. Computations show that IN-100 displays significant amounts of time dependent inelastic behavior.

↑

I. INTRODUCTION

With the growing use of high performance military gas turbine engines and the escalating cost of aircraft, the United States Air Force places stringent service limits on critical airframe and engine components.

Airframe components are periodically inspected for flaws and returned to service if the flaws can not grow to critical size prior to the next periodic inspection. Critical engine components, however, such as turbine disks, are removed from service at a time when statistically 1 in 1000 would be expected to have initiated a crack of some finite length (0.03 in). Eighty percent of the disks have at least ten useful lifetimes remaining, though no attempt is made to utilize the statistically "failed" disks [2].

Engine operation occurs in a complex region characterized by frequent load cycle excursions and short periods of sustained loading. High temperature engine operation introduces time dependent phenomena which interact with varied load spectra to produce complex material behavior. The thrust of the Air Force research has focused on crack growth prediction with lesser emphasis on the interaction of fatigue cycling and sustained hold times. If the effects of frequency on fatigue cycling and load amplitude are fully understood when coupled with sustained hold times, accurate remaining life predictions could be made for components with subcritical flaws. Many retired parts could be kept in service. Only components with a quantifiable critical flaw size would be Retired-for-Cause [14].

Approach

This thesis attempts to quantify fatigue crack growth and the effects of cyclic loading on IN-100, a superplastically forged Nickel-based superalloy used in turbine disks for the F-100 engine. Comparisons between laboratory low-cycle fatigue tests and computer generated viscoplastic cyclic effects are directed at the change of material parameters with frequency, load, and plastic strain. The coupling of high temperatures and stresses causes time dependent plastic deformation at discontinuities in the material. Due to its independence of yield criteria and its close correlation with experimental observations of IN-100, plastic flow near these discontinuities was modeled using the Bodner-Partom flow law. In addition, the Bodner-Partom model has the capability to predict behavior produced by cyclic effects, time dependent creep, strain hardening, and plastic deformation. Thus, laboratory low-cycle fatigue tests, performed on compact tension specimens manufactured from typical disk forgings, were modeled using finite element methods and the Bodner-Partom viscoplastic flow law.

A linear Euler extrapolation scheme was used to integrate the flow law through time and incorporated into the finite element model incorporating the residual force technique [7].

VISCO, a computer program developed by Hinnerichs [7] and used in this thesis, uses constant strain triangular elements and simulates crack growth by releasing fixed nodes at a predetermined time. As the node is released, nodal forces are redistributed to the surrounding elements and the boundary changed from one of restraint to a force

boundary condition. Costly matrix factorization is avoided by incorporating a Gauss-Seidel iteration equation solver, in which pertinent terms of the stiffness matrix are the only ones changed between time steps [7]. A cyclic load algorithm was used to accommodate the changing load spectra. The fatigue stress spectrum was modeled by a saw-toothed stress-time pattern of constant amplitude with a non-zero mean load and a load ratio of .1 [14]. During each time step; stress, strain, plastic work and z hardness parameter was calculated for each element in the model.

II. VISCOPLASTICITY THEORY

In the usual sense, plasticity is defined as permanent deformation by the application of stresses which are greater than those stresses required to cause yielding. The distortion depends not only on the final state of stress, but also upon the stress state from the start of yielding [12]. Thus, plastic behavior can be characterized by irreversible straining. All materials exhibit some plastic behavior, even when the applied loads produce stress below the yield stress. Most plastic deformation below the yield stress is small; and as such, is usually neglected [16].

The total strain a material experiences can be represented by the expression

$$\epsilon_{ij} = \epsilon_{ij}^e + \epsilon_{ij}^p \quad (2.1)$$

where ϵ_{ij} is the total strain, ϵ_{ij}^e is the elastic (reversible) strain and ϵ_{ij}^p is the plastic (irreversible) strain. Viscoplastic (non-recoverable) strains occur only after the yield stress is exceeded.

If one takes a time derivative of equation (2.1), a rate dependent form for total strain is obtained

$$\dot{\epsilon}_{ij} = \dot{\epsilon}_{ij}^e + \dot{\epsilon}_{ij}^p \quad \text{where } \dot{\epsilon}_{ij} = \frac{d\epsilon}{dt} \quad (2.2)$$

By taking a time derivative of Hooke's law, the elastic strain rate $\dot{\epsilon}_{ij}^e$ can be related to the stress rate; however, it is necessary to relate the plastic strain rate to stress by some other means.

In classical theory, plastic deformation begins at yield, and is dependent on a yield criterion. General yield criteria can be written

as

$$f(\sigma_{ij}) = K(k) \quad (2.3)$$

where f is some function of stress, K is a material parameter determined experimentally and k is a hardening parameter. The yield criteria as used herein is independent of coordinate orientation and only a function of the three stress invariants [13].

$$I_1 = \sigma_{ij} \quad (2.4)$$

$$I_2 = \frac{1}{2} \sigma_{ij} \sigma_{ij} \quad (2.5)$$

$$I_3 = \frac{1}{3} \sigma_{ij} \sigma_{jk} \sigma_{ki} \quad (2.6)$$

Through experimental studies by Bridgman, plastic deformation is independent of hydrostatic stress. Thus, the yield function can be written as $f(J_2, J_3) = K(k)$ where J_2 and J_3 are the second and third invariants of the deviatoric stress tensor.

$$J_2 = \frac{1}{2} S_{ij} S_{ij} \quad (2.7)$$

and

$$S_{ij} = \sigma_{ij} - \frac{1}{3} \sigma_{ij} \sigma_{kk} \quad (2.8)$$

Many forms of yield criteria have been developed. Each predicts plastic flow under different conditions and materials. The Von Mises yield criterion is one of these. It is used primarily for metals behavior and is based on distortion strain energy theory [13]. Yielding begins when the distortion strain energy equals the distortion strain energy required to produce yielding in a simple uniaxial stress test.

The distortion strain energy can be written

$$U_d = \int_V \frac{1}{2} \sigma_{ij} d\epsilon_{ij} dv \quad (2.9)$$

or in terms of J_2 , the second invariant of deviatoric stress

$$U_d = \frac{1}{2G} J_2 \quad (2.10)$$

where G is the shear modulus.

In explicit terms of principal stresses, the above expressions become

$$J_2 = \frac{1}{6} (\sigma_1 - \sigma_2)^2 + (\sigma_2 - \sigma_3)^2 + (\sigma_1 - \sigma_3)^2 \quad (2.11)$$

$$U_d = \frac{1}{12G} (\sigma_1 - \sigma_2)^2 + (\sigma_2 - \sigma_3)^2 + (\sigma_1 - \sigma_3)^2 \quad (2.12)$$

For a uniaxial test

$$\sigma_1 = \sigma_{ys} \quad \sigma_2 = \sigma_3 = 0 \quad (2.13)$$

where σ_{ys} equals the stress at the start of yielding.

J_2 reduces to

$$J_2 = \frac{1}{3} \sigma_{ys}^2 \quad (2.14)$$

where σ_{ys} is the uniaxial yield stress.

The distortion strain energy becomes

$$U_d = \frac{1}{6G} \sigma_{ys}^2 \quad (2.15)$$

Equating the multiaxial distortion strain energy to that of the uniaxial case produces

$$J_2 = K \sigma_{ys}^2 \quad (2.16)$$

where K is a proportionality constant. Multiaxial yielding is predicted when J_2 reaches the critical value at yield in a uniaxial stress test.

Using the Prandtl-Reuss relations, which assume incompressibility and isotropy, the plastic strain ϵ_{ij}^P can be expressed incrementally as

$$d\epsilon_{ij}^P = d\lambda S_{ij} \quad (2.17)$$

where λ is a positive load history dependent proportionality constant relating the material viscosity and S_{ij} are the components of the deviatoric stress tensor. If given a form for $d\lambda$, the plastic strain ϵ_{ij}^P can be found for any state of stress. It can be shown that, at yield, the Prandtl-Reuss relations imply the Von Mises yield criterion [13]. The specific expression for $d\lambda$ depends upon the plastic flow law used.

Bodner-Partom Constitutive Model

Bodner and Partom [3,4,5] suggested that plastic flow begins at the onset of loading, and as such, a continuous flow relationship exists between plastic strain and stress. Through the study of dislocation dynamics Bodner and Partom postulated the form of the parameter λ by squaring the Prandtl-Reuss relation

$$\dot{\epsilon}_{ij}^P = \lambda S_{ij} \quad (2.18)$$

resulting in

$$\frac{1}{2} \dot{\epsilon}_{ij}^P \dot{\epsilon}_{ij}^P = D_2^P = \frac{1}{2} \lambda^2 S_{ij} S_{ij} = \lambda^2 J_2 \quad (2.19)$$

where D_2^P is the second invariant of the plastic strain rate, and J_2 is the second invariant of the deviatoric stress tensor.

Bodner and Partom expressed D_2^P as follows:

$$D_2^P = D_0^2 \exp \left[- \left(\frac{J_2^2}{3J_2} \right)^n \frac{n+1}{n} \right] \quad (2.20)$$

where D_0 is the limiting value of plastic strain rate in shear, Z is the measure of material hardening, and n is a constant controlling strain rate sensitivity.

Being strain rate sensitive and independent of a specific yield surface, the Bodner-Partom flow law allows plastic deformation during unloading. This is a significant departure from classical plasticity theory where all unload sequences are accomplished elastically. The strain rate sensitivity exponent (n) influences the level of the stress-strain curves. Decreasing the value of n results in increased strain rate sensitivity and spreads the stress strain curves. It should be pointed out that the strain rate sensitivity exponent (n) is a material constant and independent of load history [4].

Thus, the Bodner-Partom model, henceforth called the Bodner model, accounts for both isotropic and kinematic hardening and is capable of representing cyclic load effects.

Bodner's Z hardness parameter can be interpreted as a macroscopic hardening function which controls resistance to plastic flow. Being deformation history dependent, the Z parameter is assumed to be a function of plastic work:

$$Z = Z(W_p) \quad (2.21)$$

where W_p is the relative amount of plastic work done from some initial state. This work function takes the form:

$$W_p = \int S_{ij} \dot{\epsilon}_{ij}^p dt = 2(D_{2J_2}^p)^{\frac{1}{2}} \quad (2.22)$$

The hardness parameter Z now becomes

$$Z = Z_1 - (Z_1 - Z_0) \exp [-mW_p] \quad (2.23)$$

where Z_1 is the maximum value of hardness, Z_0 represents the initial value of hardness from which plastic work is measured, and m is the hardening rate exponent.

Most materials exhibit some thermal recovery of hardening or relaxation of accumulated plastic work at high temperatures. In order to model this behavior, the form of plastic work must be redefined as

$$W_p = \int S_{ij} \dot{\epsilon}_{ij}^p dt + \int \frac{\dot{Z}_{rec}}{m(Z_1 - Z)} dt \quad (2.24)$$

where

$$\dot{Z}_{rec} = -A \left(\frac{Z - Z_2}{Z_1} \right)^r Z_1 \quad (2.25)$$

Z_2 is the stable non-work hardened value of Z at a given temperature. A and r are material constants picked to match creep test data. The thermal hardening recovery term (\dot{Z}_{rec}) of Eq. 2.25 is always negative due to the negative sign on A , since Z is always greater than or equal to Z_2 . A balanced condition exists when the rate of work hardening equals the rate of hardening recovery. At high strain rates, Z hardness reaches its saturation value Z_1 quickly and a steady state condition is realized.

Stouffer experimentally developed the nine (9) Bodner Material parameters for IN-100 at 1350°F [6] and are presented in Table 2.1.

TABLE 2.1
BODNER COEFFICIENTS FOR IN-100 AT 1350°F

Material Parameter	Description	Value
E	Elastic modulus	26.3x10 ² KSI (18.133x10 ⁴ MPa)
n	Strain rate exponent	0.7
D ₀	Limiting value of strain rate	10 ⁴ sec
Z ₀	Limiting value of hardness	915.0KSI (6304 MPa)
Z ₁	Maximum value of hardness	1015.0KSI (6993 MPa)
Z ₂	Minimum value of hardness	600.0KSI (4134 MPa)
m	Hardening rate exponent	2.57KSI ⁻¹ (.37273 MPa ⁻¹)
A	Hardening recovery coefficient	1.9x10 ⁻³ sec ⁻¹
r	Hardening recovery exponent	2.56

(1 KBAR = 100 MPa = 14.504KSI)

III. METHODS OF ANALYSIS

The Computer Program

An analytical computer program of known accuracy named VISCO was used throughout this study. VISCO is a two-dimensional finite element code employing constant strain triangular elements for both plane stress and plane strain solutions.

The Bodner-Partom viscoplastic constitutive equations are solved using the Gauss-Seidel iterative equation solver with overrelaxation, eliminating costly stiffness matrix factorization and allowing terms of the stiffness matrix to be changed as nodes are released simulating crack growth. VISCO employs the residual force technique using an elastic stiffness matrix for the entire analysis. Plasticity is treated as an applied load used in conjunction with thermal and applied mechanical loads for equilibrium. During each time step, equilibrium tolerances are checked. If the tolerances are exceeded, the time step is reduced until equilibrium is obtained. Time integration of the Bodner equations is accomplished for each element using a Euler extrapolation scheme [7].

To accurately model cyclic material behavior within an aircraft gas-turbine engine, it is necessary to understand the duty cycle of the engine. The duty cycle can be characterized by frequent load cycles and long dwell times. In addition, few rotating jet engines components are subjected to compressive loading. With this in mind, the engine cyclic load spectrum can be represented as a saw-toothed constant amplitude load-time pattern with non-zero mean stress and a positive stress ratio as shown in Fig. 3.1.

Frequencies for this type of operation generally range from .01 Hz to 5 Hz, which corresponds to experimental test data collected by Nicholas and Larsen for use on another project [14].

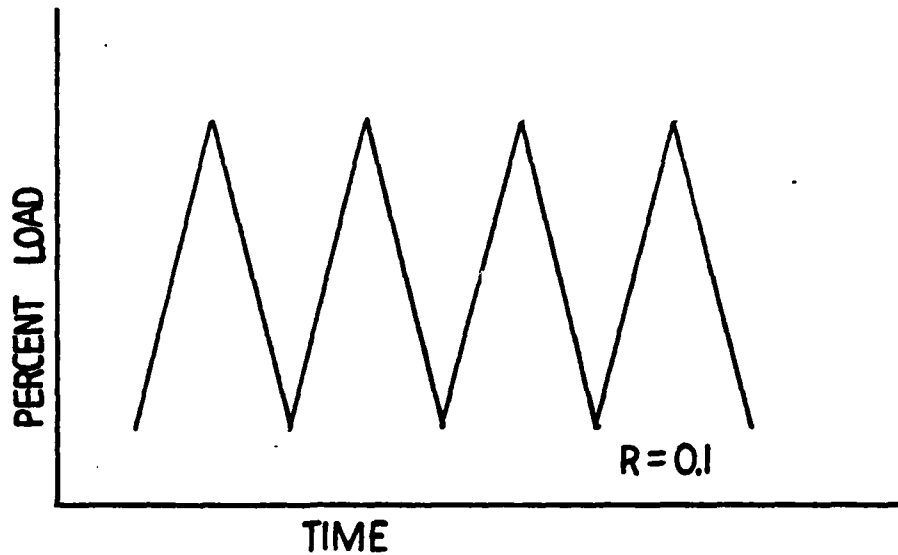


Fig 3.1 Typical Cyclic Load

VISCO's loading function was modified for cyclic response (see Appendix A). Using a ramp function to model the load spectrum in Fig. 3.1, a percentage of total load was calculated at each timestep. Element stress, strain, and Bodner Z hardness were recovered at each load percentage. The load rates were matched to the half-cycle period of the saw-toothed load function. VISCO normally loads the specimen at the rate of 20 percent of total load per second. In order to match the cyclic load spectra, load rates were matched to the cyclic half period. For example, at 2.5Hz, the cyclic half period is .2 seconds. The load varies from a minimum to peak value in .2 seconds, resulting in a 500% load rate. This technique graphically depicts incremental fatigue effects as well as the change in stress field at a crack tip. In addition, modifications to VISCO were made to stop load cycling at

a predetermined time and hold the load at a constant stress intensity factor (K).

Computer Program Verification and Uniaxial Studies

To verify proper program operation and to determine IN-100 uniaxial non-linear response to cyclic loading, a two triangular finite element model, shown in Fig 3.2, was used in VISCO. Plane stress solutions were obtained for each frequency and load shown in Table 3.1.

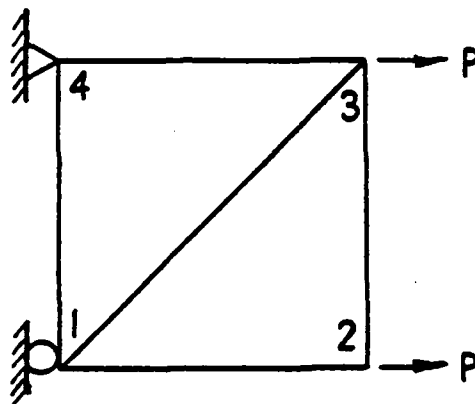


Fig 3.2 Uniaxial Finite Element Model

TABLE 3.1

UNIAXIAL TEST LOADS AND FREQUENCIES

<u>Test Frequency (Hz)</u>	<u>Stress (psi)</u>
2.50	130,000
0.167	150,000
0.03	165,000
0.03	180,000
0.03	200,000
0.03	220,000

Peak load stress levels represent typical values expected at the crack tip for a compact tension specimen while the lowest load/stress level (130KSI) represents the experimental yield stress of IN-100 at 732°C.

Each of the eighteen uniaxial cases was allowed to run for fifteen complete load cycles. Results showed that the computer solutions followed the input load cycle at each time step and that calculated stress values were accurate. Plastic deformation calculations compared favorably with predicted values.

Computer Computational Time

It was originally intended to match laboratory fatigue tests done by Larsen and Nicholas with computer generated fatigue data [14]. This necessitated at least 8,000 load cycles before going into a sustained hold period. Preliminary computer runs using the finite element mesh shown in Fig. 3.4 at a frequency of 2.5Hz required 2,000 seconds central processor time per run on the CDC 6600 computer for 5 complete load cycles. With optimum timestepping, it would take 14 to 18 hours to accomplish 8,000 load cycles of central processor time. Increasing the size of the finite element mesh (reducing the number of elements) doubled the number of load cycles possible, but could not provide critical stress, strain and Z hardness values near the crack tip.

With these computational restrictions in mind, it was decided to model the cyclic fatigue effects through 4 load cycles and compare results with uniaxial computations. Changes in the stress, strain, and Z hardness could be closely monitored with each cycle and changes observed.

Two-Dimensional Compact Tension Finite Element Modeling

Two-dimensional fatigue modeling was accomplished using a standard compact tension specimen geometry as shown in Fig. 3.3.

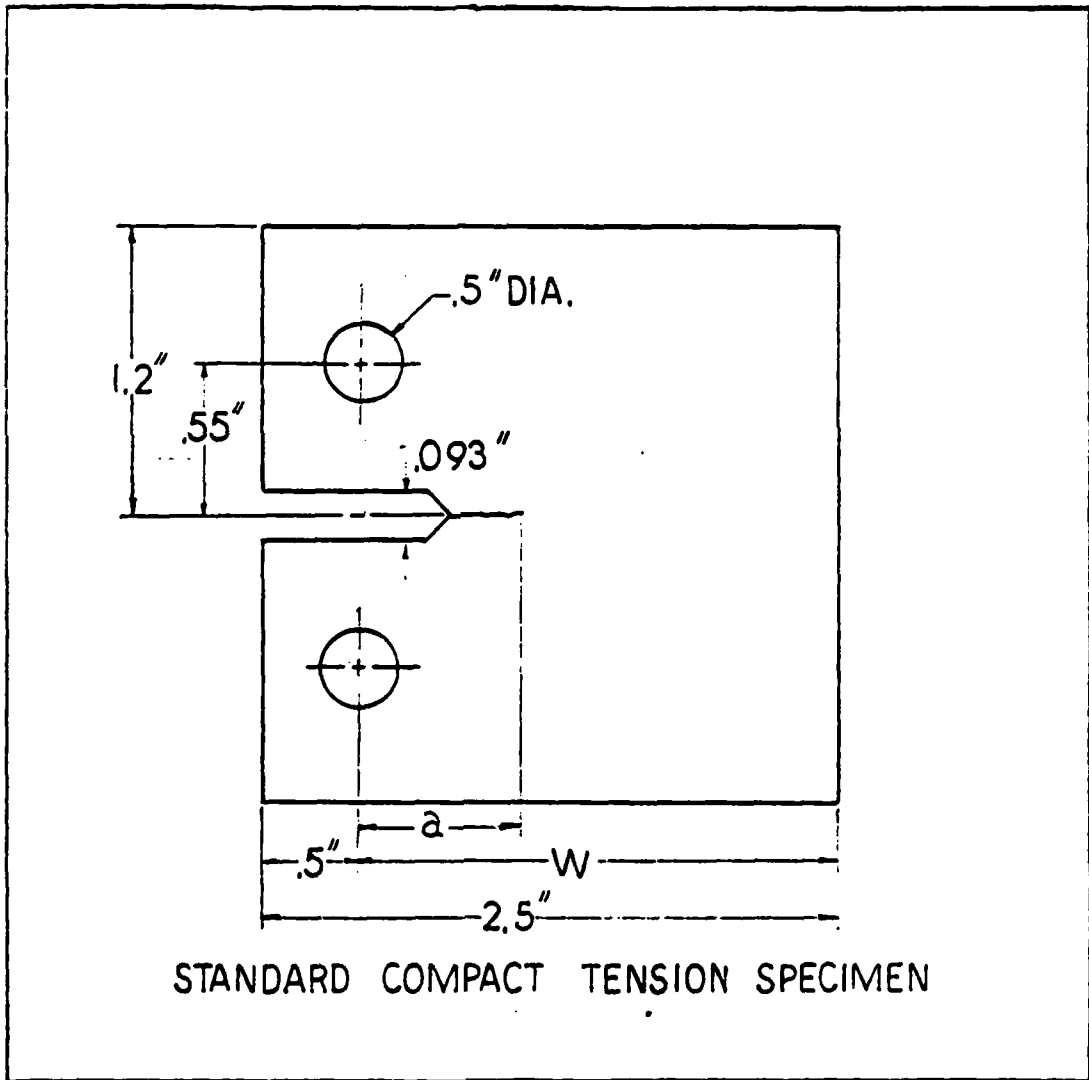
Due to symmetry, only half of the compact tension specimen was modeled using constant strain triangular elements. The finite element mesh (543 elements and 327 nodes) is shown in Fig's. 3.4 and 3.5 and is identical to mesh 3 used by Smail for compact tension specimens of the same geometry [16]. This pattern allows unlimited element size reductions and insures that no two adjacent elements differ in size by more than a factor of 2 [8]. Except for elements near the loading pin holes, element aspect ratios varied from 0.5 to 1.0. Elements near the crack tip had an area of $4.8848 \times 10^{-6} \text{ in}^2$ ($3.1494 \times 10^{-5} \text{ cm}^2$).

Since acceptable accuracy validation was performed by Smail [15] using the same computer program (VISCO) and finite element mesh, no extensive accuracy tests were carried out herein. Five cyclic load cases, with specified stress intensity factors shown in Fig. 3.6, were studied. Cyclic stress levels at the crack tip were compared with monotonic computer runs made by Smail at the same load and stress intensity factor (see Table 3.2).

TABLE 3.2

COMPACT TENSION SPECIMEN LOADS AND STRESS INTENSITY FACTORS

Stress Intensity Factor KSI $\sqrt{\text{in}}$	Load lbs.	Crack Length Inches	Specimen Thickness Inches
35	1762	.6630	.2154
45	2265	.6630	.2154



STANDARD COMPACT TENSION SPECIMEN

Fig 3.3 Compact Tension Specimen Geometry

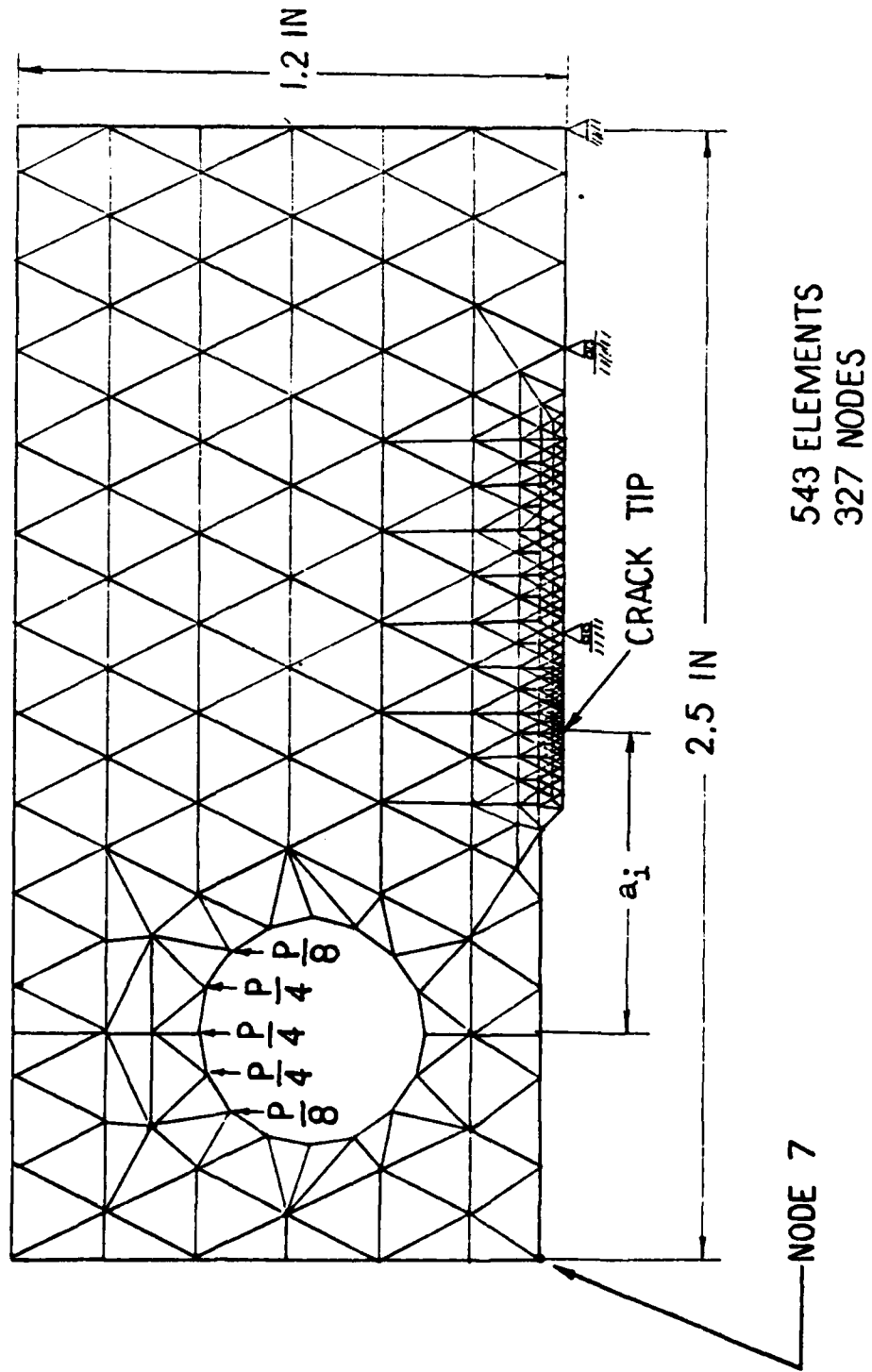


Fig 3.4 Compact Tension Specimen Finite Element Mesh

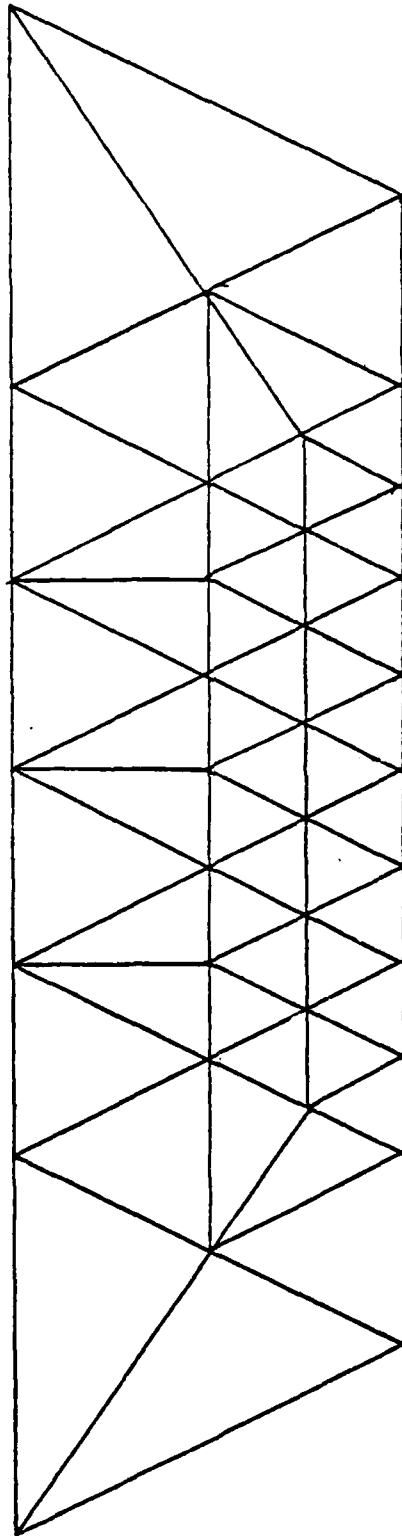
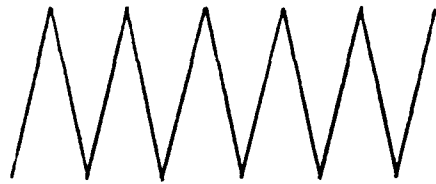


Fig. 3.5 Uniform Mesh Ahead of Crack Tip

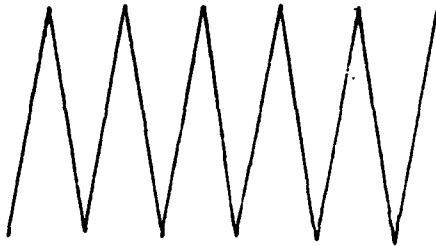


BASELINE NO DAMAGE
 $K = 35 \text{ KSI} \sqrt{\text{IN}}$

$R = 0.1$ FOR ALL CYCLING



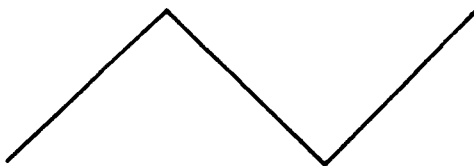
2.5 HZ
 $K = 35 \text{ KSI} \sqrt{\text{IN}}$



2.5 HZ
 $K = 45 \text{ KSI} \sqrt{\text{IN}}$



.167 HZ
 $K = 35 \text{ KSI} \sqrt{\text{IN}}$



.03 HZ
 $K = 35 \text{ KSI} \sqrt{\text{IN}}$

Fig 3.6 Cyclic Load Cases and Stress Intensity Factors

IV. RESULTS AND DISCUSSION

At 2.5Hz with stress levels at or below 165KSI (see Fig's. 4.1-4.3), the uniaxial model behaved elastically. After approximately 2.5 cycles, the stress strain curve loops became coincident. A quasi-stable steady state had been reached in as little as 2.5 load cycles. Stress levels above 165KSI caused rapid plastic deformation, especially during the first load cycle. Subsequent load cycles produced constant amounts of inelastic straining as shown in Fig's. 4.4-4.6. No stable solution existed for these stress levels.

As load cycle frequency decreased no stable-elastic material behavior was noted for stress levels above 130KSI. See Fig's. 4.7-4.18. However, for all cases above, the greatest plastic deformation always occurred during the first load cycle. Subsequent cycling produced constant plastic deformation.

All stress-strain curves displayed linear elastic behavior below 130KSI stress levels. Plastic flow appeared to start near the material yield stress (130KSI nominal value) in all cases. Using this value as a reference yield stress, specimens cycled at .03Hz spent 82 times longer above the reference value than the specimen at 2.5Hz. Thus, it was expected that time dependent inelastic deformation was dependent on the inverse of the load cycle frequency.

As shown in Fig's. 4.19-4.21, Z hardness is very sensitive to both frequency and load level. At 2.5Hz, Z hardness increased slowly at stress levels below 165KSI, while rather rapid increases were noted at lower frequencies. Increasing the stress level caused rapid rises in Z hardness. Z hardness saturation occurred after 3 cycles in all cases for

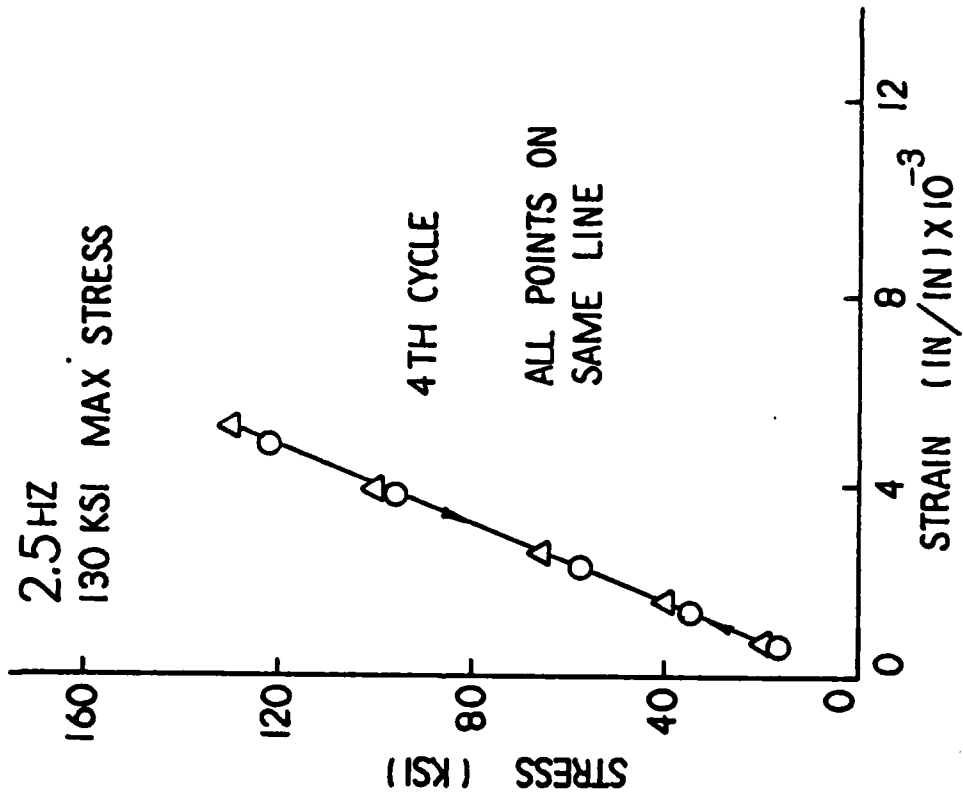


Fig 4.1 Uniaxial Stress-Strain Curve 2.5Hz

130KSI Max Stress

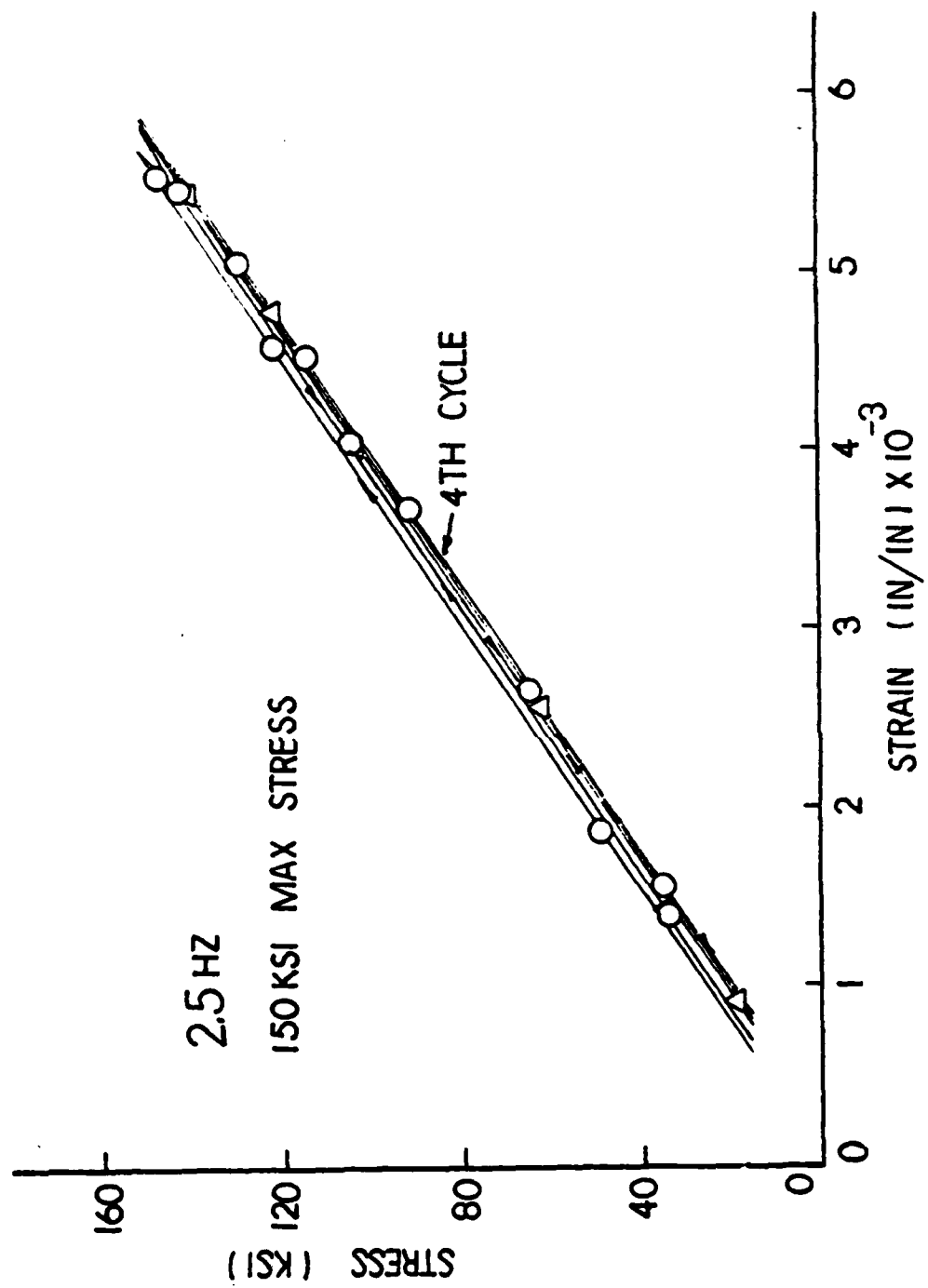


Fig 4.2 Uniaxial Stress-Strain Curve

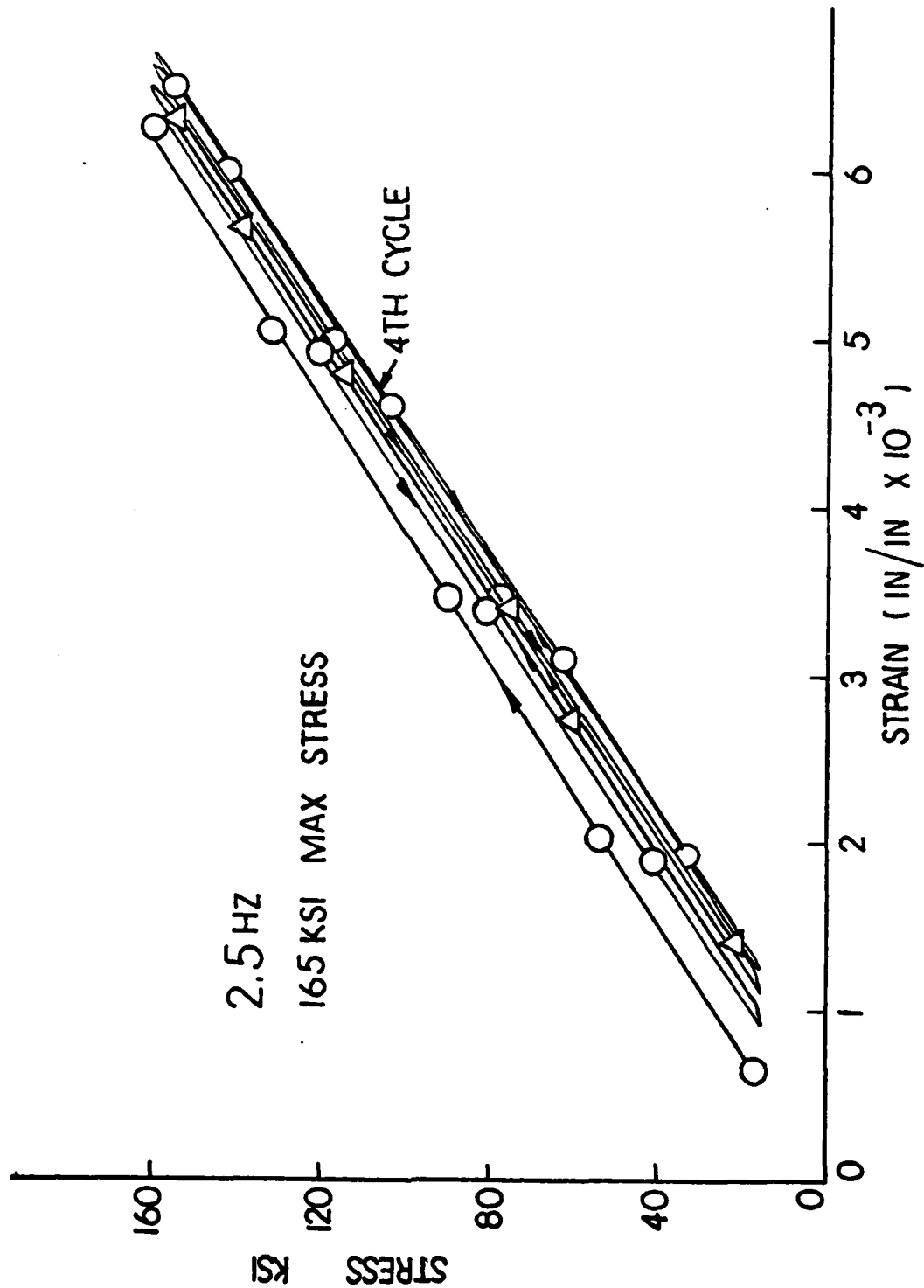


Fig 4.3 Uniaxial Stress-Strain Curve

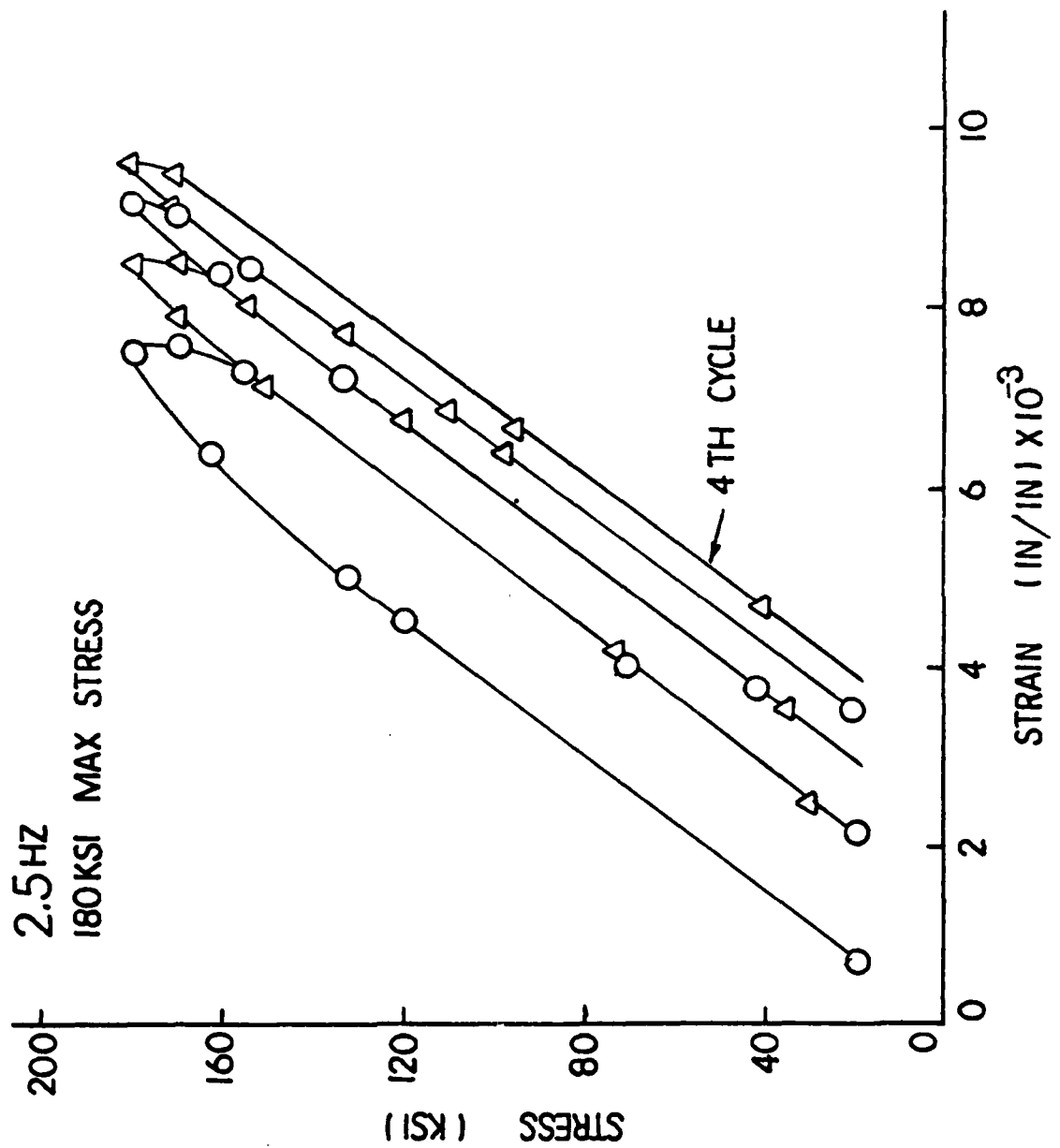


Fig 4.4 Uniaxial Stress-Strain Curve

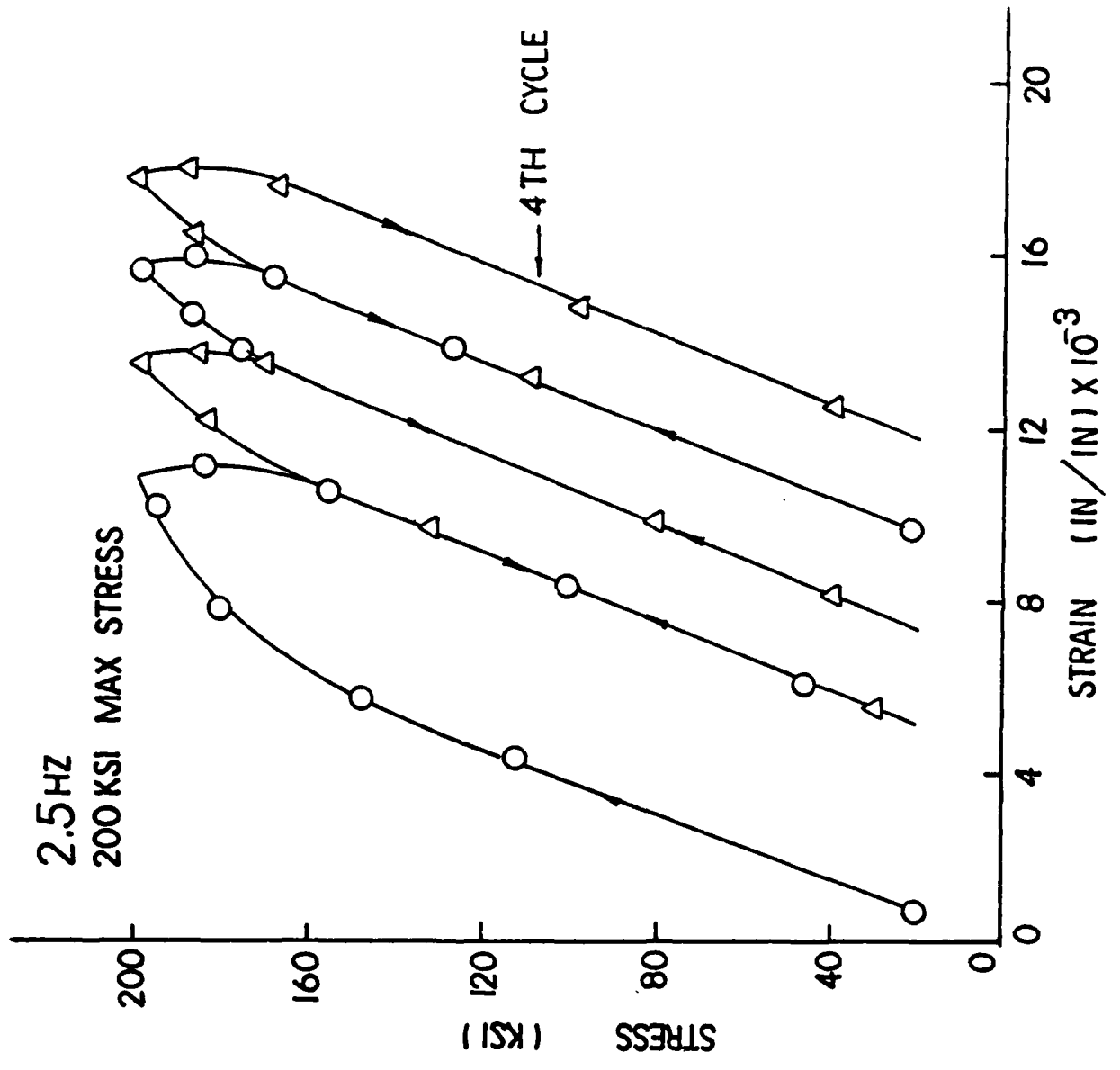


Fig 4.5 Uniaxial Stress-Strain Curve

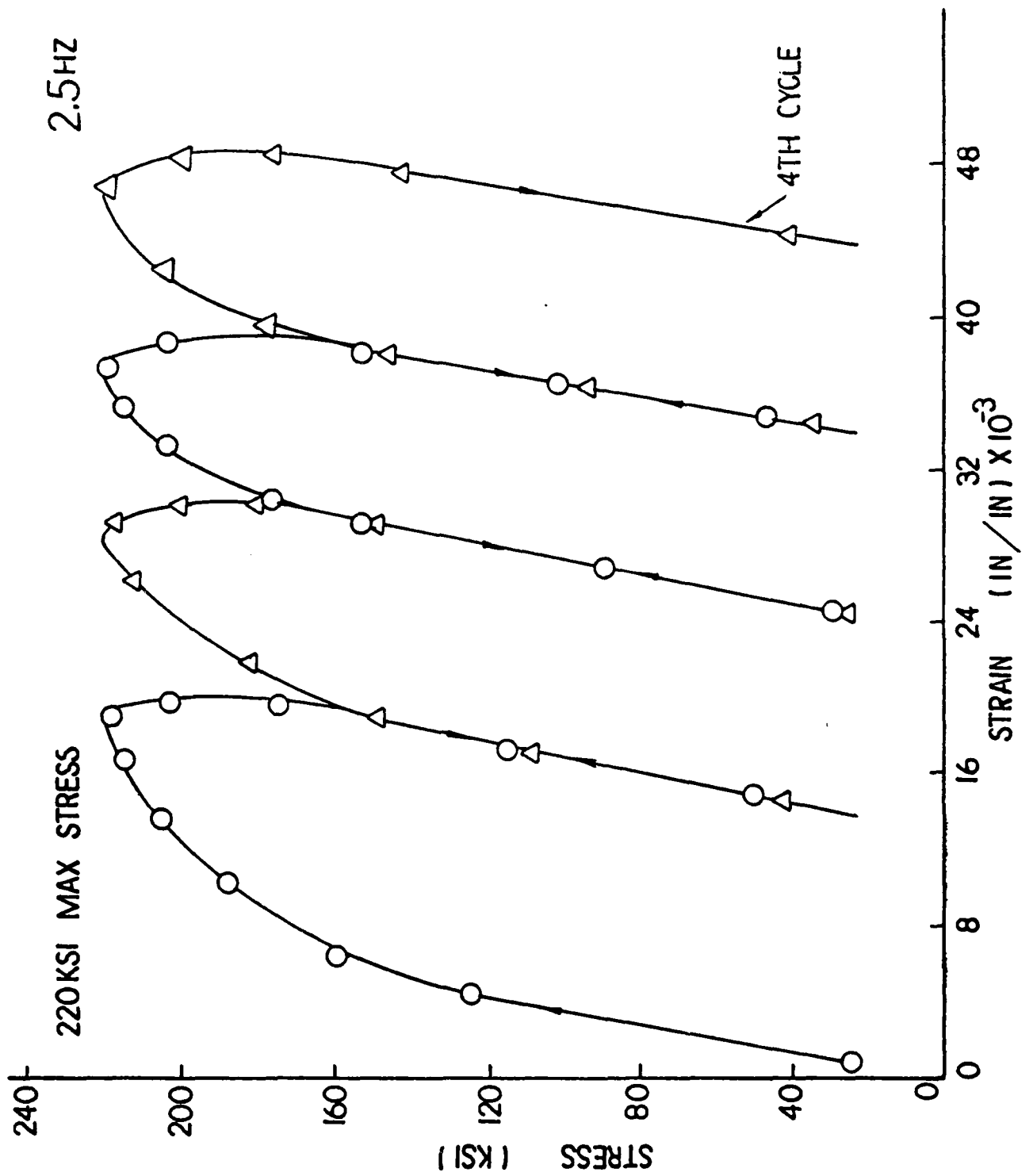


Fig 4.6 Uniaxial Stress-Strain Curve

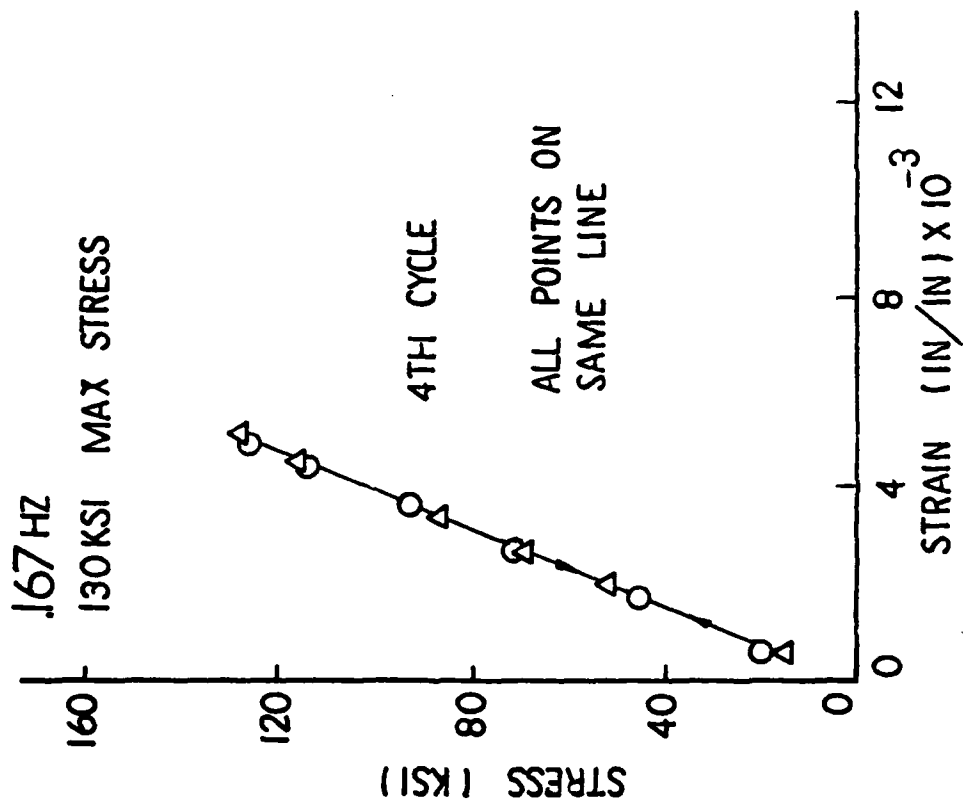


Fig 4.7 Uniaxial Stress-Strain Curve .167Hz
130KSI Max Stress

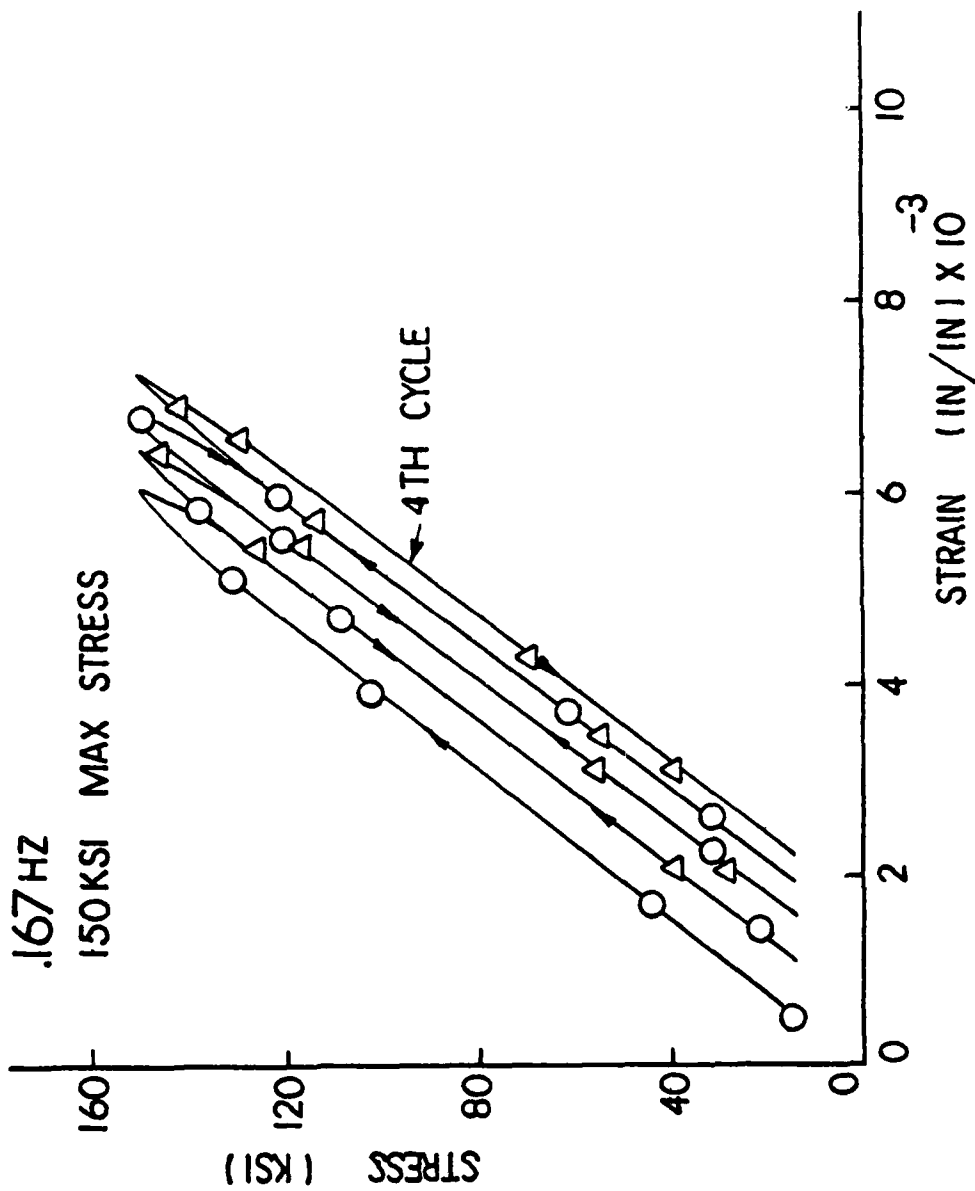


Fig 4.8 Uniaxial Stress-Strain Curve

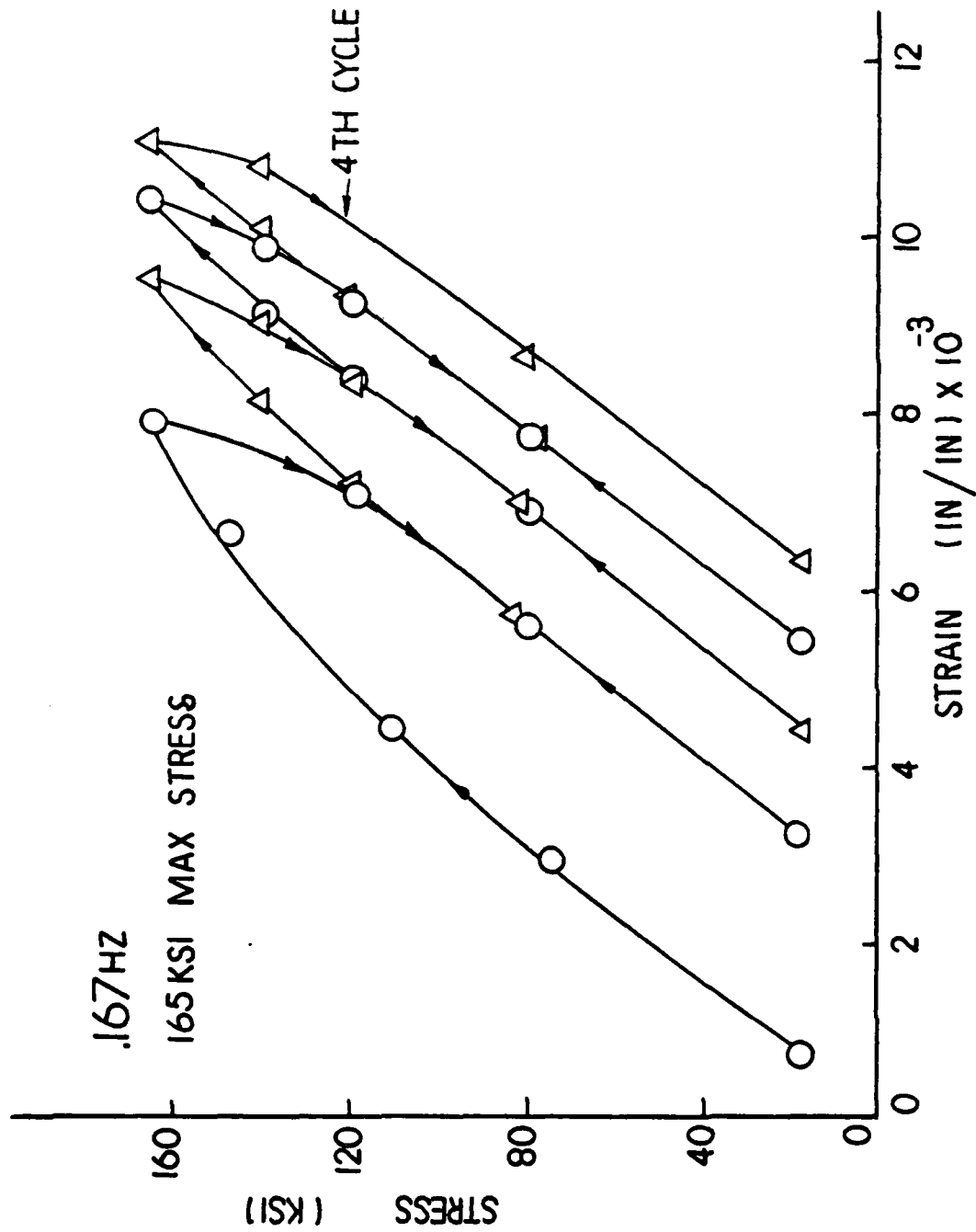


Fig 4.9 Uniaxial Stress-Strain Curve

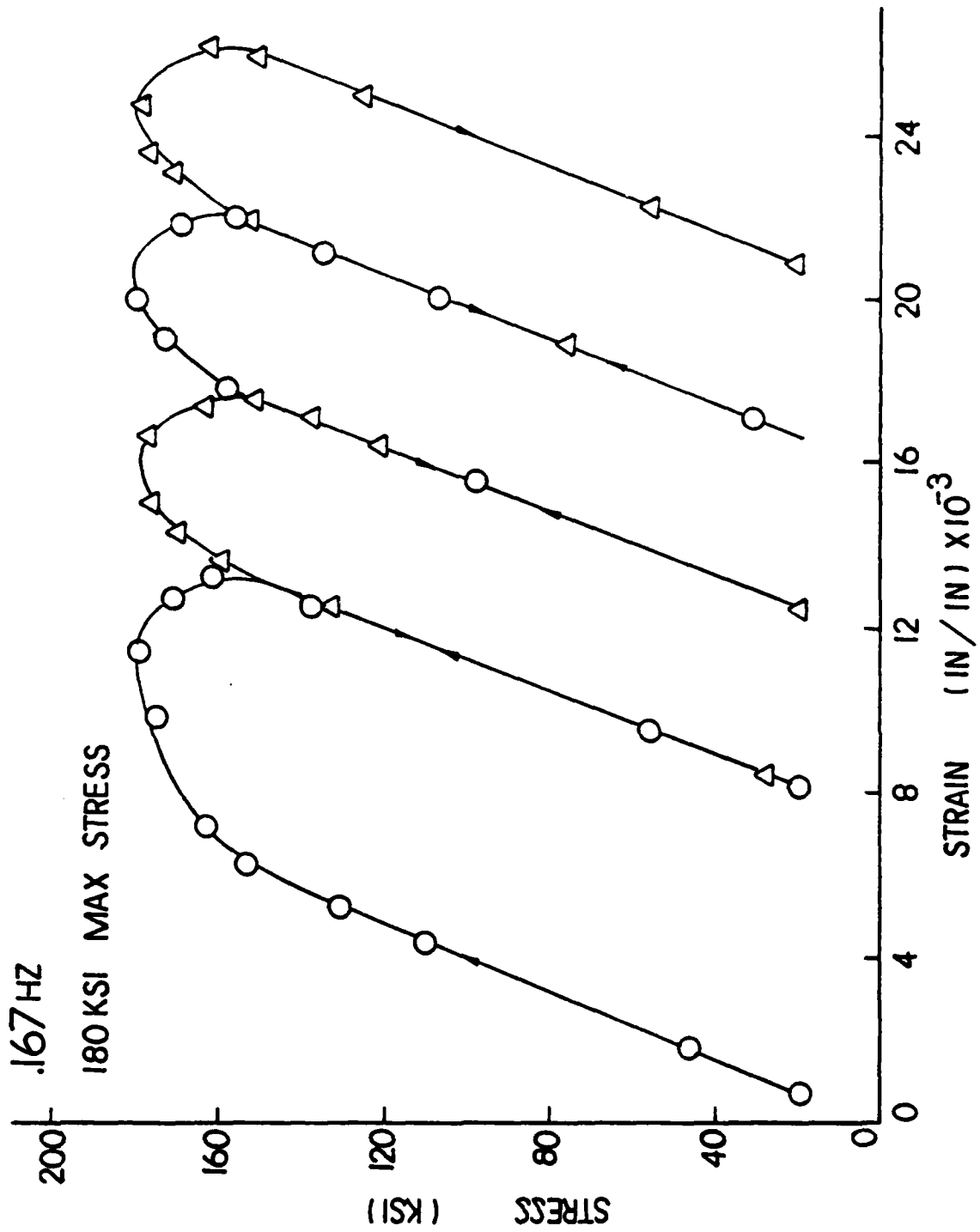


Fig 4.10 Uniaxial Stress-Strain Curve

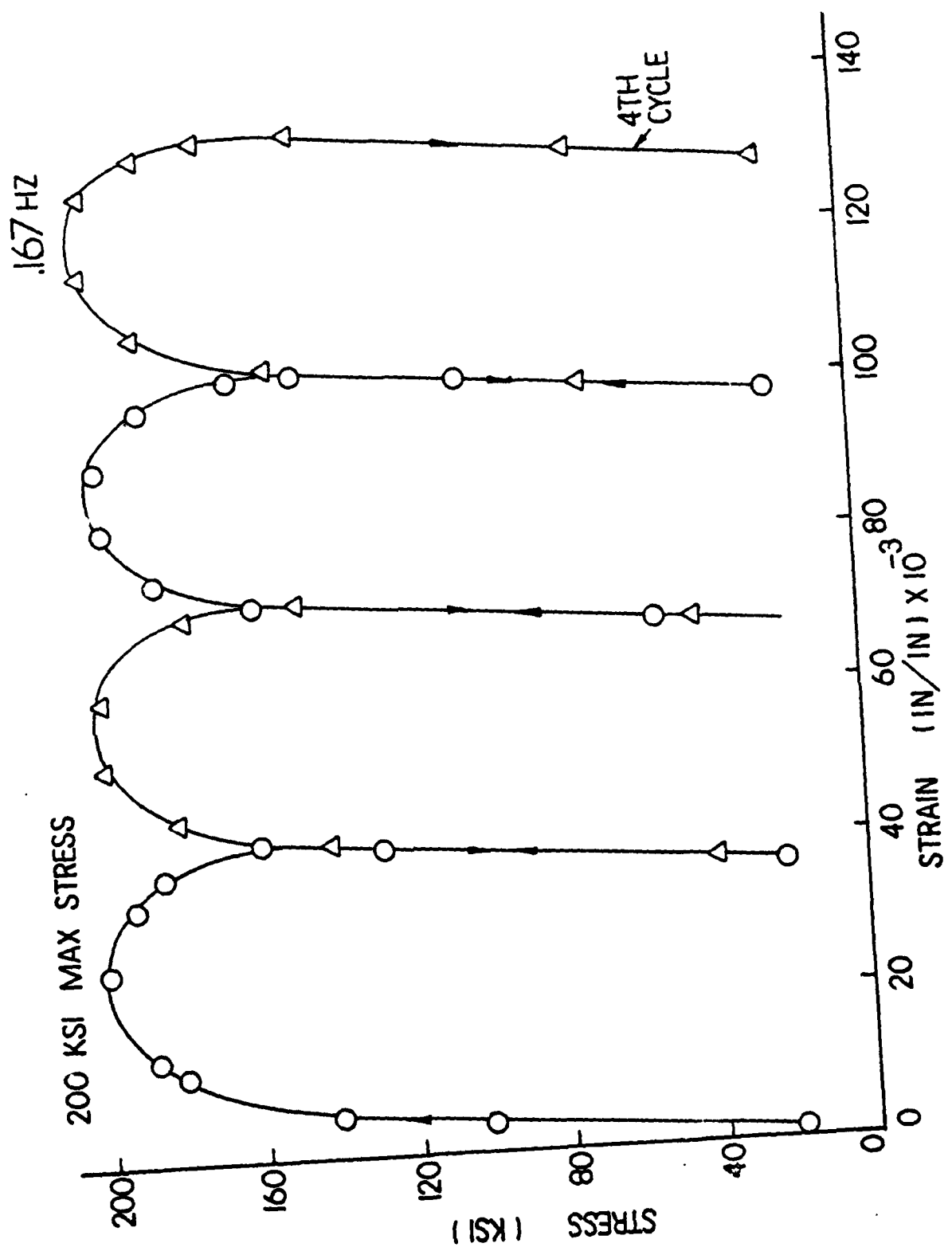


Fig 4.11 Uniaxial Stress-Strain Curve

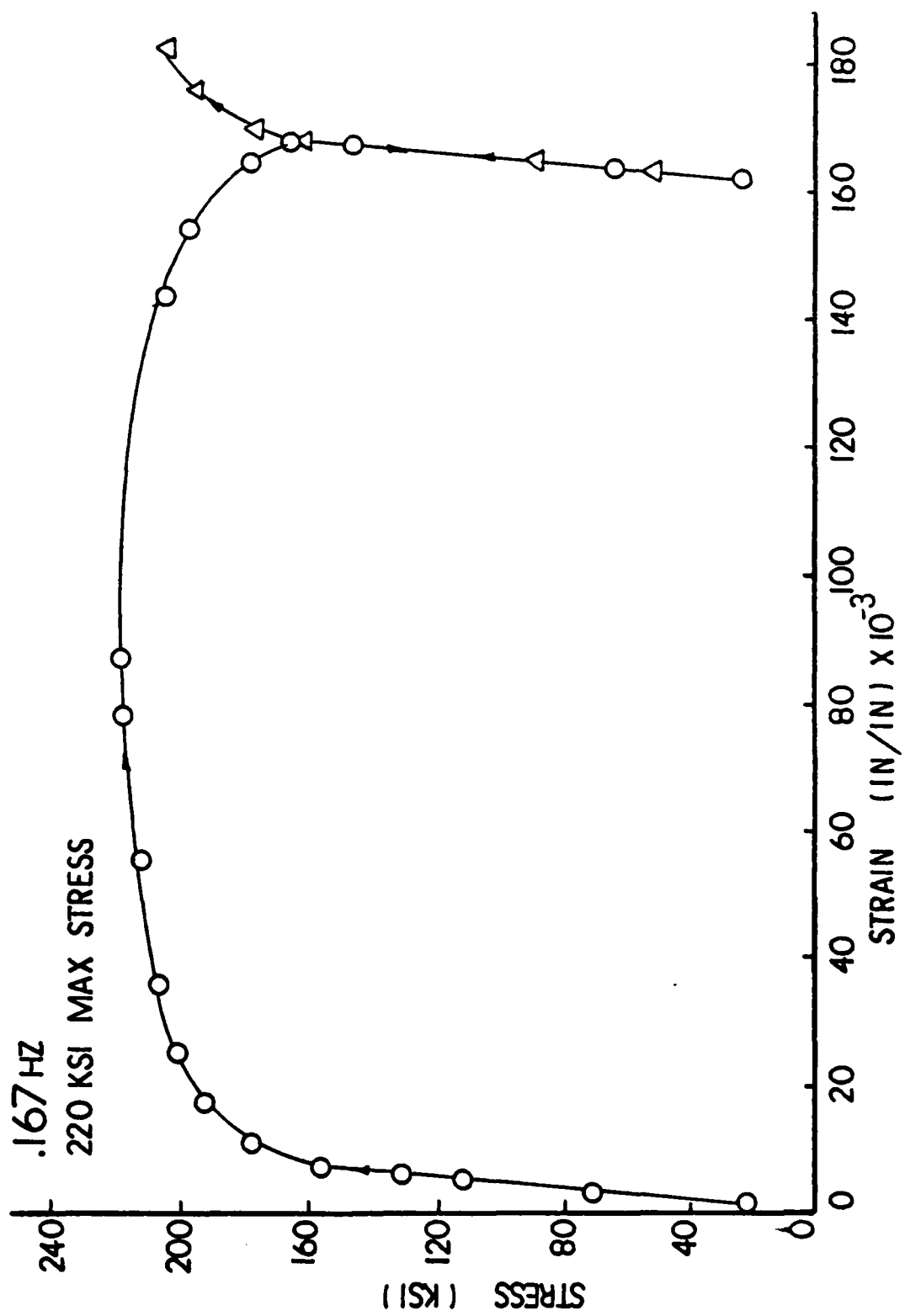


Fig 4.12 Uniaxial Stress-Strain Curve

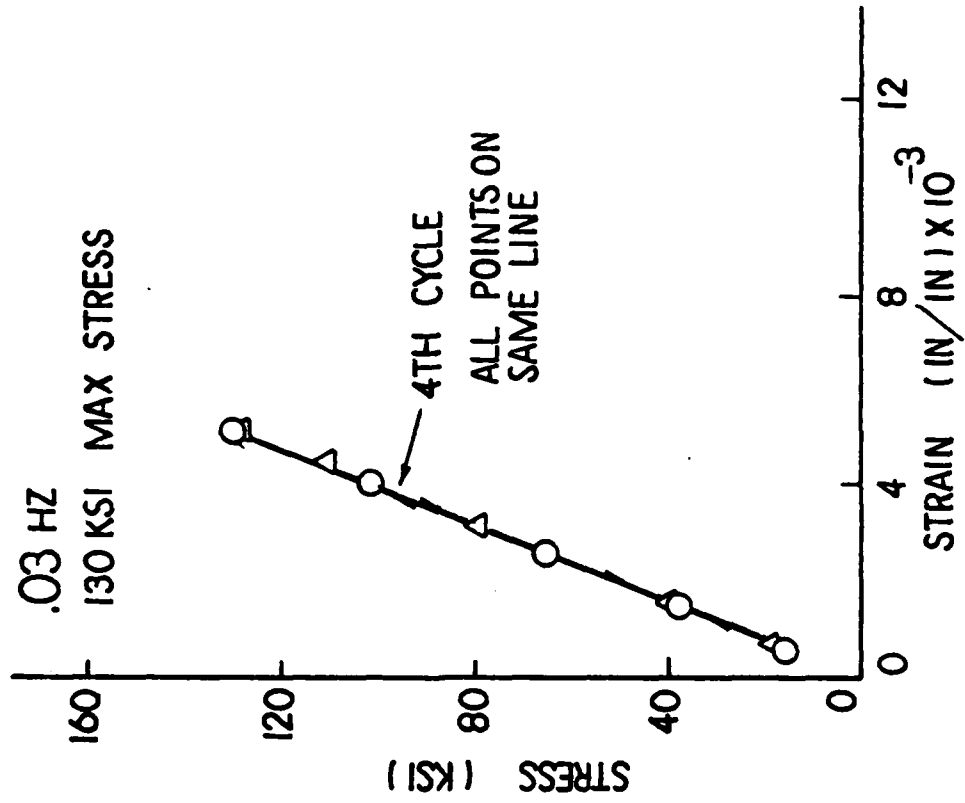


Fig 4.13 Uniaxial Stress-Strain Curve

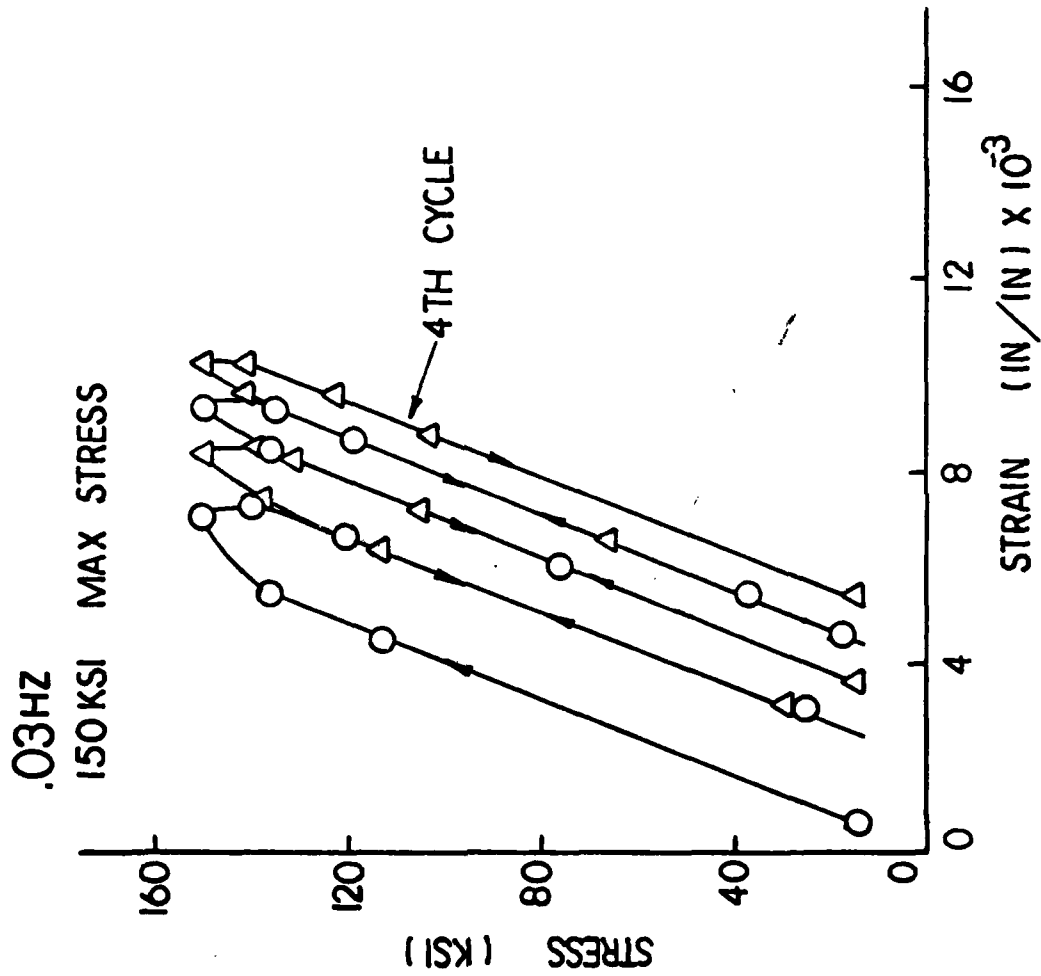


Fig 4.14 Uniaxial Stress-Strain Curve

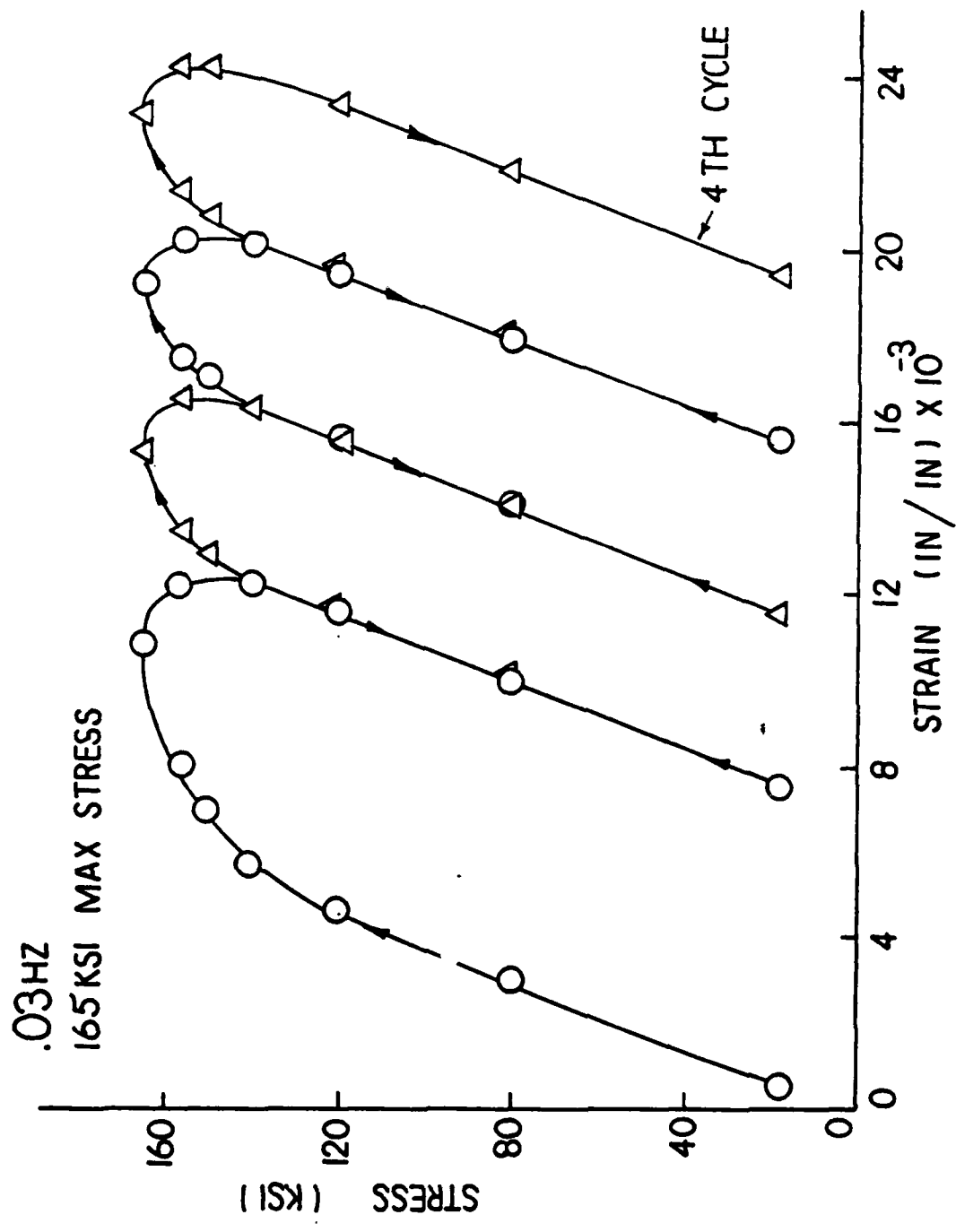


Fig 4.15 Uniaxial Stress-Strain Curve

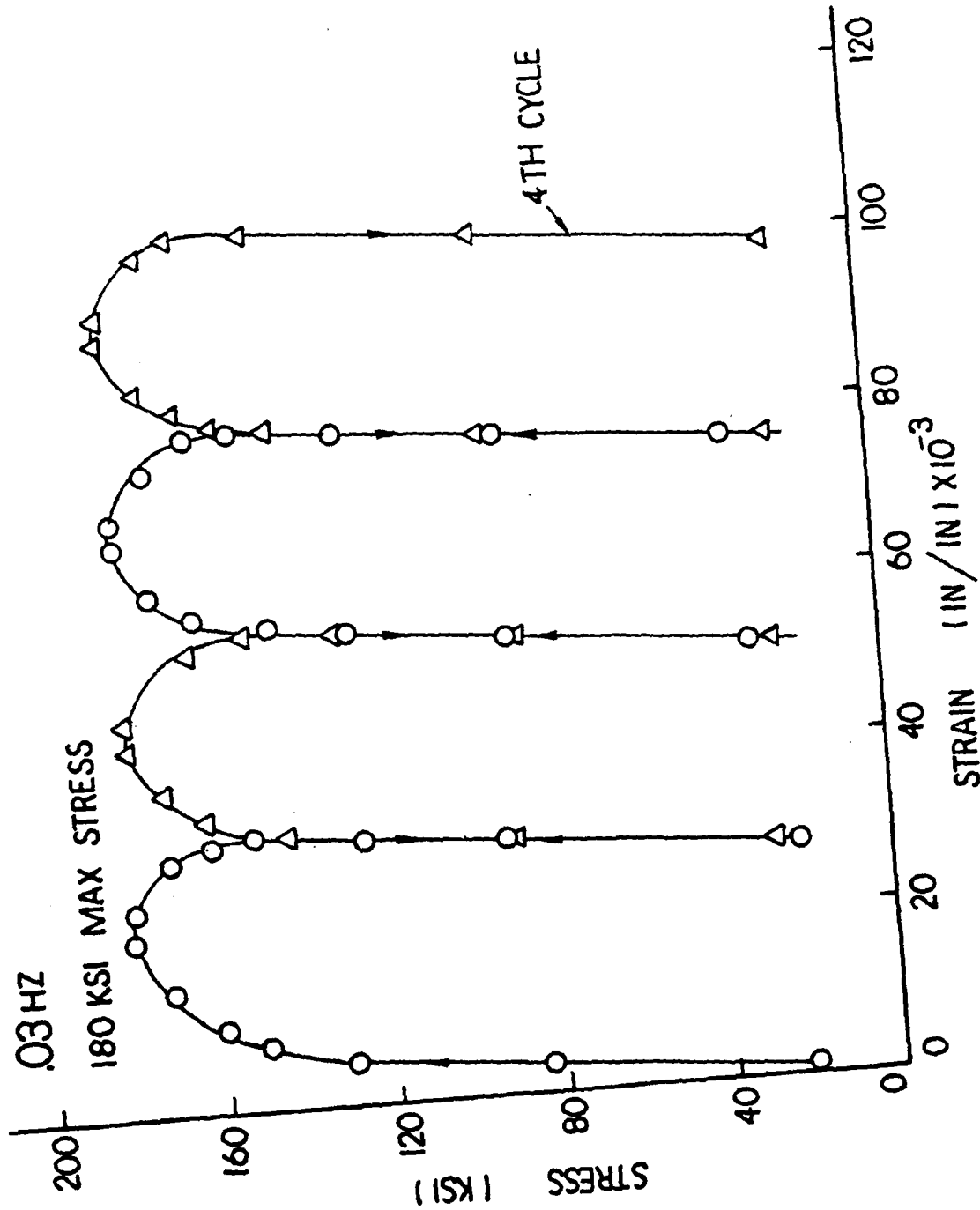


Fig 4.16 Uniaxial Stress-Strain Curve

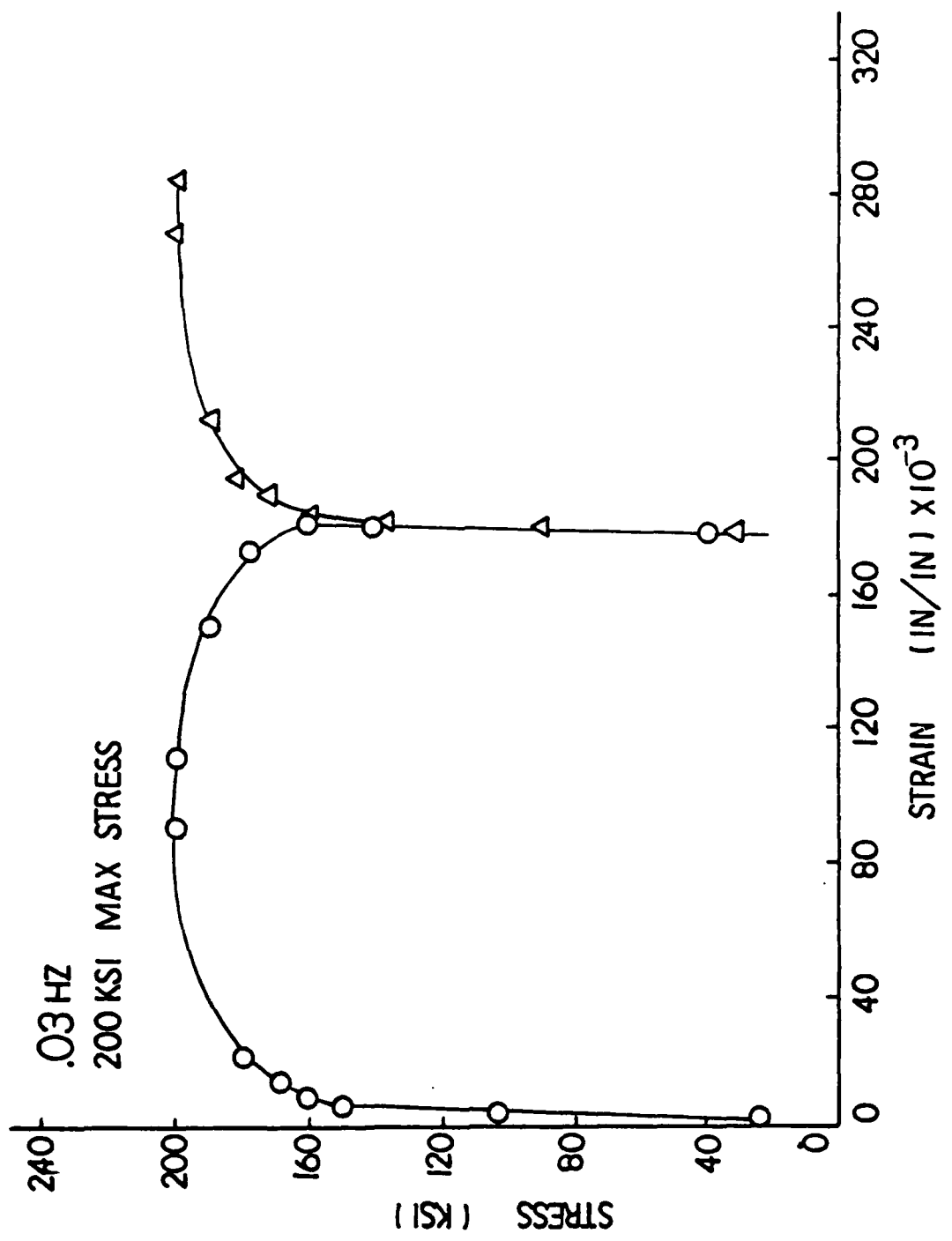


Fig 4.17 Uniaxial Stress-Strain Curve

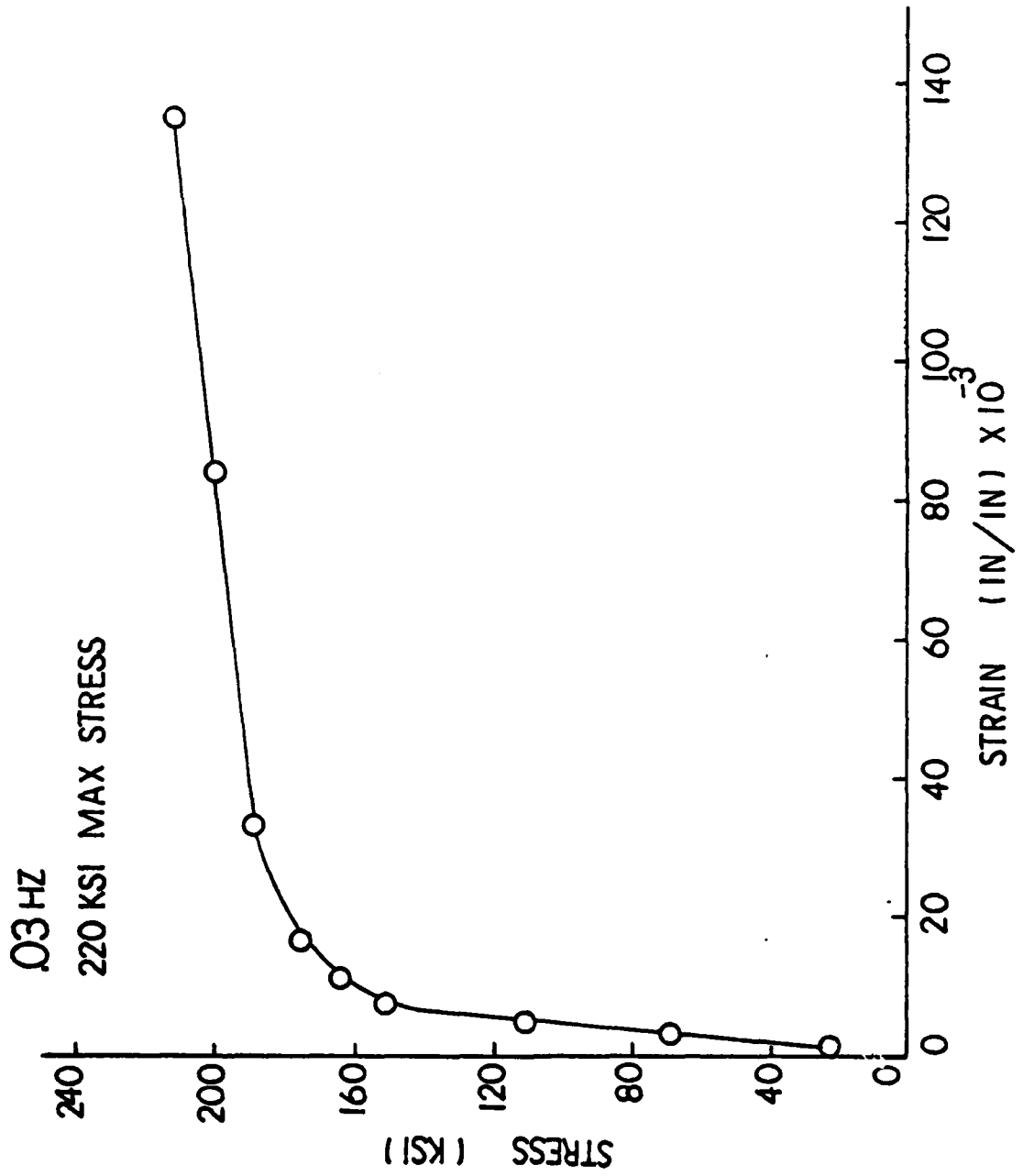


Fig 4.18 Uniaxial Stress-Strain Curve

stress levels of 180KSI or greater, with the exception of the 2.5Hz specimen at 180KSI.

If one compares the cyclic stress-strain loops of Fig's. 4.1-4.18 to the Z hardness curves, Fig's. 4.19-4.21 show constant magnitude plastic strain per cycle occurs only when Z hardness saturates.

In addition, Z hardness does not oscillate with the load cycle. The plastic deformation occurring during each load cycle causes Z to increase until reaching saturation. After Z reaches saturation, the additional plastic deformation accumulated per cycle is balanced by the relaxation due to temperature. Thus, the material has reached its fully hardened state and does not vary with additional plastic deformation. The foregoing results graphically depict the thermal hardening recovery and secondary creep characteristics of the Bodner model. By setting the time derivative of equation 2.24 equal to zero, the rate of work hardening equals the rate of thermal hardness recovery. For a given time increment after Z reaches saturation, a balanced condition is present which represents secondary creep. Each additional load cycle causes constant magnitude plastic deformation increases per cycle, shifting the stress-strain curves to the right (Fig 4.1 - 4.18). Comparing stress levels and time values in Fig's 4.19 - 4.21 reveals that Z saturates at approximately the same time and is independent of frequency.

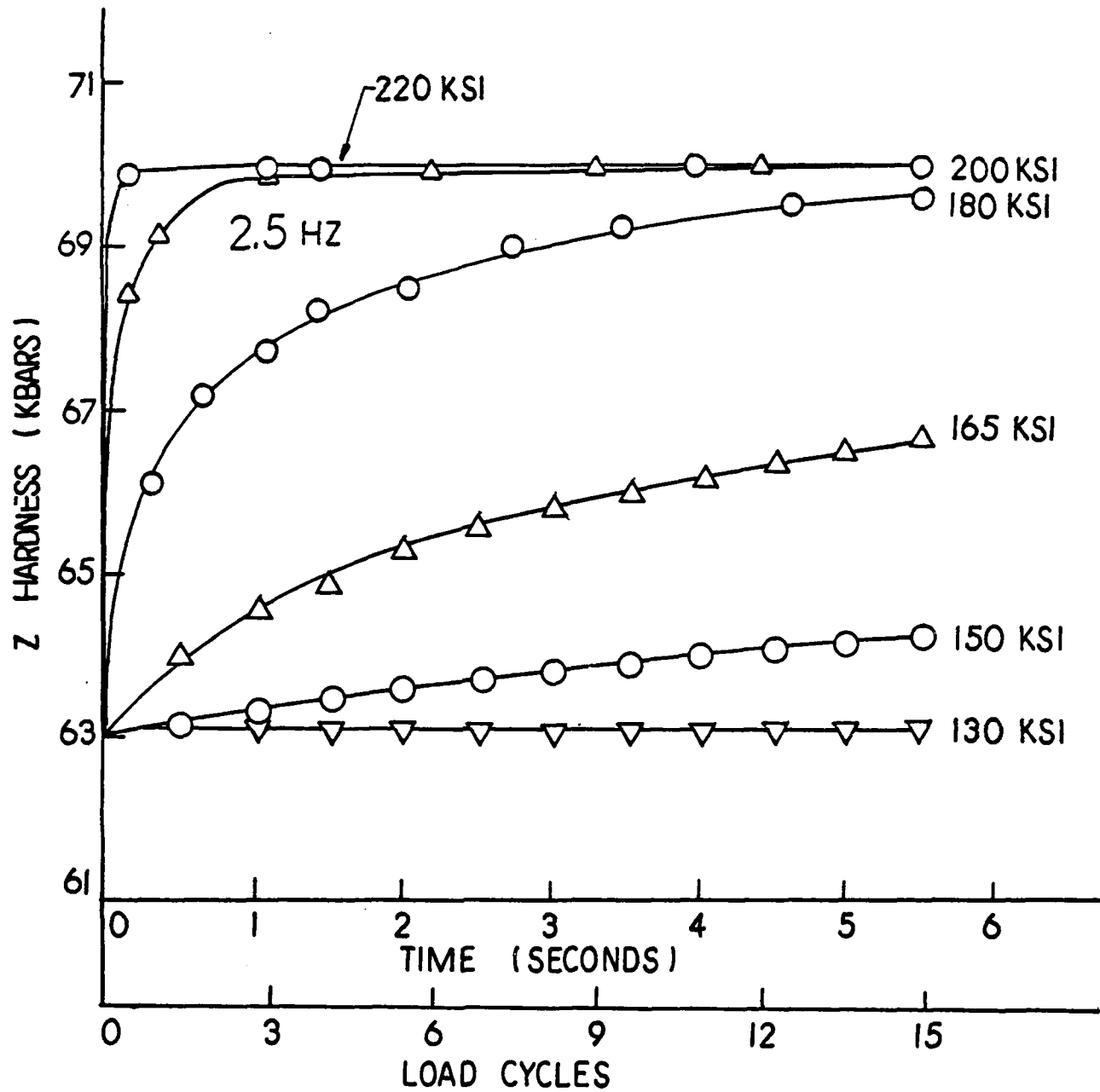


Fig 4.19 Z Hardness vs Time

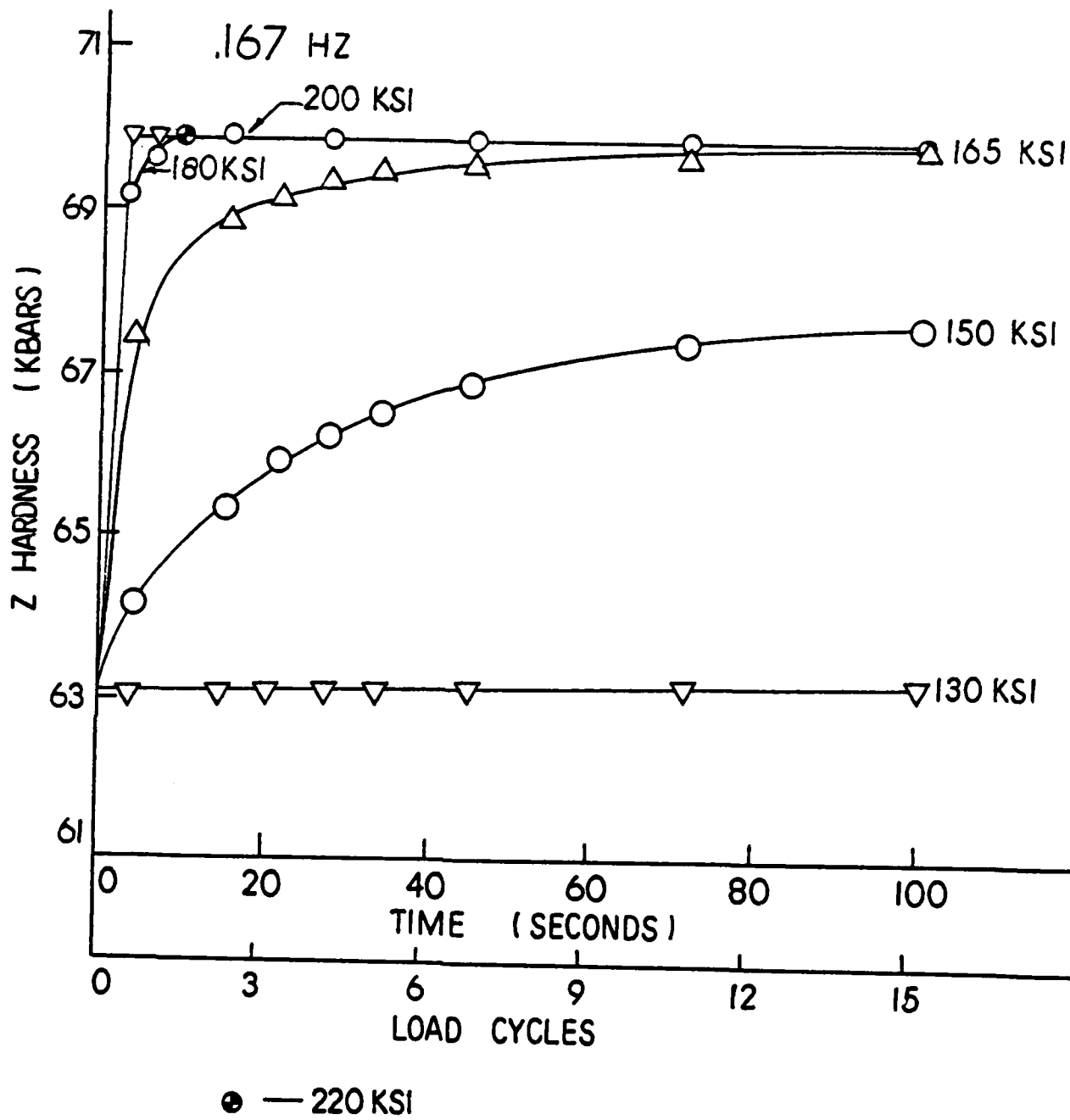


Fig 4.20 Z Hardness vs Time

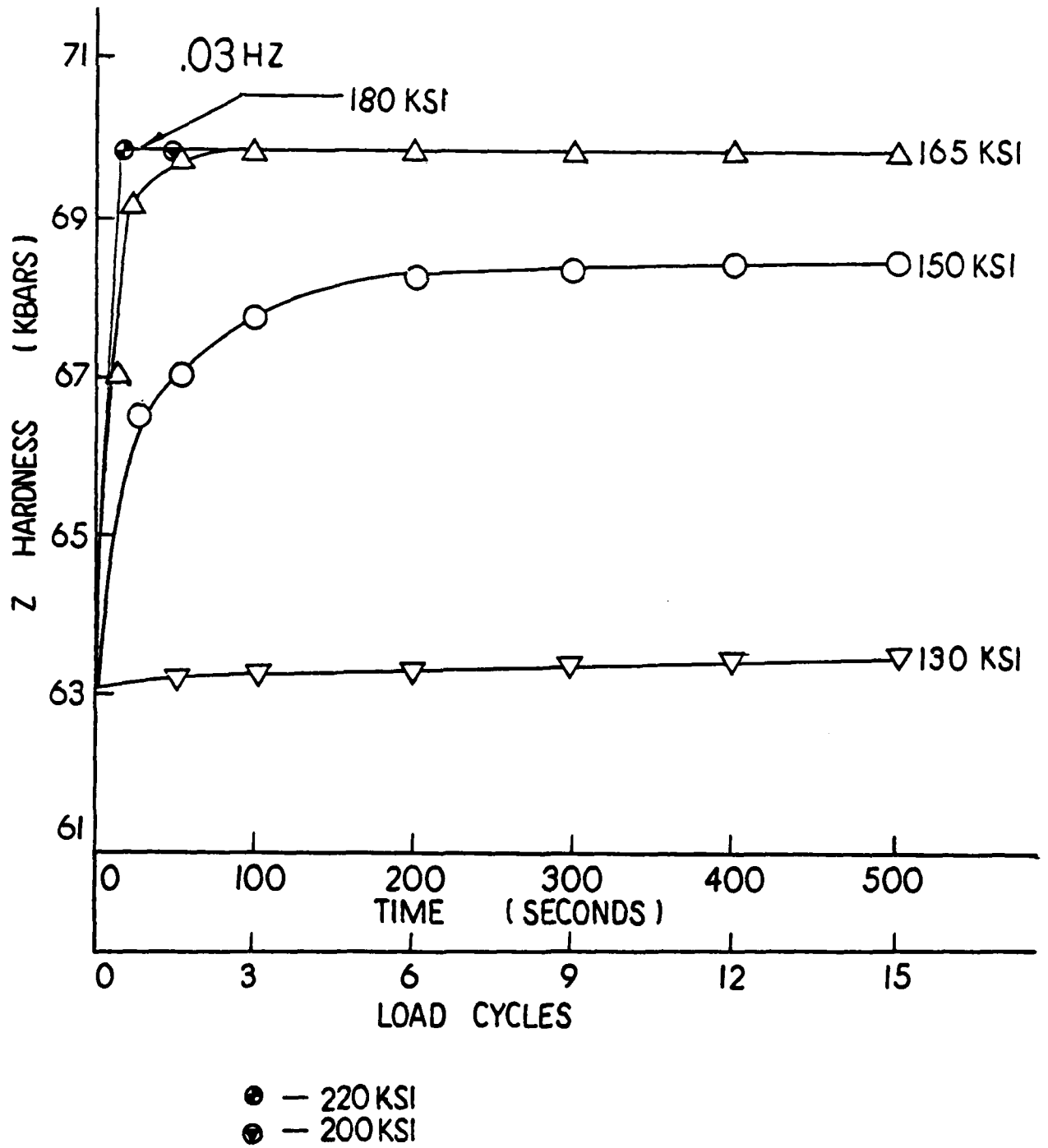


Fig 4.21 Z Hardness vs Time

It should be noted in Fig. 4.22, which is typical of all uniaxial cases, that plastic strain increases during that portion of the load cycle where the stress is above the reference yield stress. These strain rise points occur at approximately 80 percent of the applied load. During the unload portion of the cycle while above the yield stress, plastic deformation continues. Between cycles, plastic strain remains constant until the subsequent "yield point" is reached. The magnitude of the rise in plastic strain during each load cycle decreases until Z hardness reaches its saturation value (maximum).

MAX STRESS 165 KSI

2.5 HZ

PLASTIC STRAIN

PERCENT LOAD

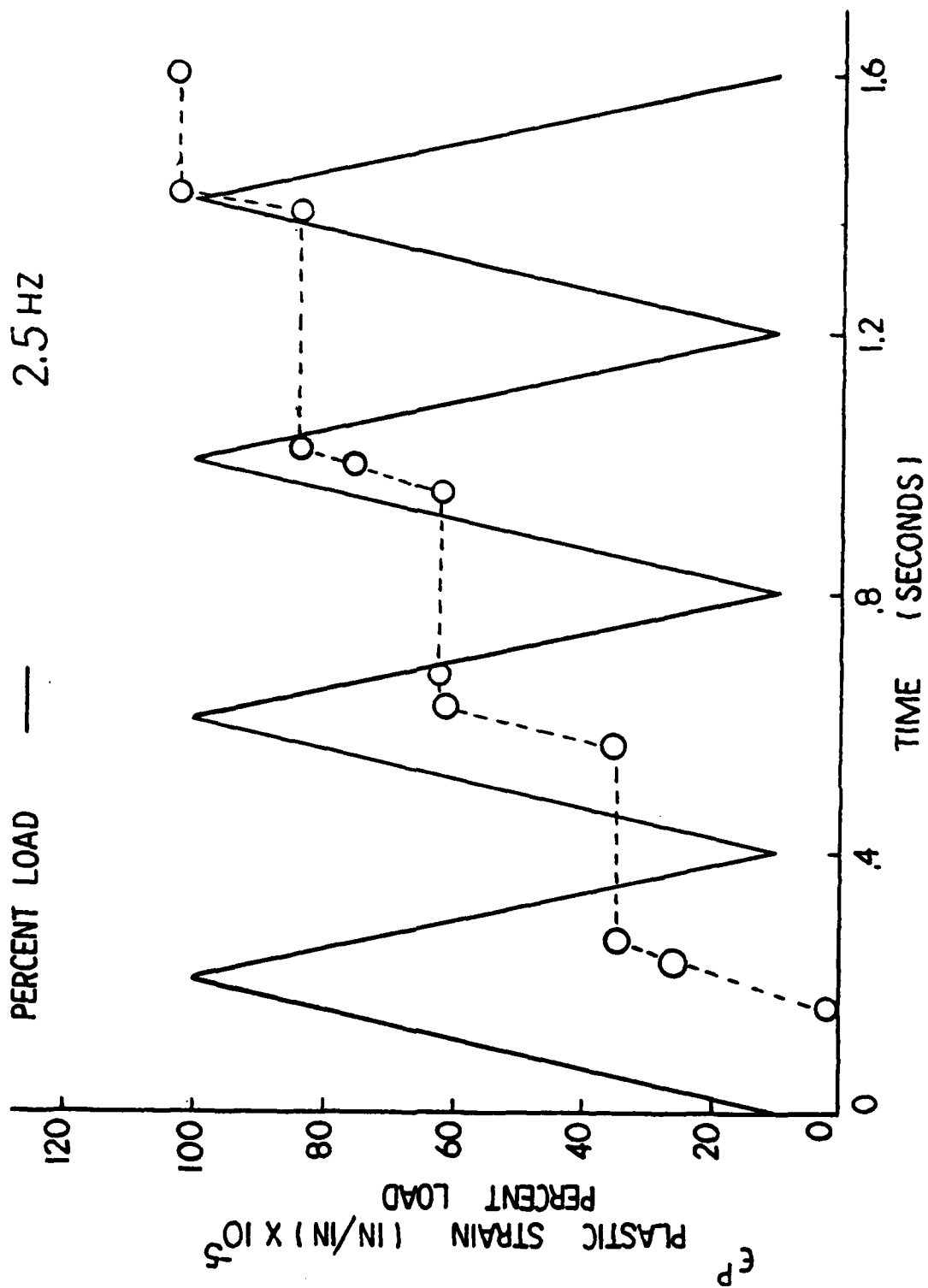


Fig 4.22 Plastic Strain vs Time

Compact Tension Specimen Tests

Results and comparisons made in this section are presented for each frequency and stress intensity factor shown in Fig. 3.6. Subsequent figures are in five groups as shown below:

- a) Cyclic stress strain curves at the crack tip for the first 3 load cycles
- b) Profiles of y stress, y strain and Z hardness as a function of distance ahead of the crack tip for the first 3 cycles
- c) Changes in plastic zone size with the number of load cycles
- d) Vertical (y) displacement behind the crack tip versus distance behind crack tip during cyclic unload
- e) Cyclic crack mouth displacement versus load curves

As shown in Fig's. 4.23, 4.24, 4.25, and 4.26, (effective stress versus total strain curves); rapid increases in plastic deformation at the crack tip occur during the first load cycle. No significant changes occur afterward. Constant magnitude plastic deformation occurs with each successive cycle. If one compares these results with the Z hardness profiles, Fig's. 4.29, 4.32, and 4.38, it can be seen that the Z hardness near the crack tip reaches saturation in the first half load cycle. The material at the crack tip is fully hardened; further cycling produces no further hardening. Referring to Fig's. 4.29-4.38, no significant changes in y strain, Z hardness, or y stress profiles ahead of the crack tip occur after the first cycle. This behavior

suggests a stable condition exists at the crack tip after the first cycle and can be compared directly with uniaxial results shown in Fig's. 4.1-4.18. This suggests that the material ahead of the crack tip is essentially in a stress controlled boundary condition, and accumulates plastic strain per cycle just as it does in the uniaxial cases. No net accumulation of strain per cycle would be seen if the material ahead of the crack tip was strain controlled. In addition, this type of behavior ahead of the crack tip infers that if nodes are released in the finite element model to simulate crack growth, and the number of load cycles between node releases is large; changes ahead of the crack tip will occur the instant the node is released. One cycle after node release, the stress-strain field and Z hardness remain essentially constant until the next node is released. This suggests that the behavior ahead of the crack associated with crack growth can be characterized by a short transient period after node release followed by stable cyclic behavior until the next node is released.

If the stress profiles ahead of the crack tip are known, one can refer to the uniaxial results and come very close to predicting the behavior in the compact tension finite element model. However, the stress ahead of the crack tip using the Linear Elastic Fracture Mechanics (LEFM) plane stress solution of Eq. 4.1, [1,11]

$$\sigma_y = \frac{K_1}{\sqrt{2\pi r}} \cos \frac{\theta}{2} \left[1 + \sin \frac{\theta}{2} \cos \frac{3\theta}{2} \right] \quad (4.1)$$

with theta (θ) of zero degrees, stress intensity factors (K_1) of 35 and 45KSI $\sqrt{\text{in}}$ respectively differed significantly from the finite element solution. Results depicted in Fig's. 4.27, 4.30, 4.33, and 4.36 show that the LEFM solution overestimates the stress field near the crack tip in most cases until reaching 0.02 inches ahead of the crack tip. Beyond 0.02 inches, LEFM underestimates stresses by 10%. Very near the crack tip (under 0.006 inches), the LEFM solution overestimates the stress by approximately 15 percent.

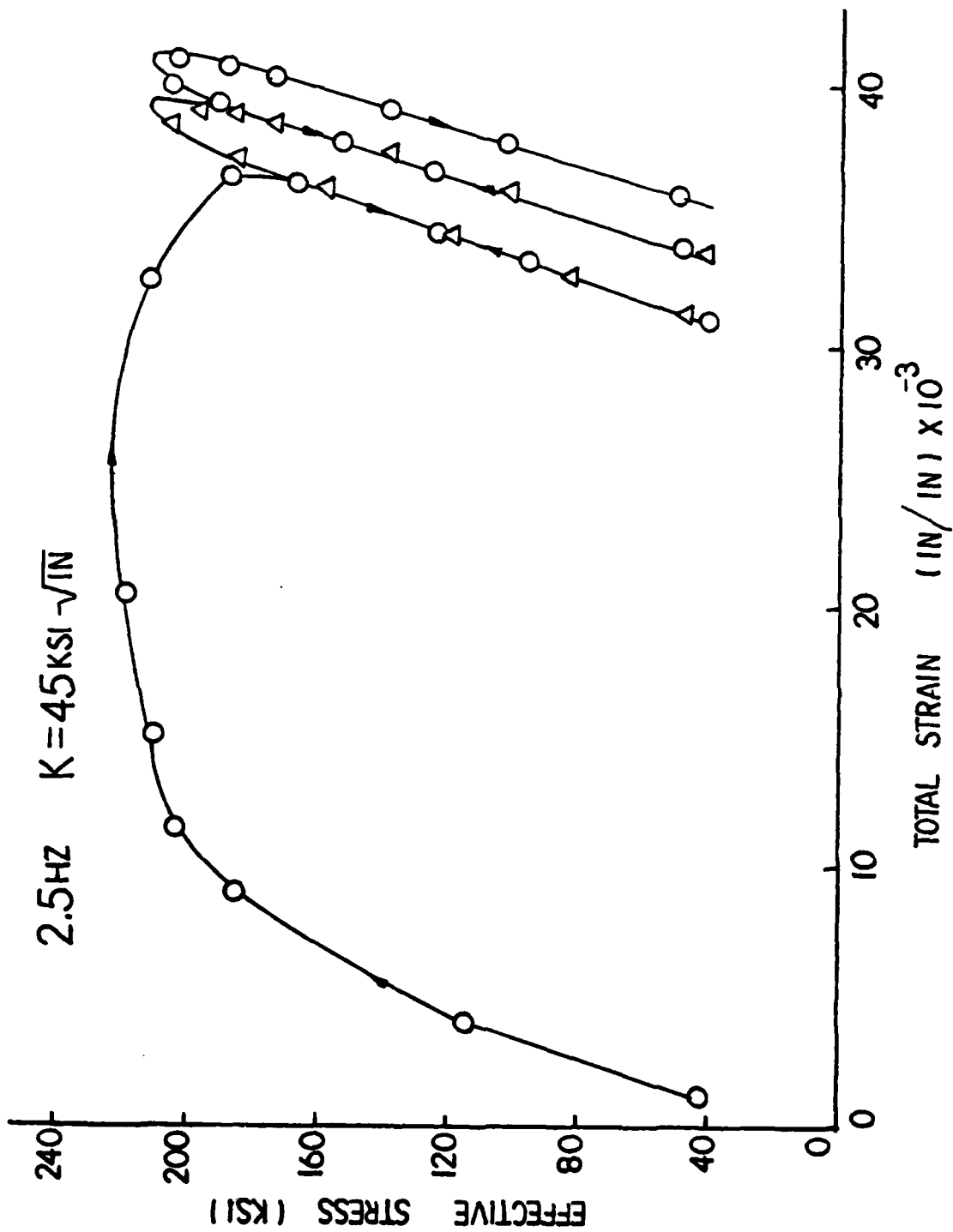


Fig 4.23 Effective Stress vs Total Strain at Crack Tip

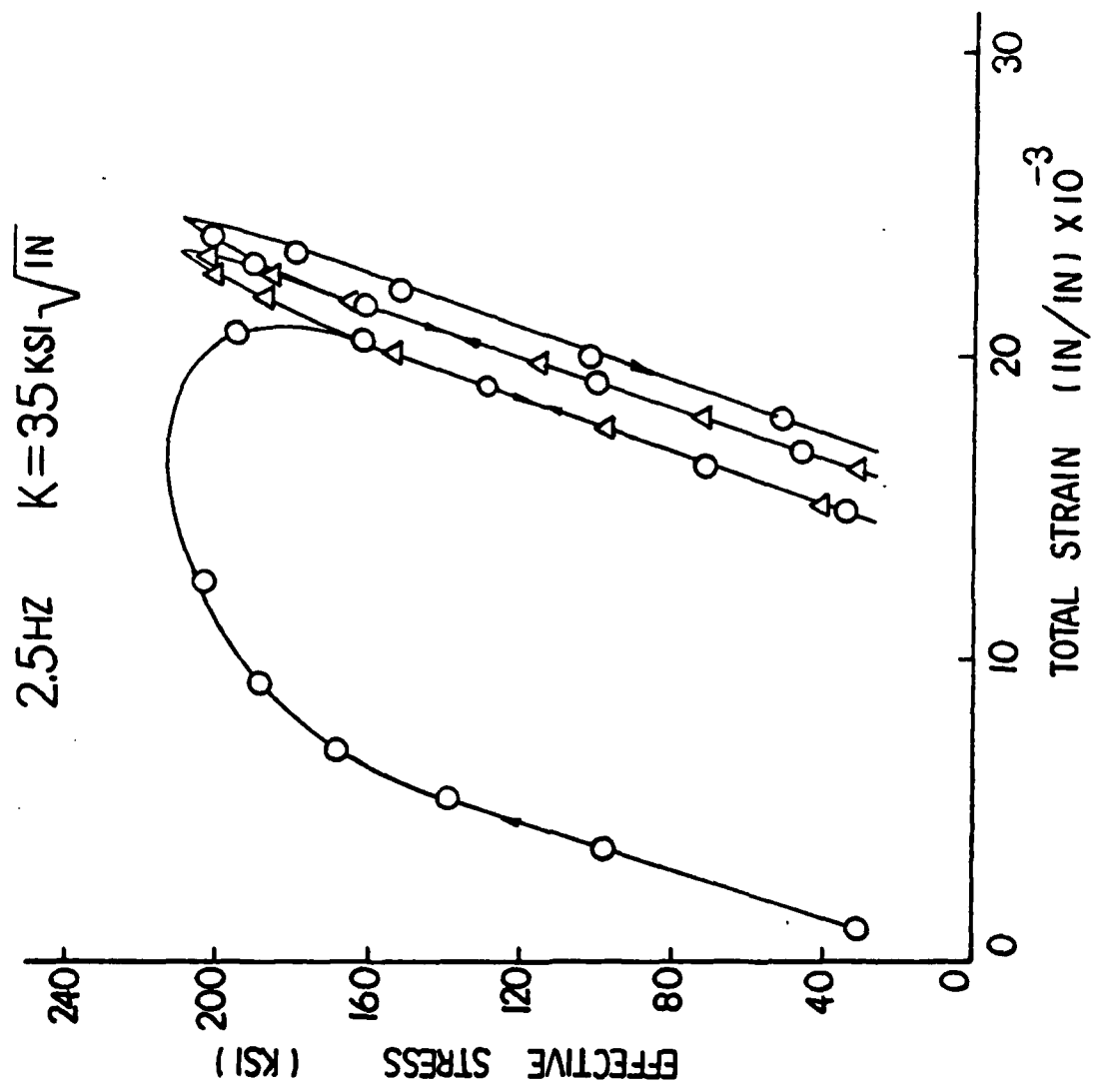


Fig 4.24 Effective Stress vs Total Strain at the Crack Tip

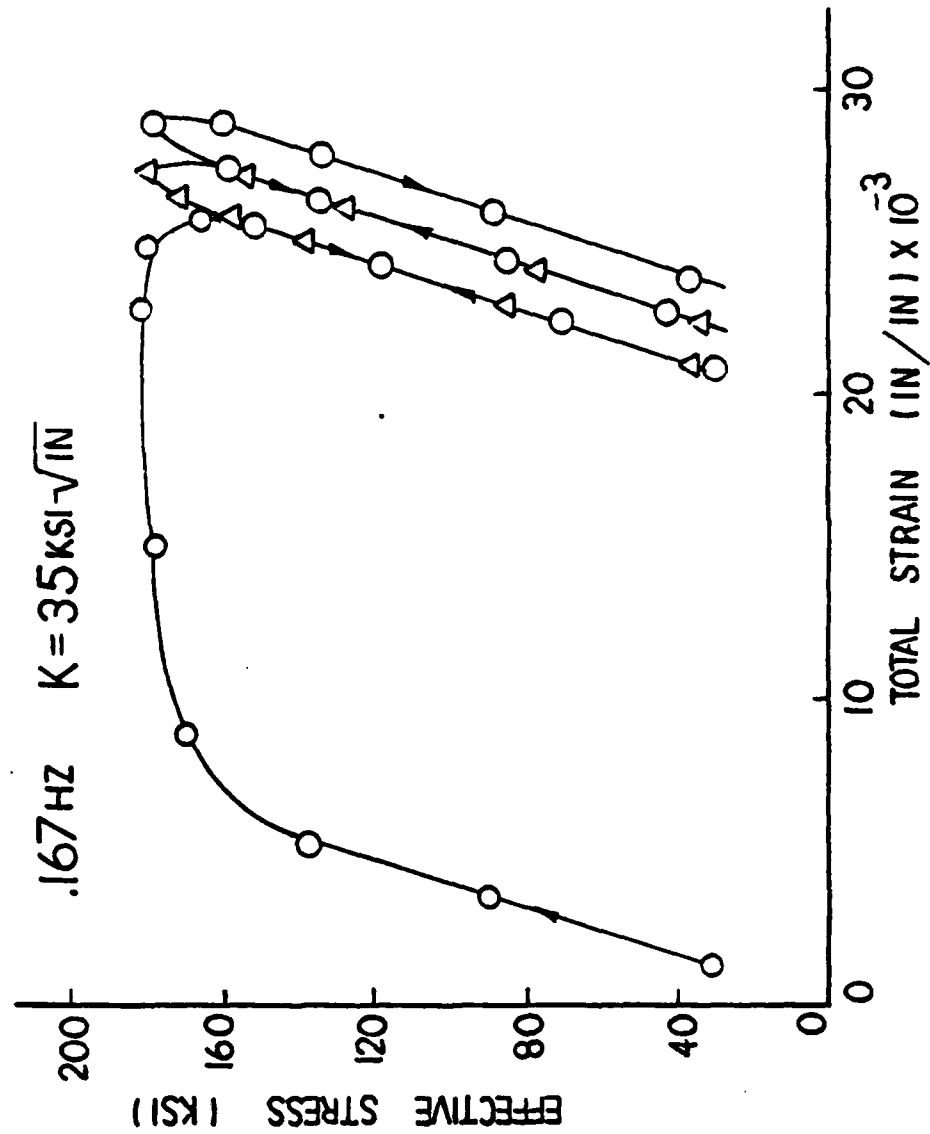


Fig 4.25 Effective Stress vs Total Strain
at Crack Tip .167Hz $K=35\text{KSI}\sqrt{\text{in}}$

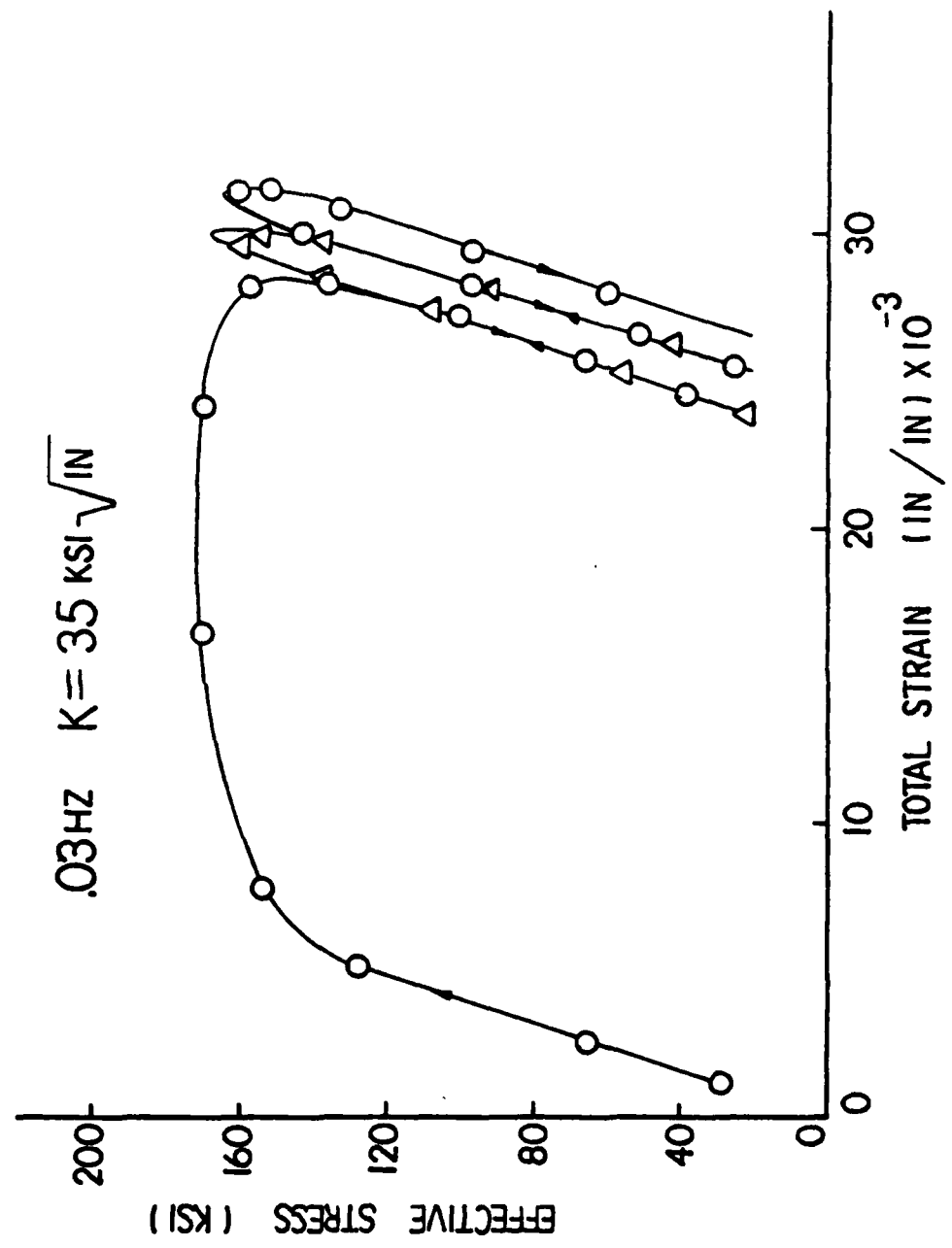


Fig 4.26 Effective Stress vs Total Strain at Crack Tip

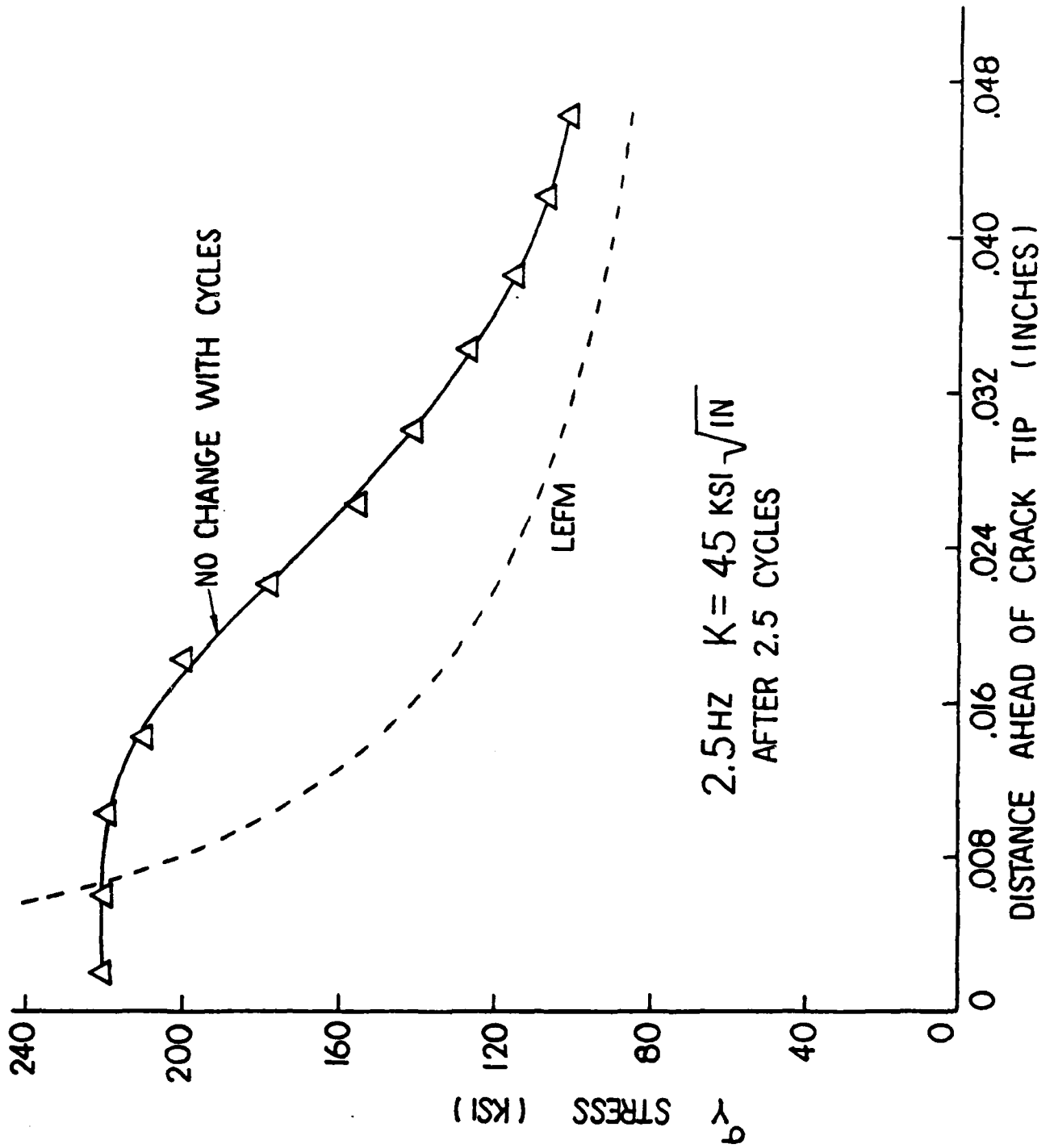


Fig 4.27 Y Stress vs Distance Ahead of Crack Tip

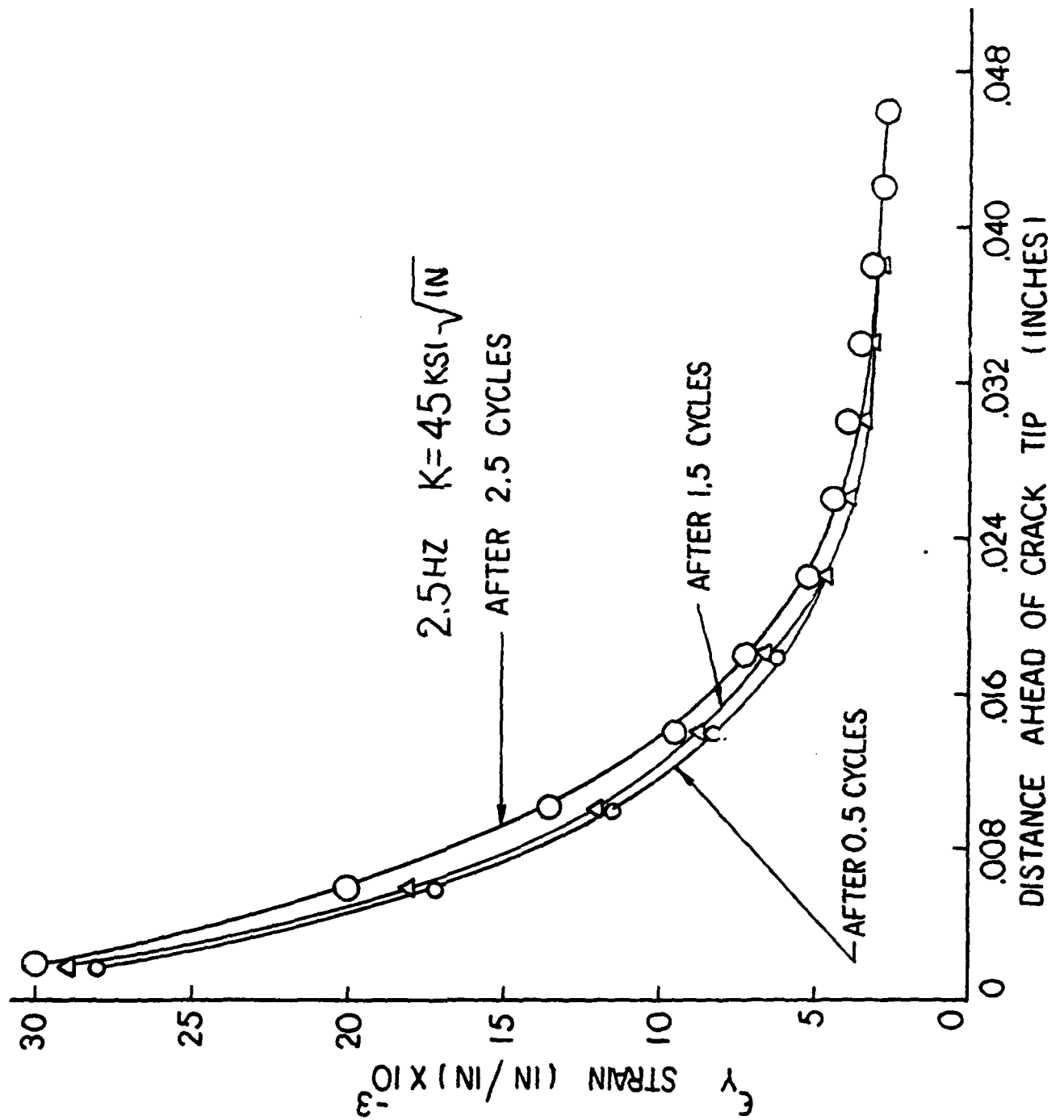


Fig 4.28 Y Strain vs Distance Ahead of Crack Tip

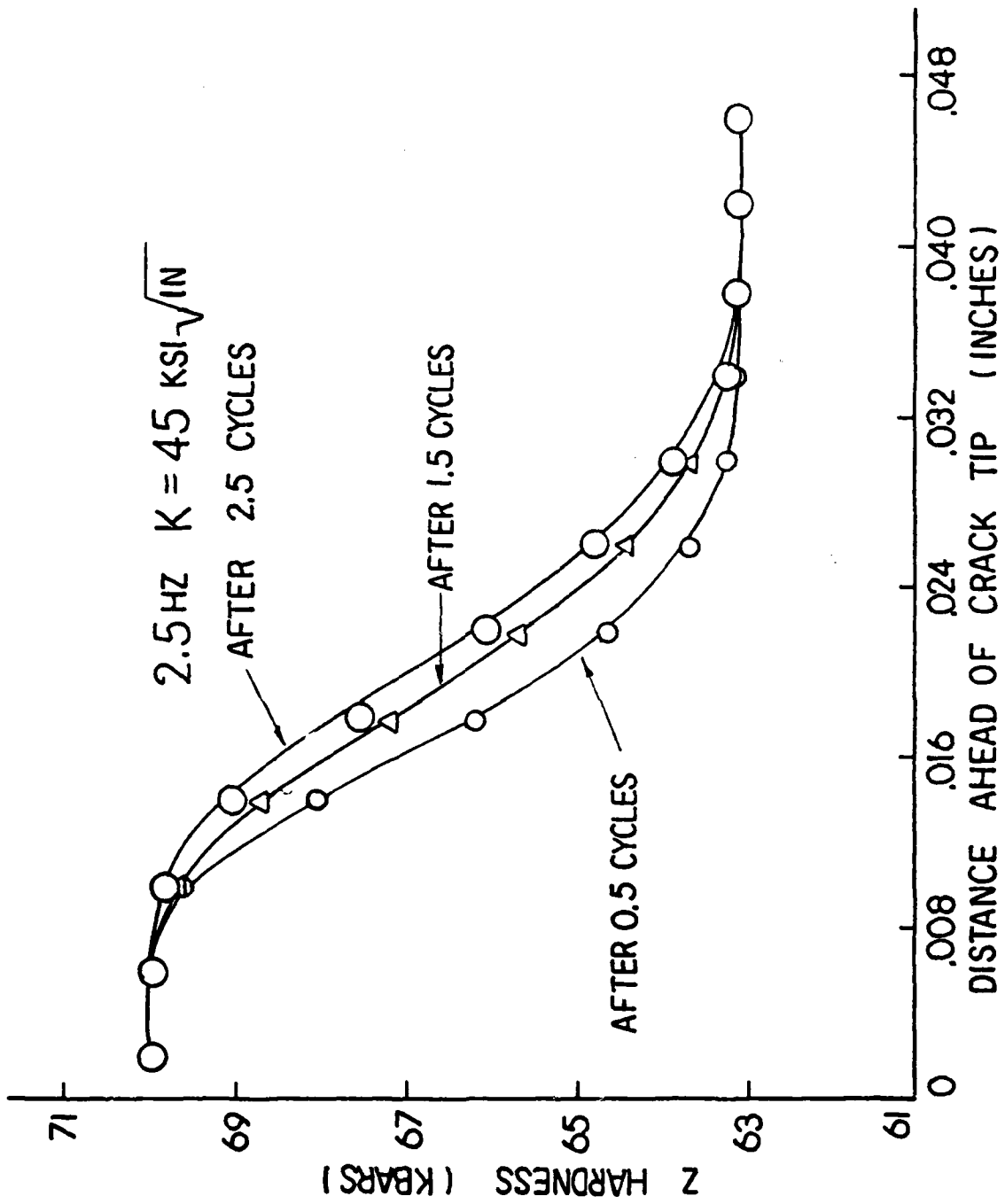


Fig 4.29 Z Hardness vs Distance Ahead of Crack Tip

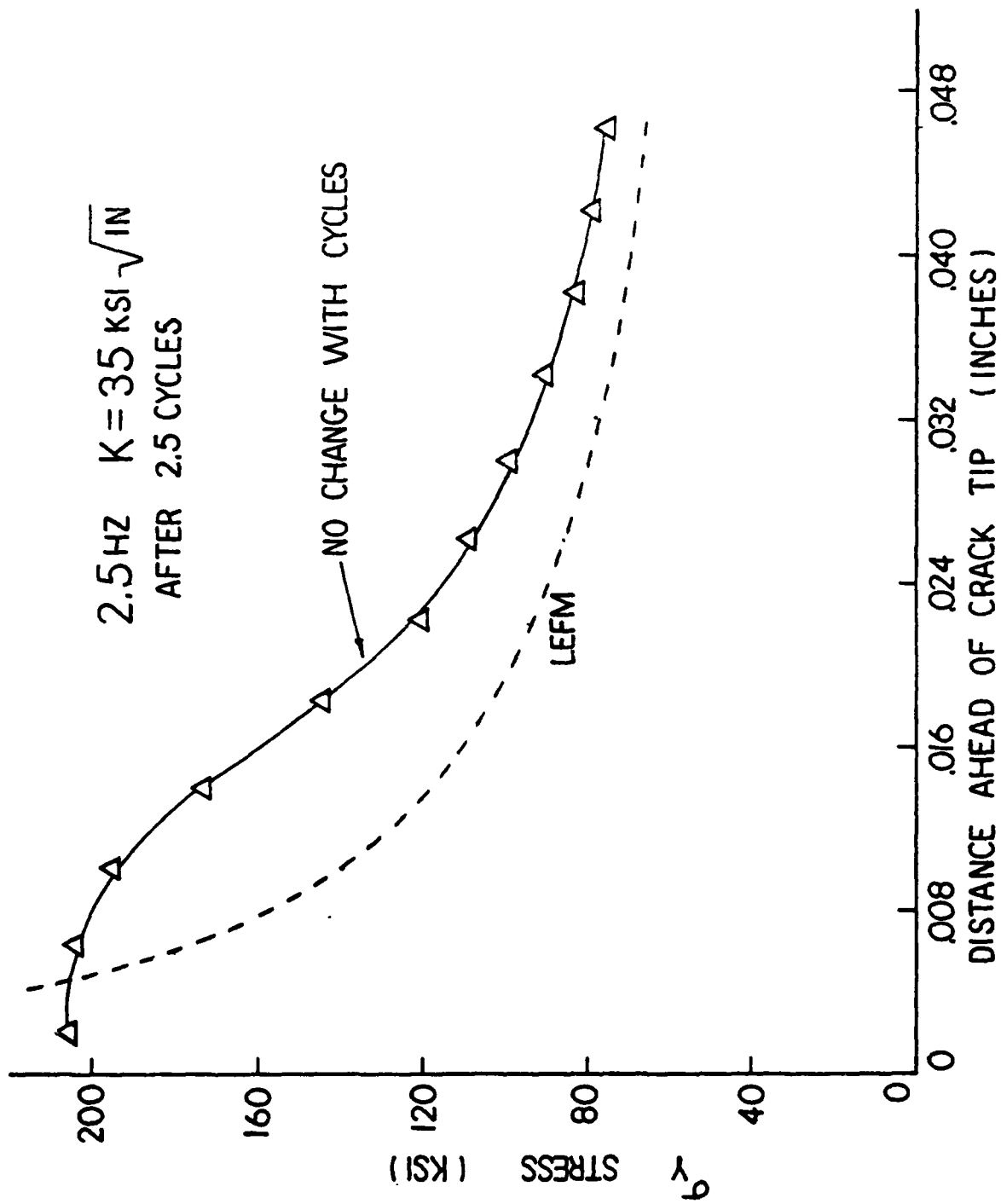


Fig 4.30 Y Stress vs Distance Ahead of Crack Tip

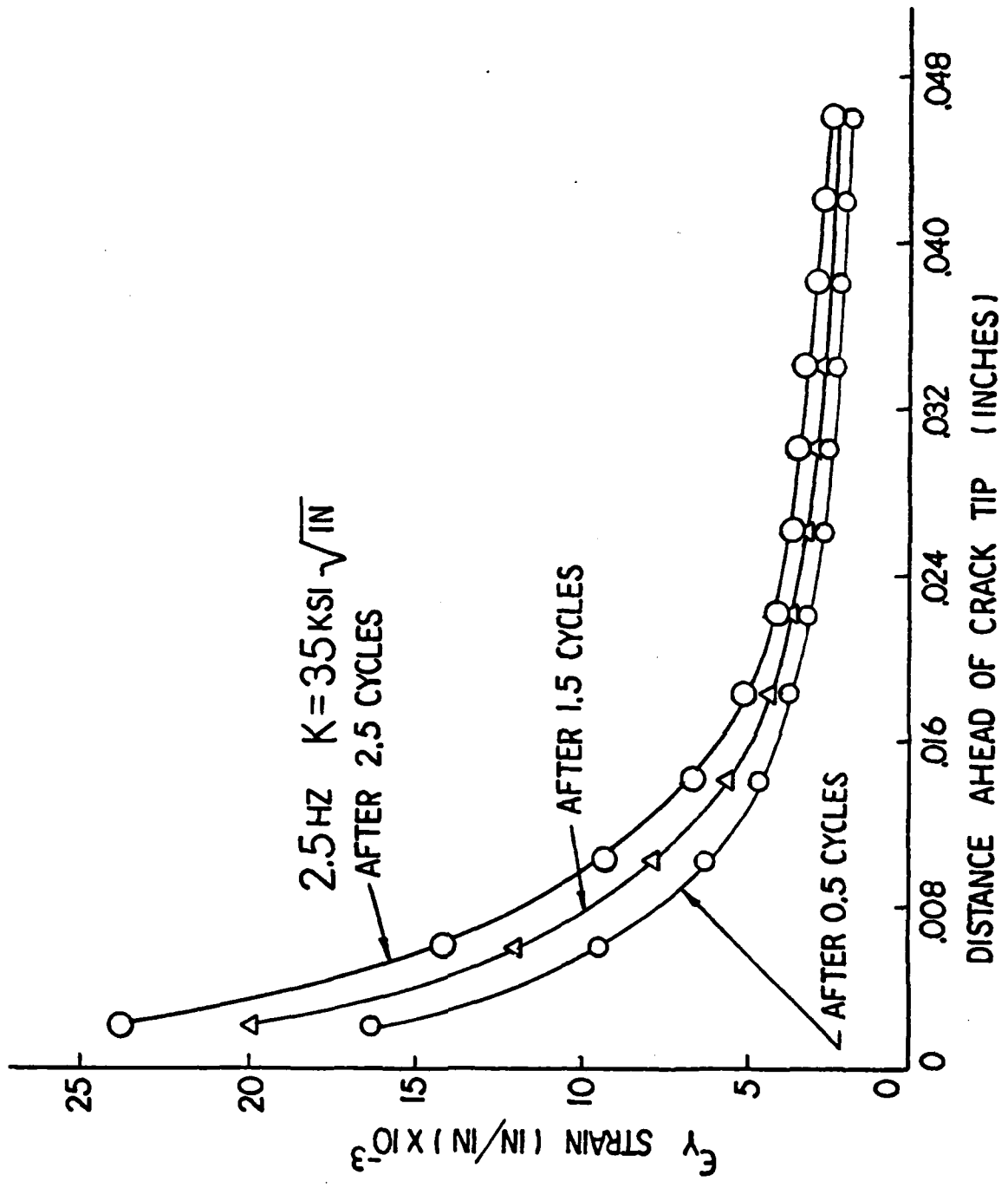


Fig 4.31 Y Strain vs Distance Ahead of Crack Tip

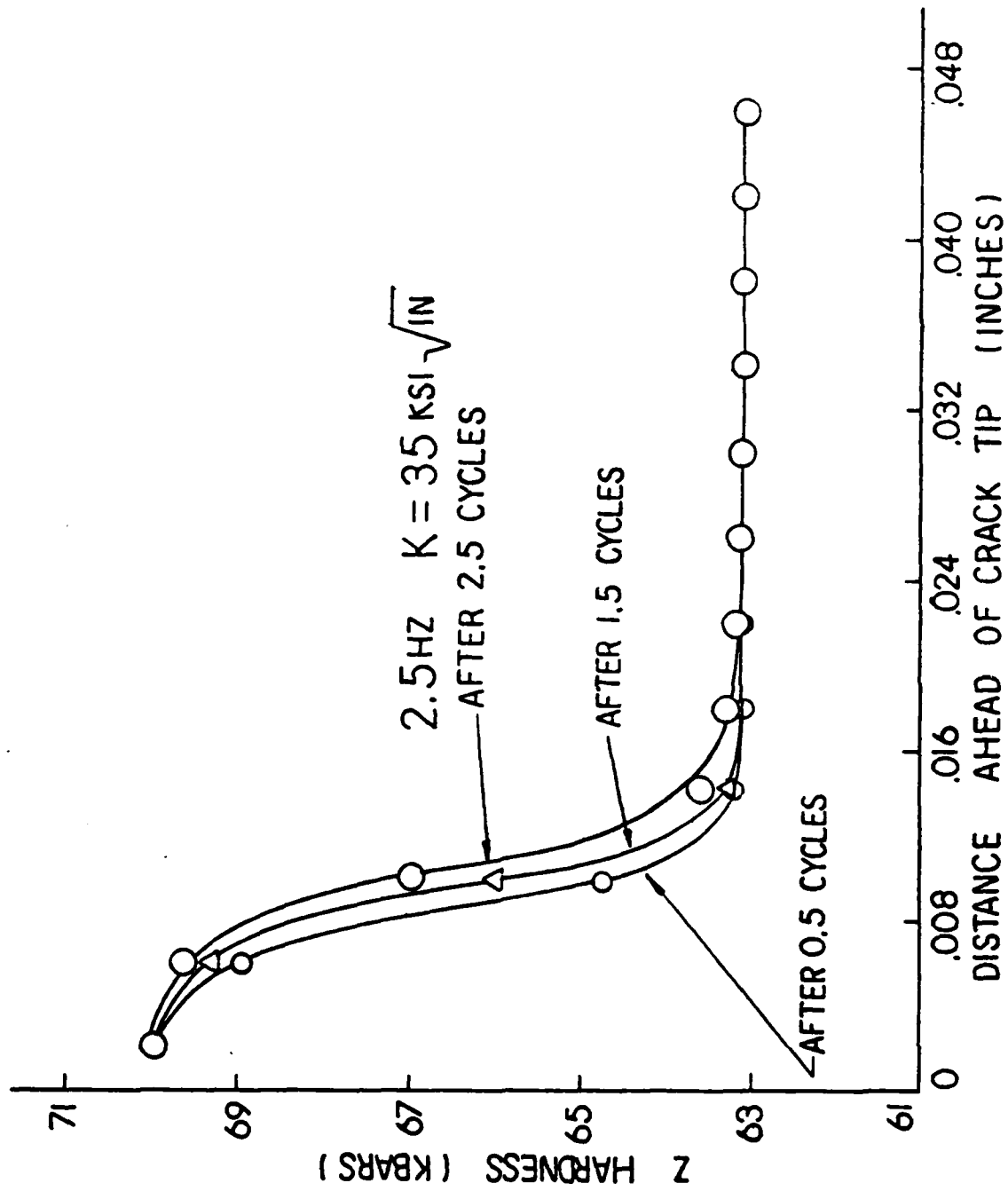


Fig 4.32 Z Hardness vs Distance Ahead of Crack Tip

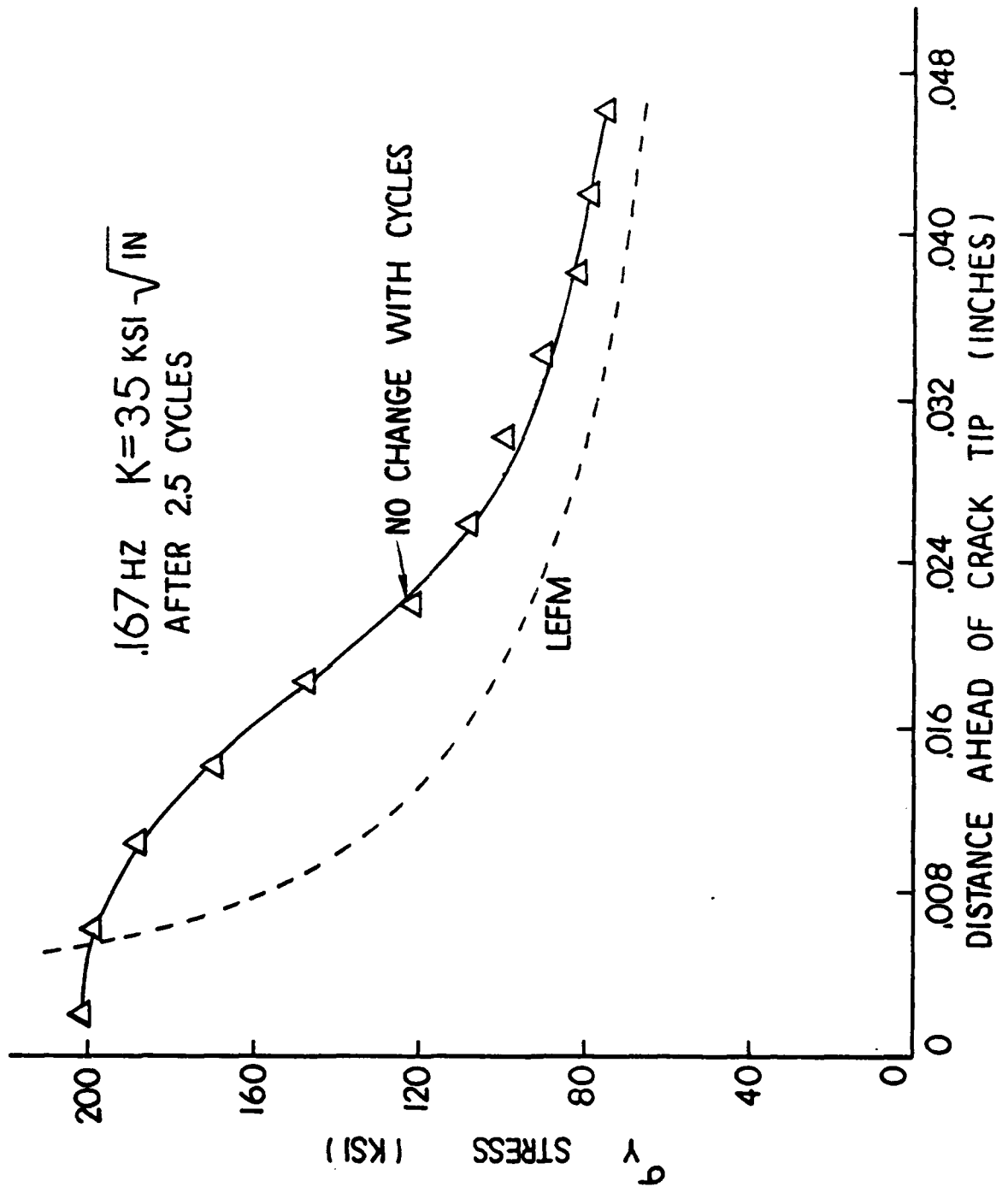


Fig 4.33 Y Stress vs Distance Ahead of Crack Tip

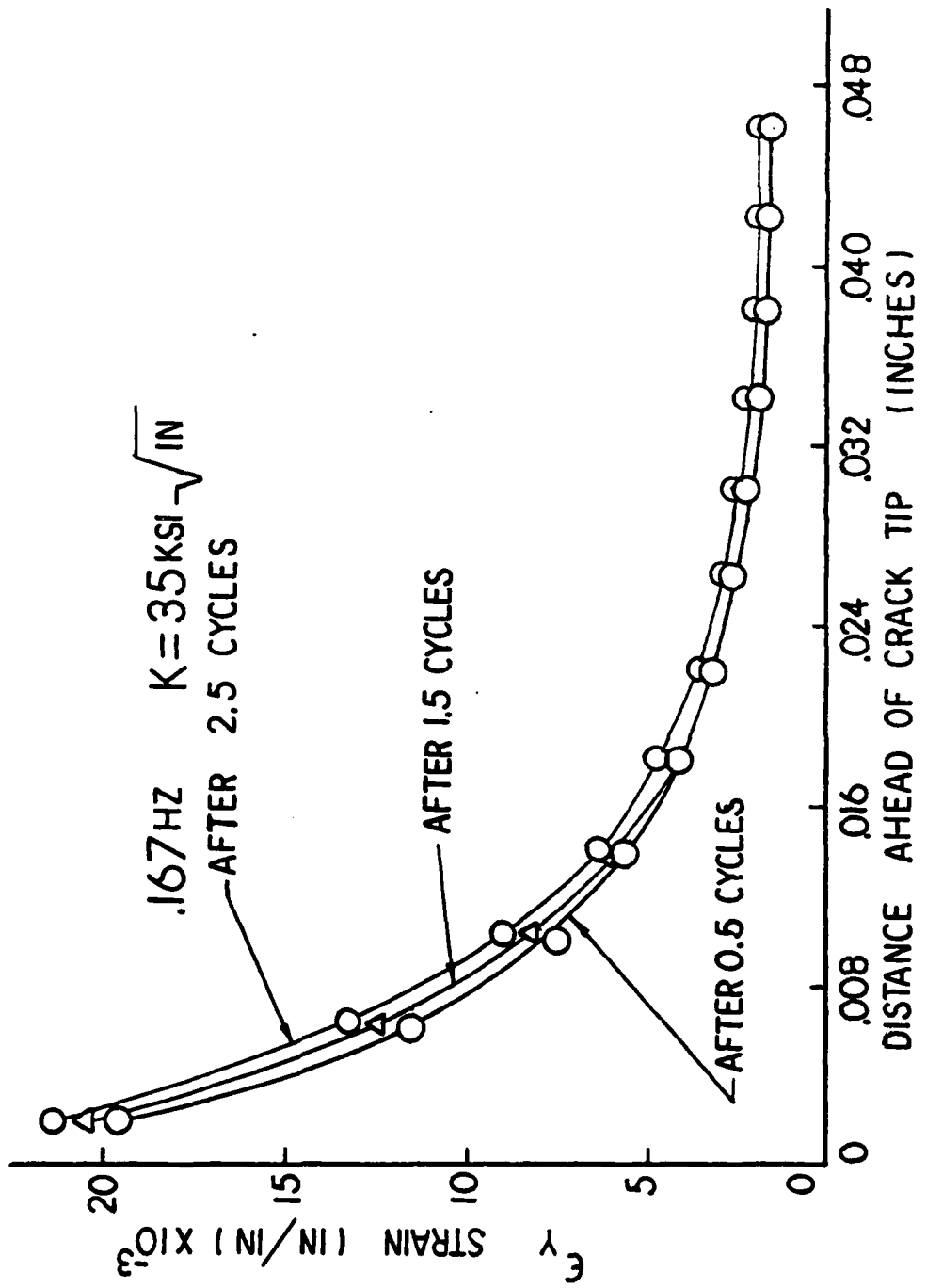


Fig 4.34 Y Strain vs Distance Ahead of Crack Tip

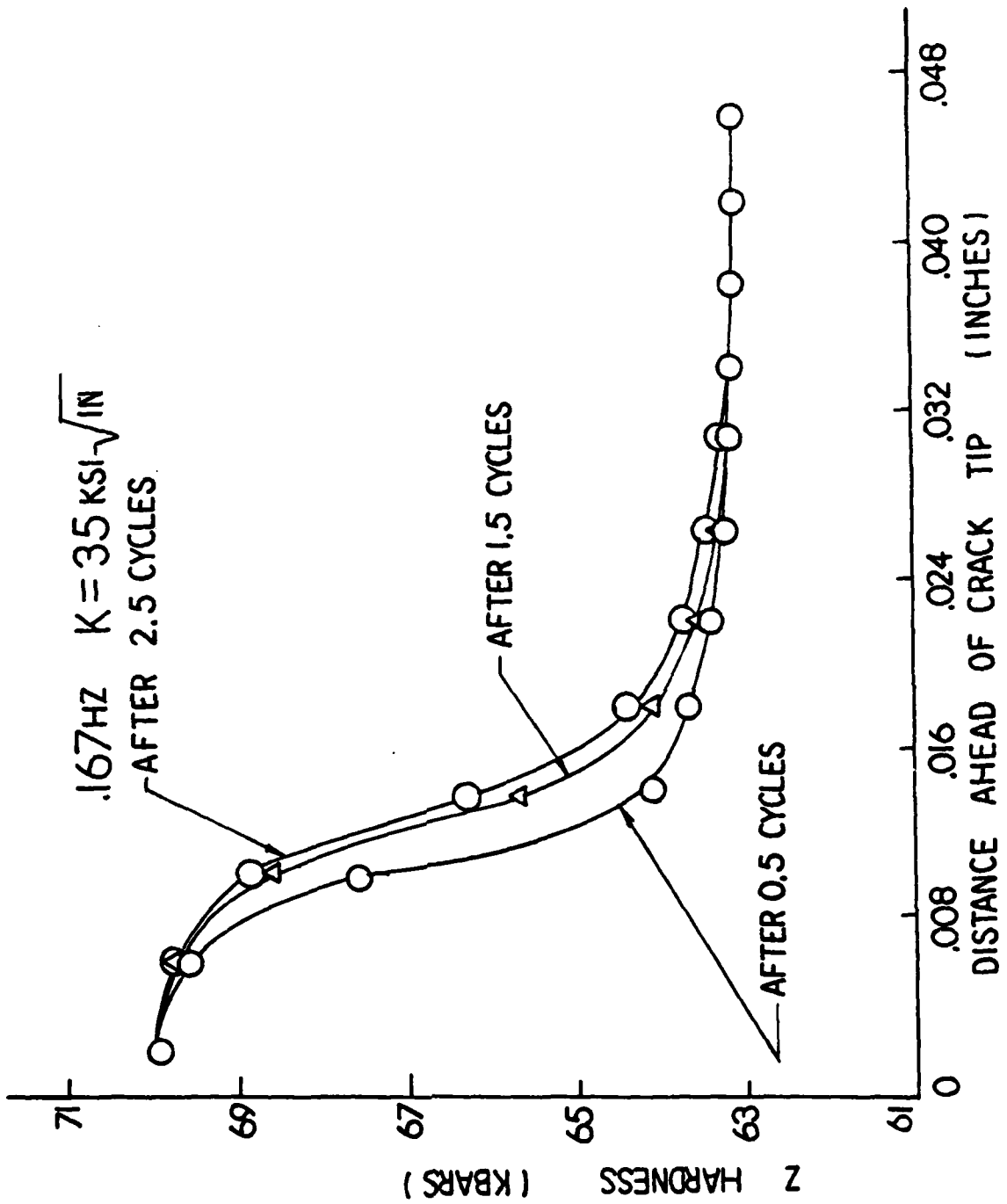


Fig 4.35 Z Hardness vs Distance Ahead of Crack Tip

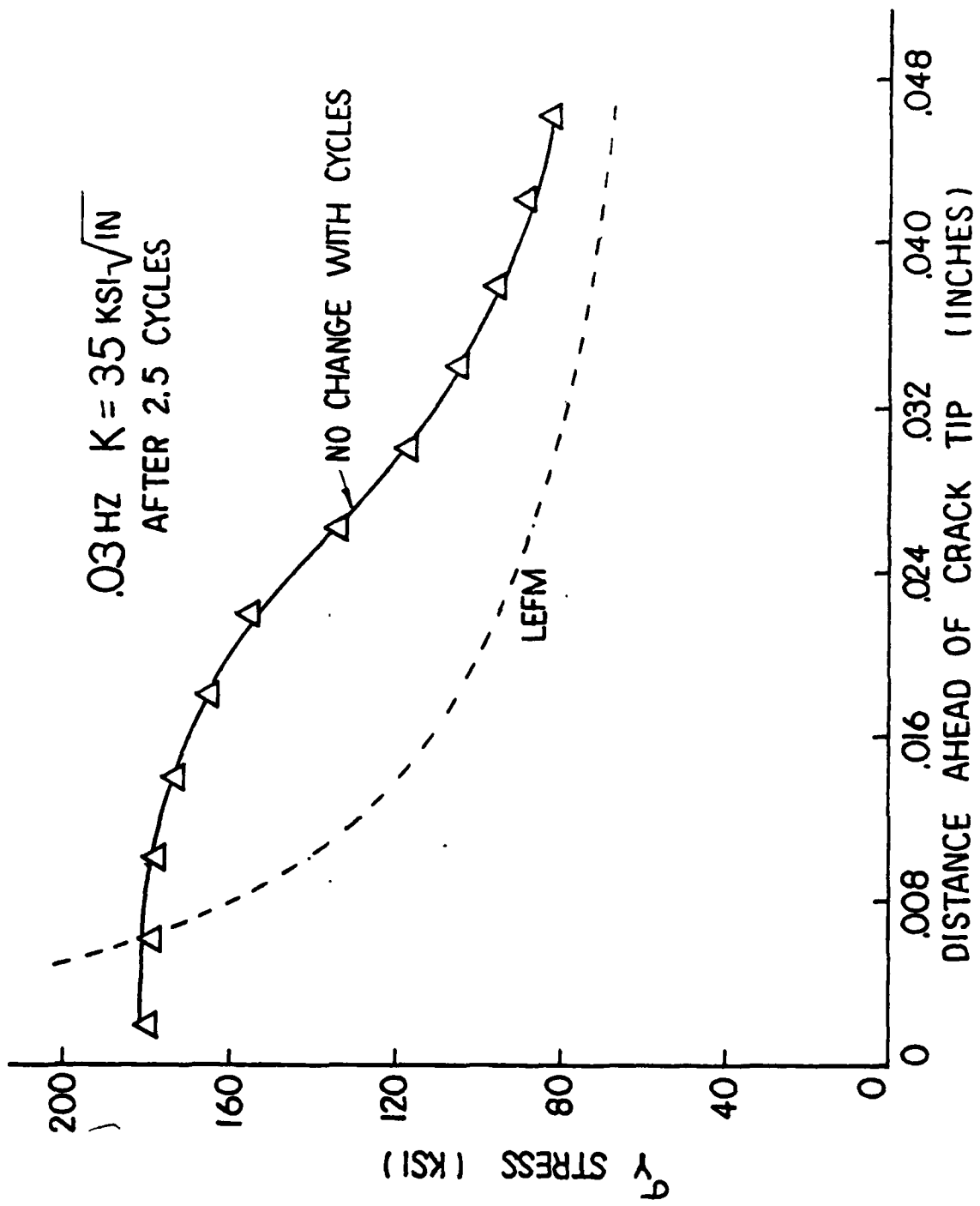


Fig 4.36 Y Stress vs Distance Ahead of Crack Tip

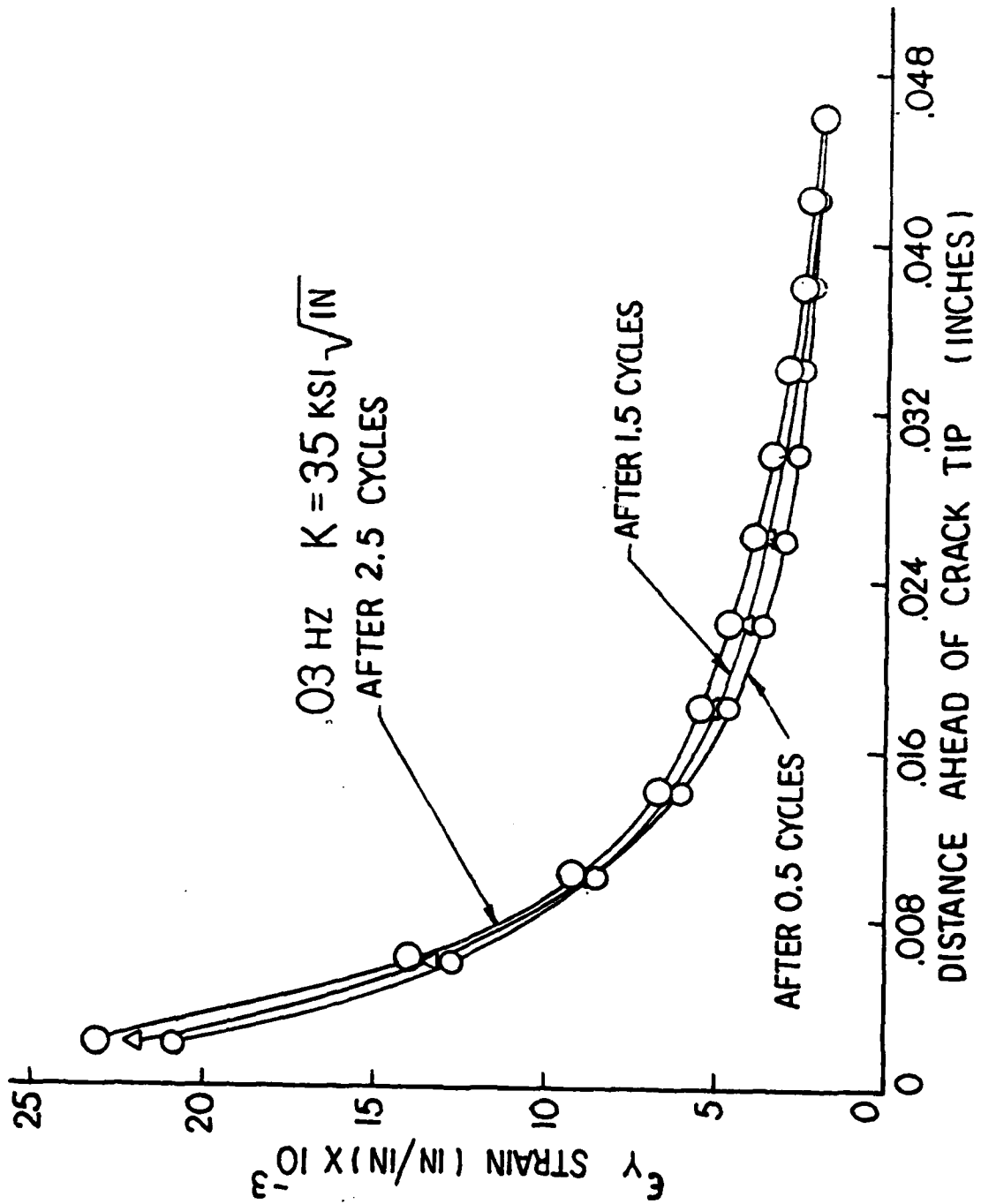


Fig 4.37 Y Strain vs Distance Ahead of Crack Tip

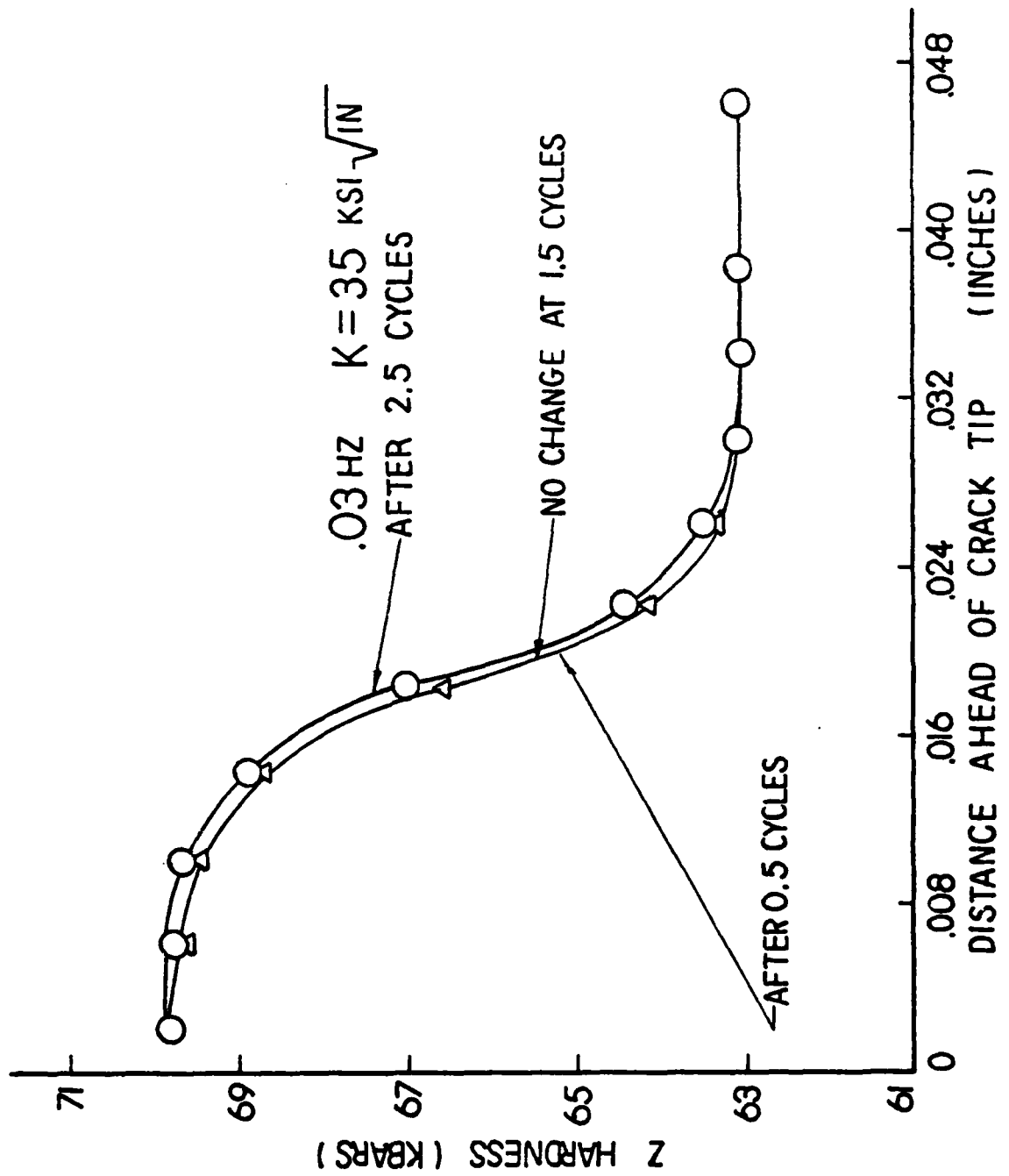


Fig 4.38 Z Hardness vs Distance Ahead of Crack Tip

Results of a typical overload condition are displayed in Fig's. 4.39-4.41. The load was cycled at a stress intensity factor of $45\text{KSI}\sqrt{\text{in}}$ for two cycles. Load cycling was stopped when the stress intensity factor rose to $35\text{KSI}\sqrt{\text{in}}$ during the next half cycle. Stress, strain and Z hardness values shown represent the effect of overload. It can be seen that overload increases plastic deformation near the crack tip, retarding future crack growth. This verifies laboratory overload fatigue crack growth studies conducted by Larsen and Nicholas [14].

Numerous studies have shown crack closure in center cracked panels during cycles unload [15]. To check for crack closure, vertical (y) displacements behind the crack tip were continuously monitored during the unload cycle. As shown in Fig's. 4.42-4.46 no negative displacements were observed, indicating no crack closure. Lack of closure may be attributed to both specimen geometry and to the positive load levels (stress ratio of 0.1) throughout the unload half cycle. The compact tension specimen geometry can be thought of as a cantilever beam with a positive end load with the fixed support at the crack tip. With this in mind it can be seen that one would not expect closure (negative) displacements at the crack tip.

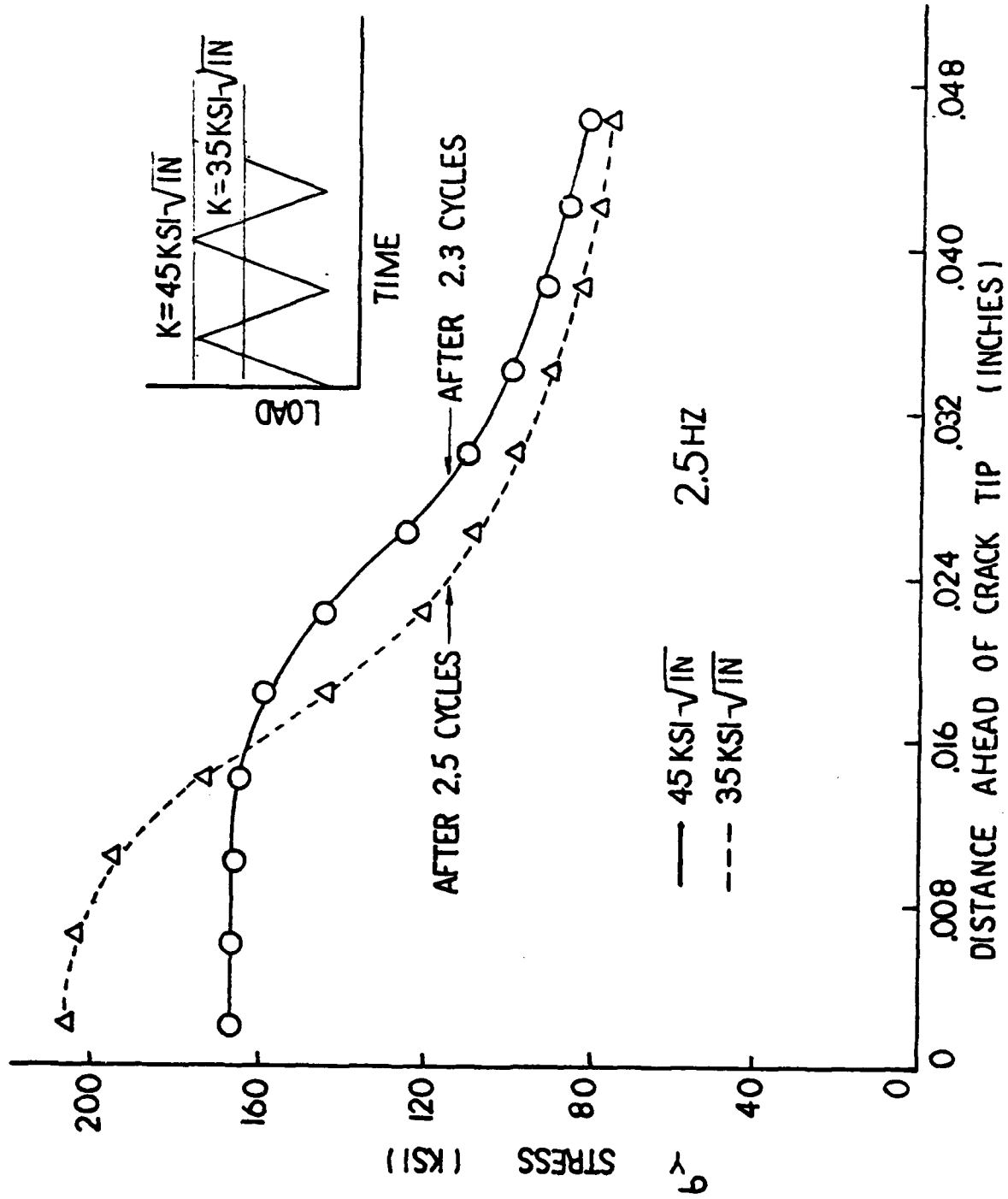


Fig 4.39 Y Stress vs Distance Ahead of Crack Tip
Considering Overstress

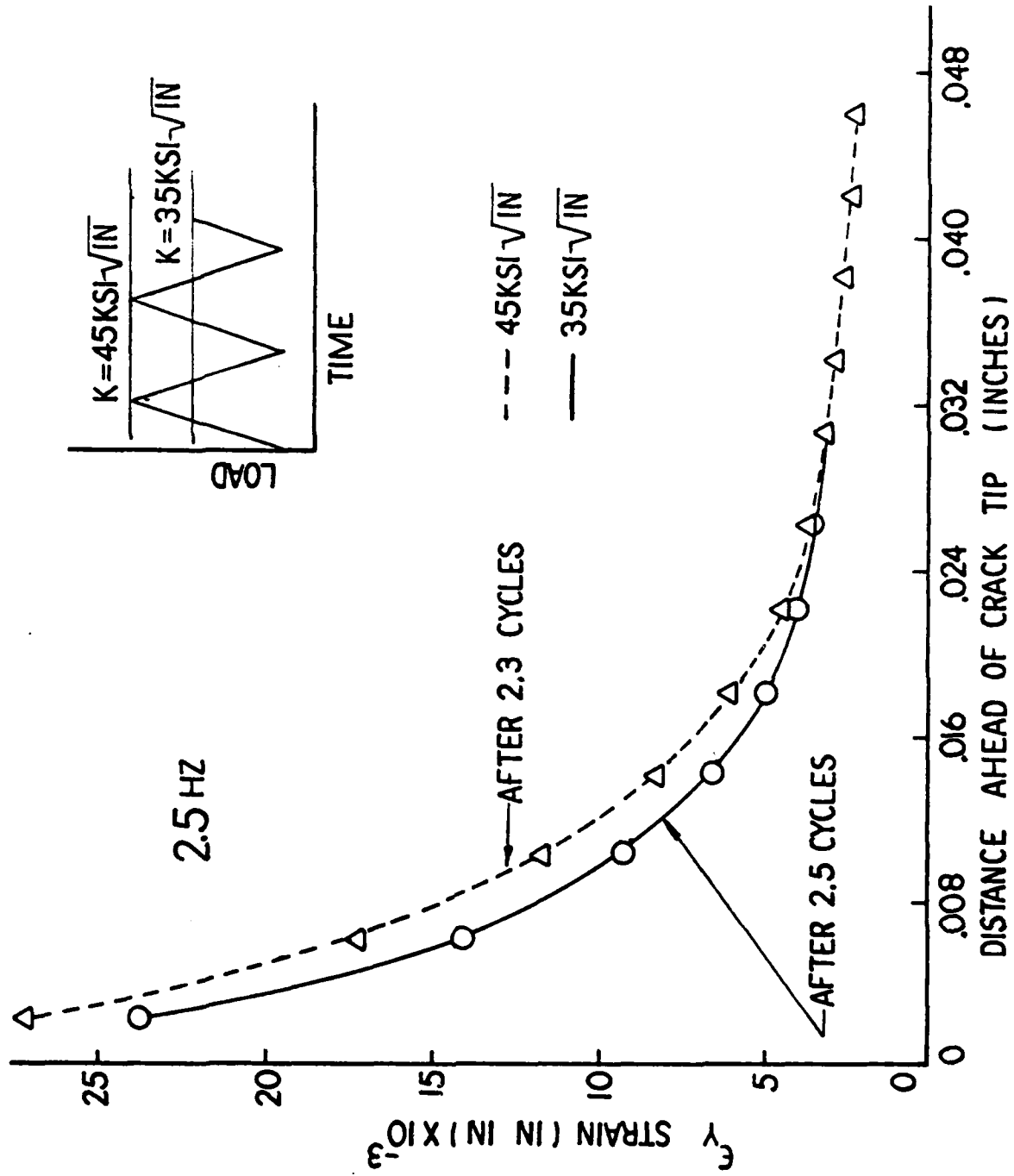


Fig 4.40 Y Strain vs Distance Ahead of Crack Tip
Considering Overstress

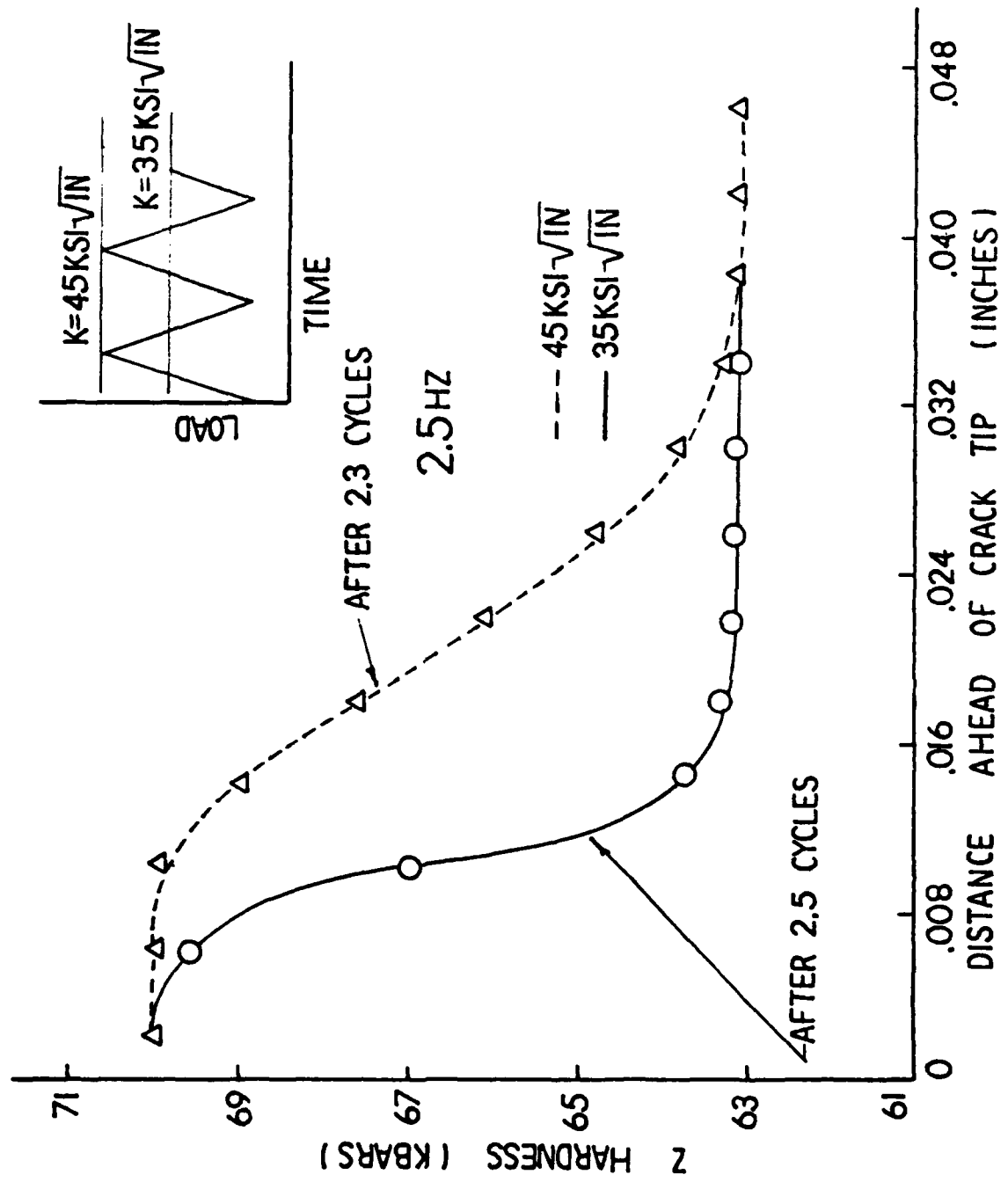


Fig 4.41 Z Hardness vs Distance Ahead of Crack Tip
Considering Overstress

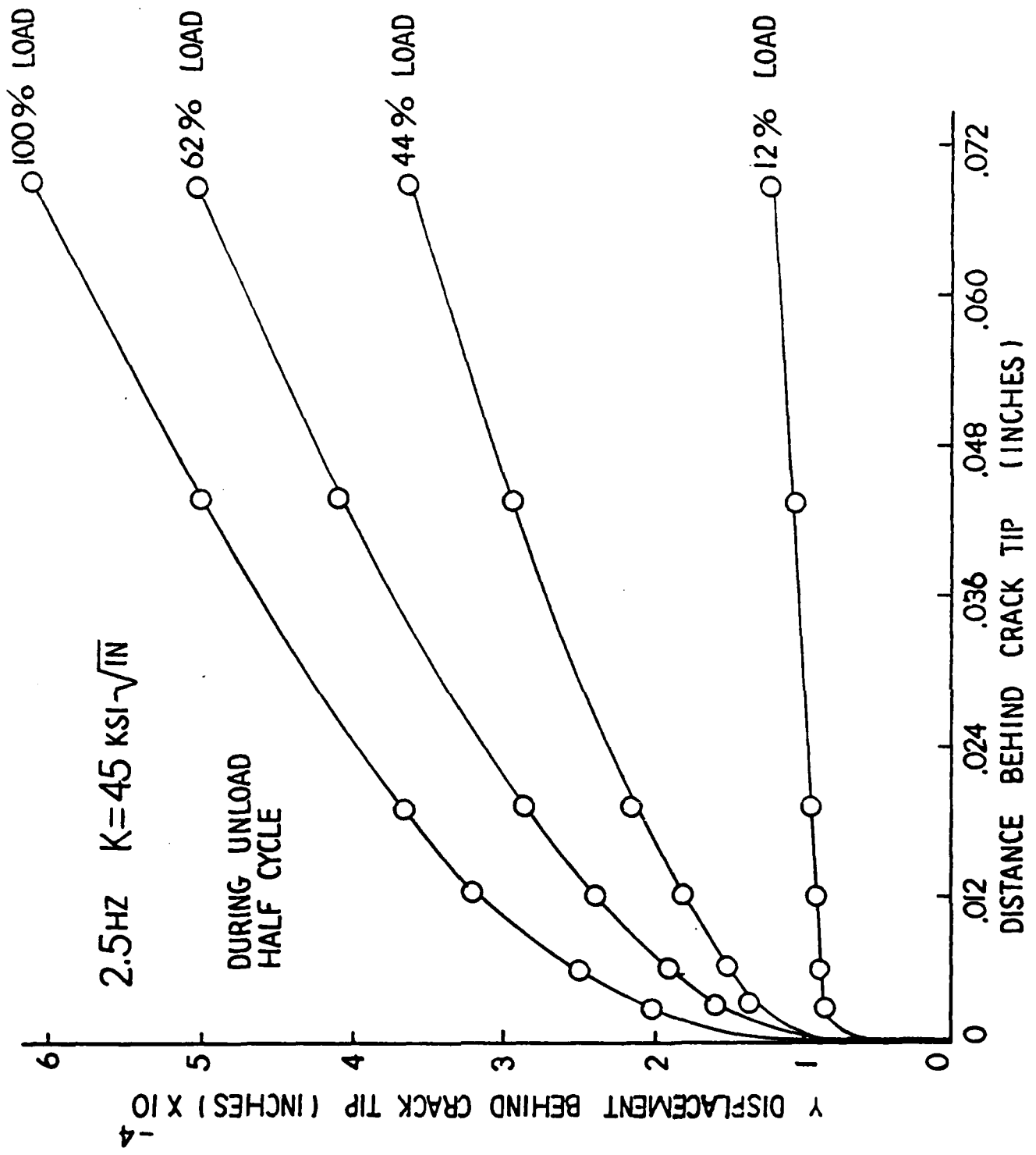


Fig 4.42 Y Displacement vs Distance Behind Crack Tip
During Unload

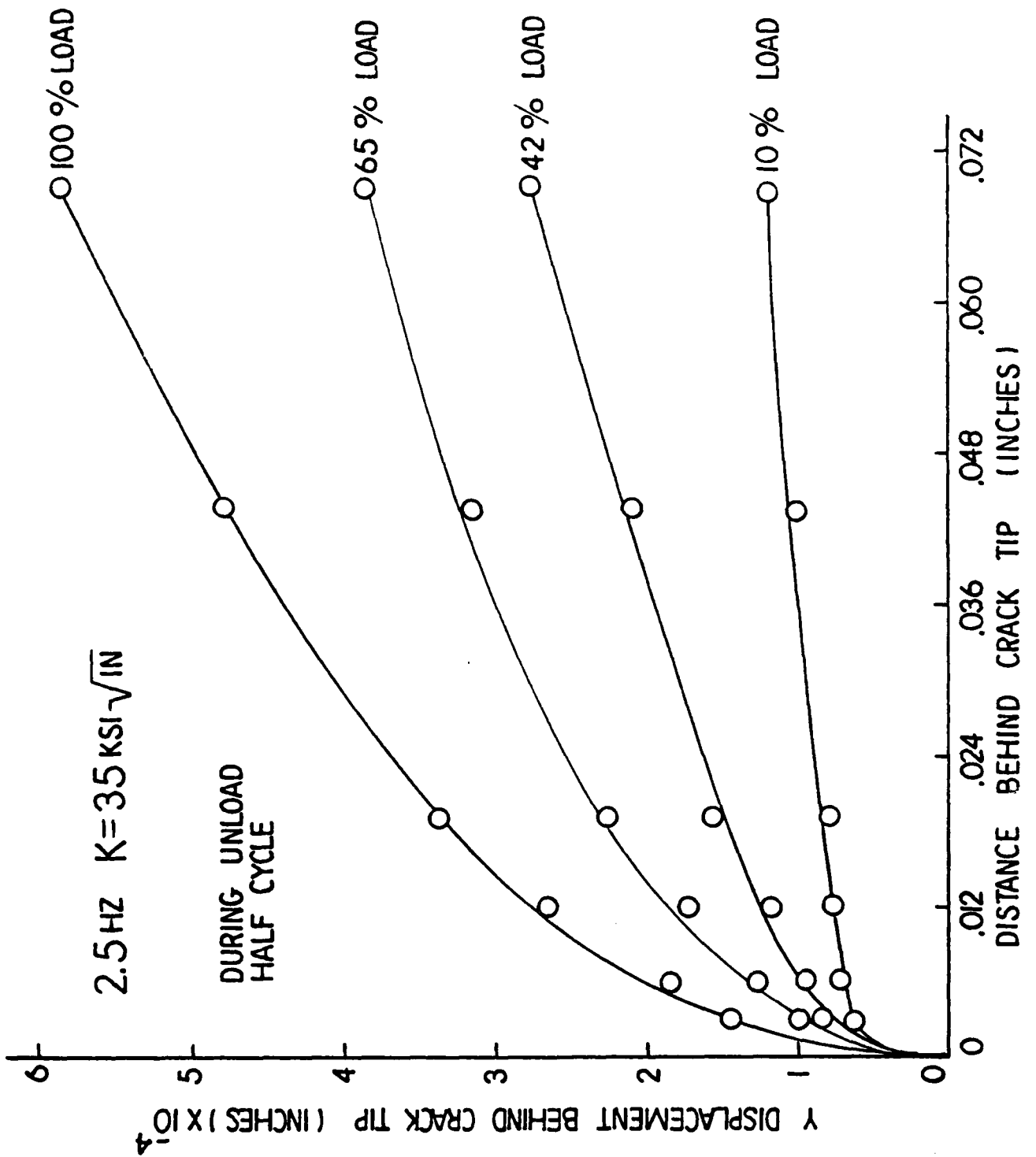


Fig 4.43 Y Displacement vs Distance Behind Crack Tip
During Unload

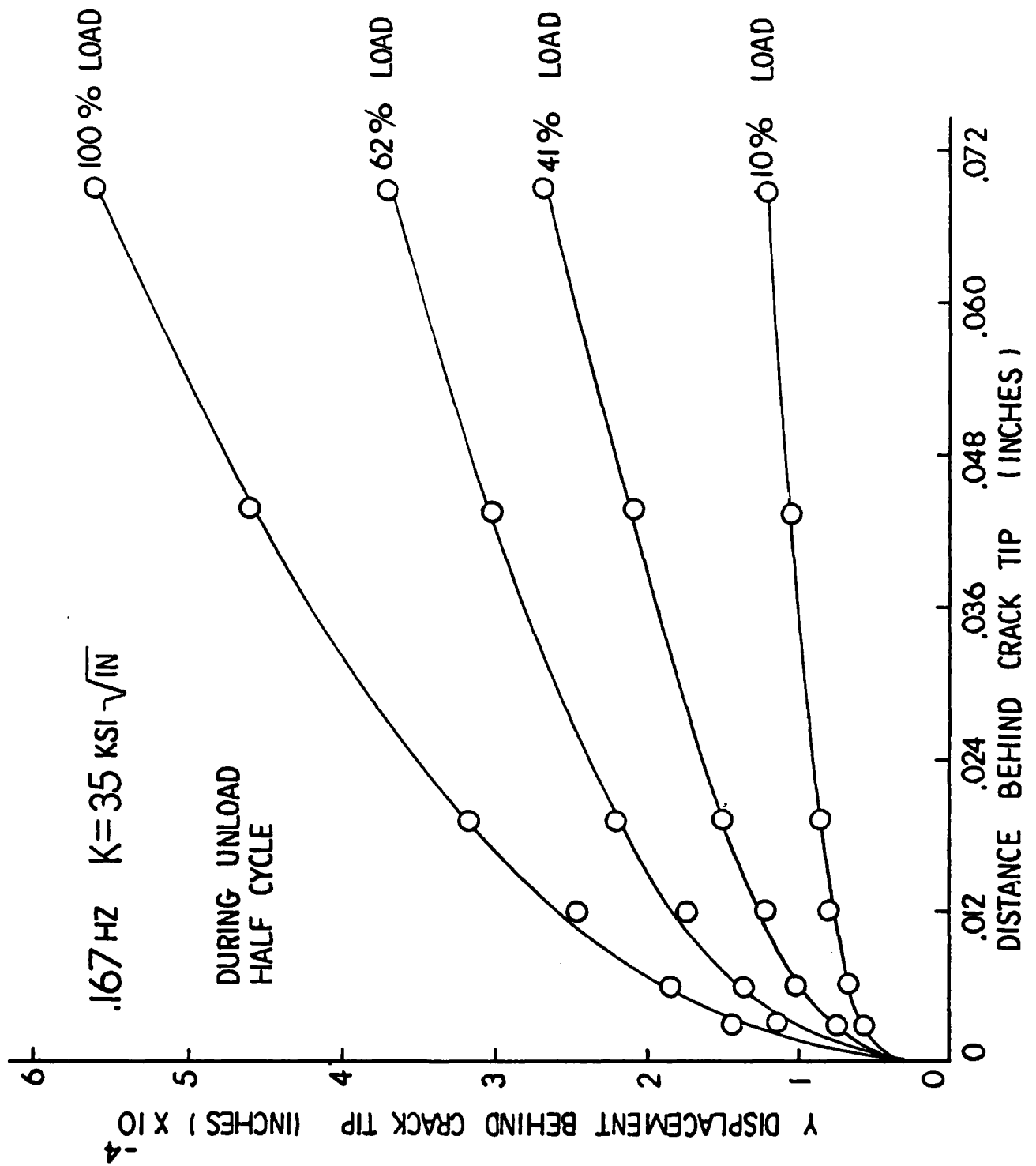


Fig 4.44 Y Displacement vs Distance Behind Crack Tip

During Unload

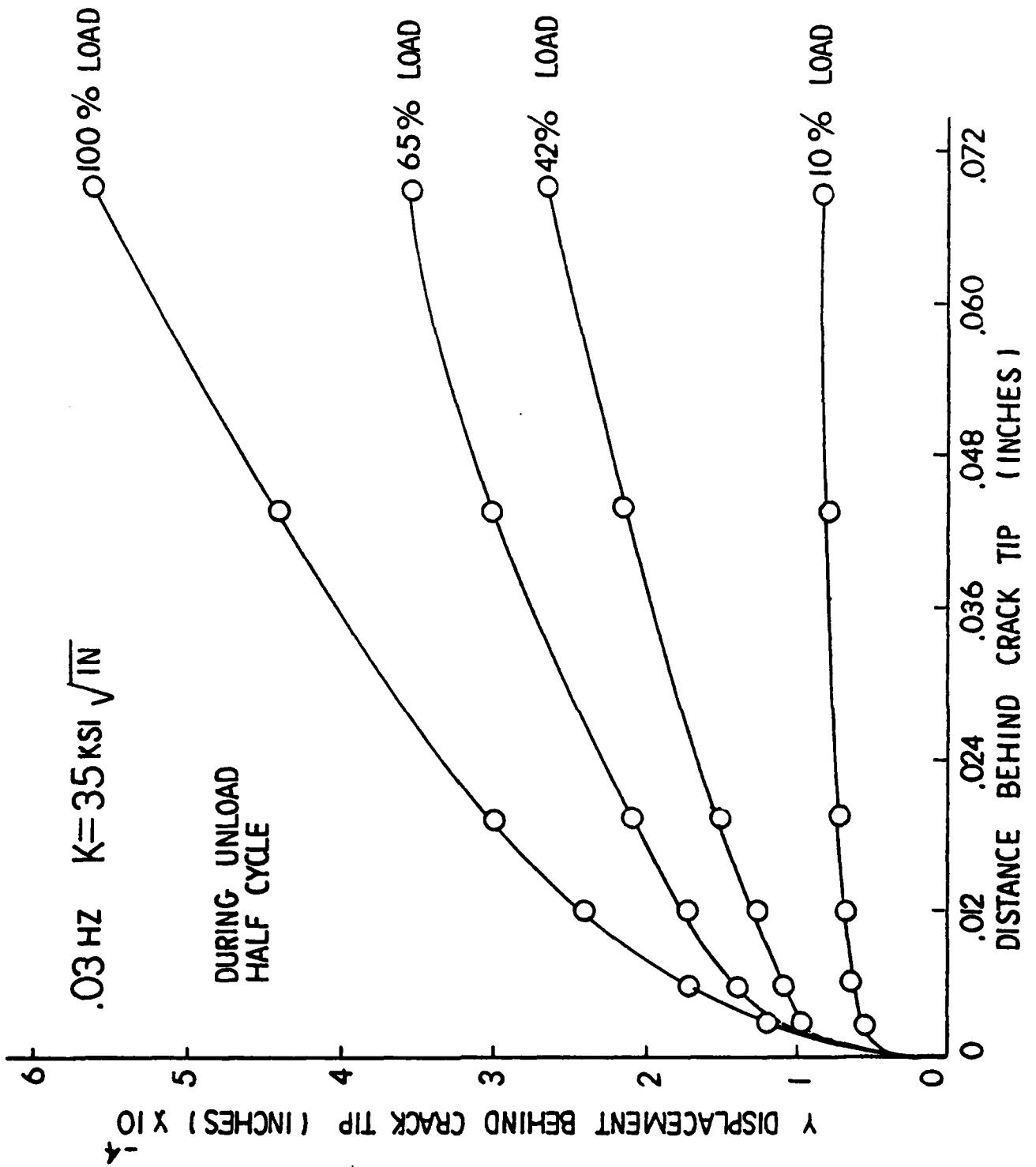


Fig 4.45 Y Displacement vs Distance Behind Crack Tip
During Unload

Throughout this study, it was speculated that at stress levels below 165KSI near the crack tip, the compact tension specimen behaved elastically and that plastic deformation produced negligible effects. To verify this premise, an averaging process was undertaken. The load was cycled through 4.5 cycles. After 4.5 cycles, the finite elements which had plastic strain values at or above 10^{-3} in/in were considered plastic. By averaging stresses and total strains for all plastic elements, the stress-strain curves (Fig's. 4.46-4.47) were plotted. At 2.5Hz and $K=35$ KSI in the compact tension specimen reached a "quasi-steady state" after 2.5 cycles. Additional cycling produced negligible shifts in the stress-strain curve. Peak stresses averaged 165KSI at the crack tip over the plastic zone. At 0.03Hz, no such "steady state" condition was evident. Similar observations were made with uniaxial results at the same stress levels.

To observe overall effects of load cycling, extended hold, and node release, the load was cycled at 2.5Hz at a stress intensity factor of 35KSI in for 2.5 cycles. After cycling, the load was held at a constant stress intensity factor, for fifteen minutes followed by node release. Results shown in Fig's. 4.48-4.49 depict plastic zone growth with the load cycling. Comparing Fig's. 4.49 with 4.50 shows there is little change in plastic zone size during the sustained hold period.

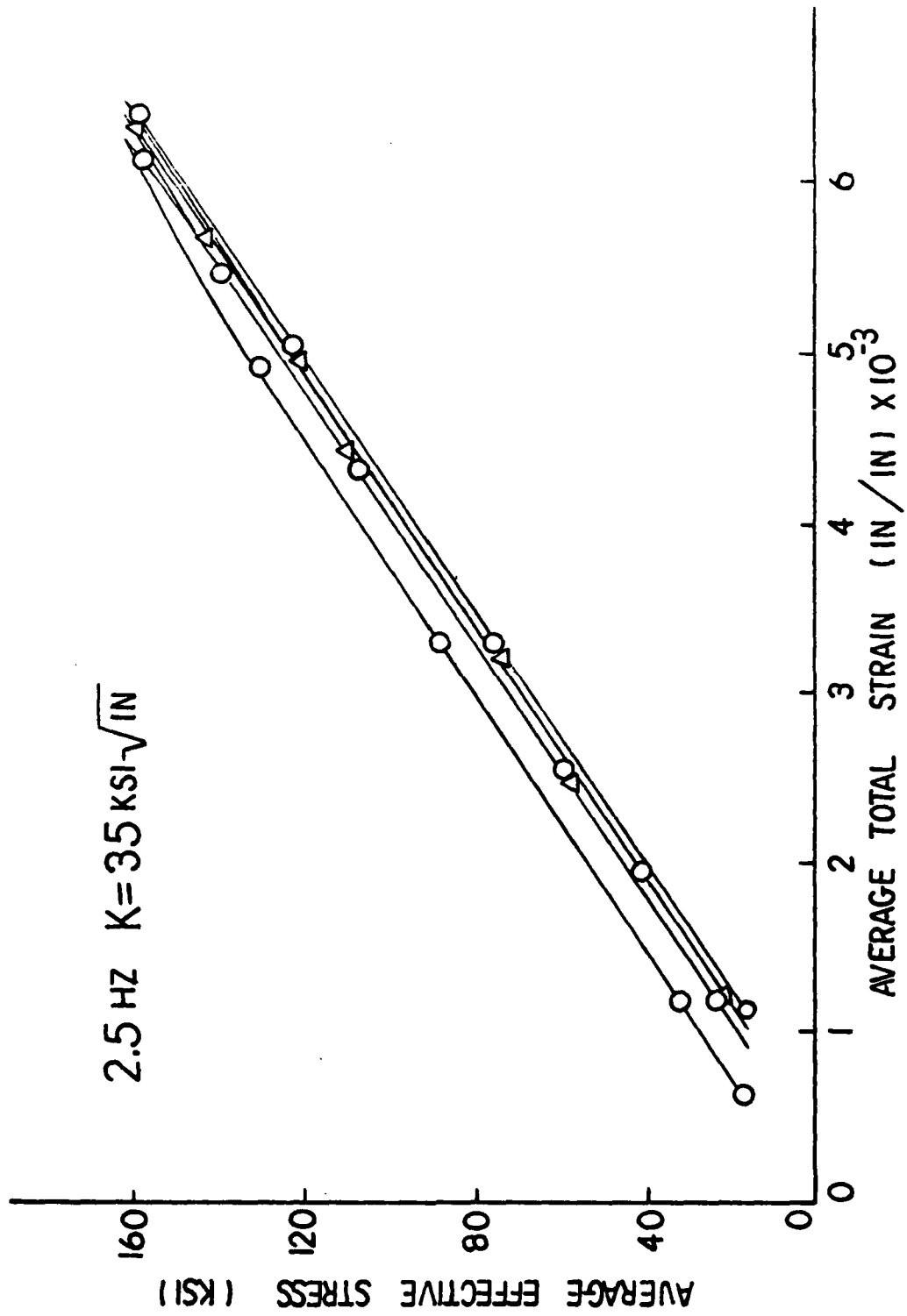


Fig 4.46 Average Effective Stress vs Average Total Strain
Near Crack Tip

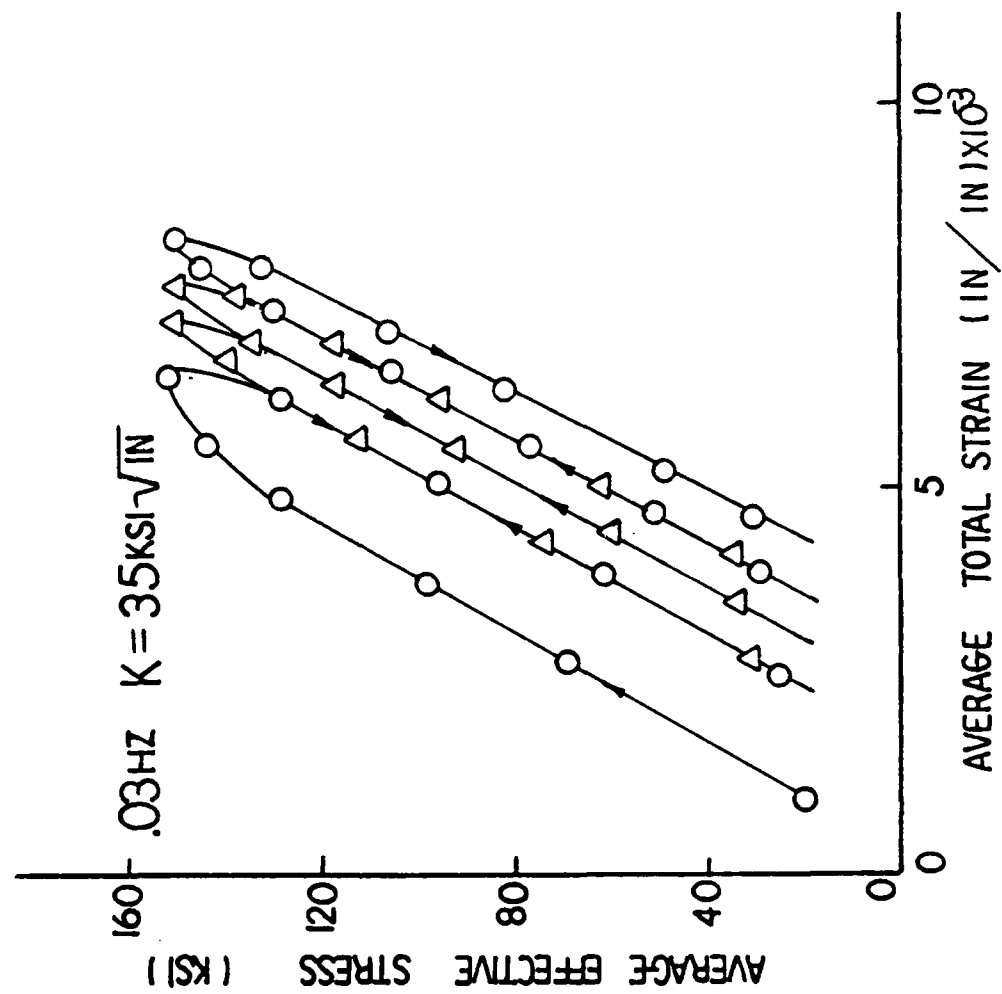


Fig 4.47 Average Effective Stress vs Average Total Strain
 Near Crack Tip

The stress field ahead of the crack tip changes little during the sustained hold and during node release (see Fig. 4.52). However, straining continues to increase slightly (Fig. 4.53). It should be noted that after node release, the Y strain (ϵ_y) is coincident with the strain curve prior to node release. In addition, it must be realized that the stress-strain field has translated one finite element to the new crack tip. The plastic zone ahead of the crack tip is approximately the same size as it was prior to node release. (Fig's. 4.50-4.51) As expected, the Z hardness parameter decreased during hold period (see Fig. 4.54). During the sustained hold, the rate of plastic deformation (strain rate) decreased due to the absence of load cycling, allowing the rate of thermal hardness recovery (\dot{Z}_{rec} , equation 2.24) to become more dominant. The decrease in Z hardness (strain hardening) indicates a gradual return toward an unhardened state.

Changes in plastic zone size with frequency are shown in Fig's. 4.48-4.49 and 4.55-4.60. It should be noted that as the frequency decreased the size of the plastic zone increased. This corresponds directly to uniaxial test results shown in this section.

Laboratory fatigue testing relies heavily on compliance measurements to acquire data. Little information is available as to compact tension specimen far field behavior. The far field behavior dictates the linearity or non-linearity of clip gauge measurements taken at the crack mouth. To this end, computer generated far field displacements (Y displacement) at the crack mouth (node 7) on the edge of the specimen were plotted during the load cycle for three frequencies and two

INCHES
SCALE 0 .002 .004

2.5HZ $K=35 \text{ KSI}\sqrt{\text{IN}}$

PLASTIC ZONE

AFTER 0.5 CYCLES

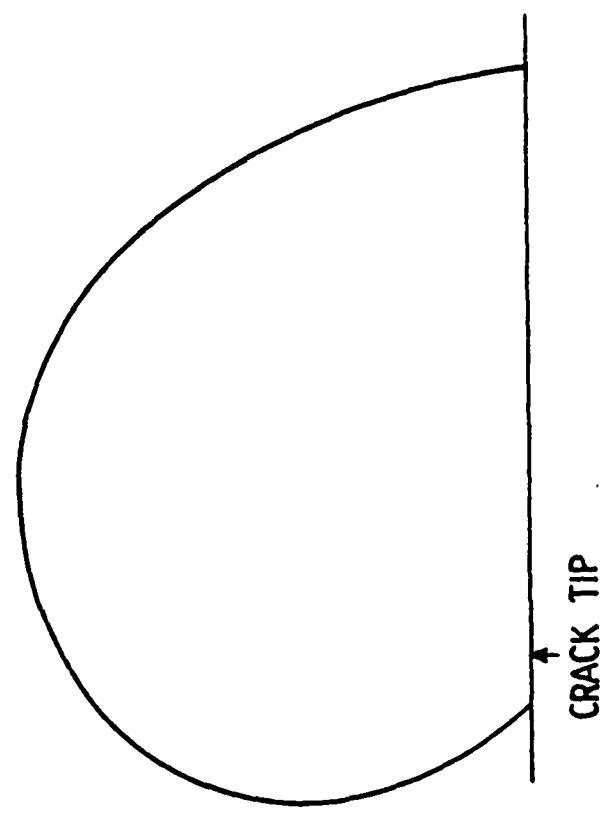


Fig 4.48 Plastic Zone After 0.5 Cycles

2.5HZ K=35 KSI $\sqrt{\text{IN}}$

SCALE INCHES
0 .002 .004

PLASTIC ZONE
AFTER 2.5 CYCLES

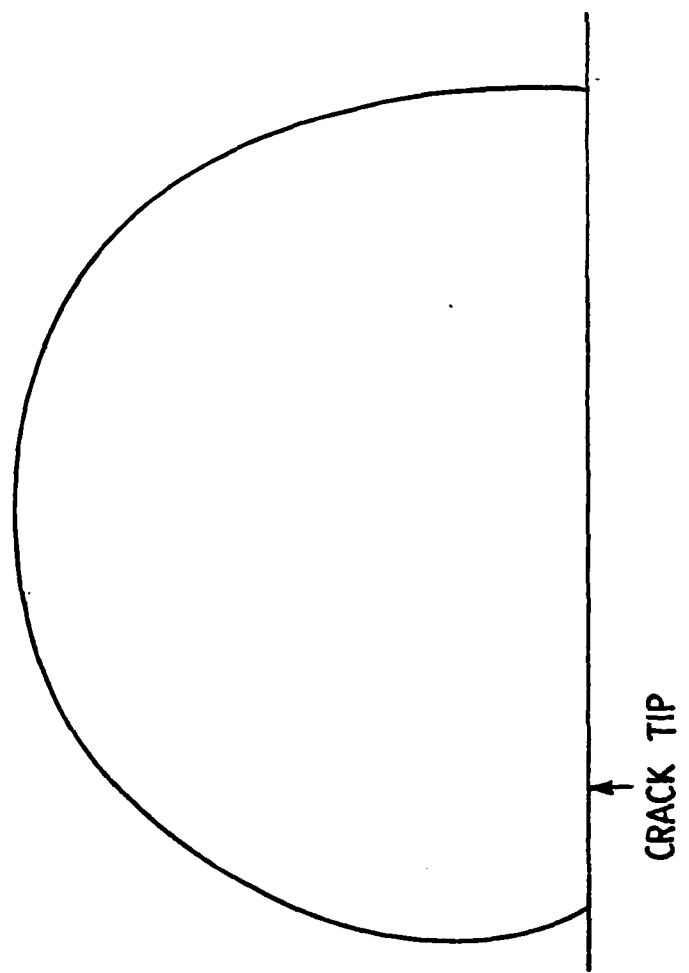


Fig 4.49 Plastic Zone After 2.5 Cycles

SCALE INCHES
0 .002 .004

$K = 35 \text{ KSI}\sqrt{\text{IN}}$

PLASTIC ZONE

AFTER 15 MIN. HOLD

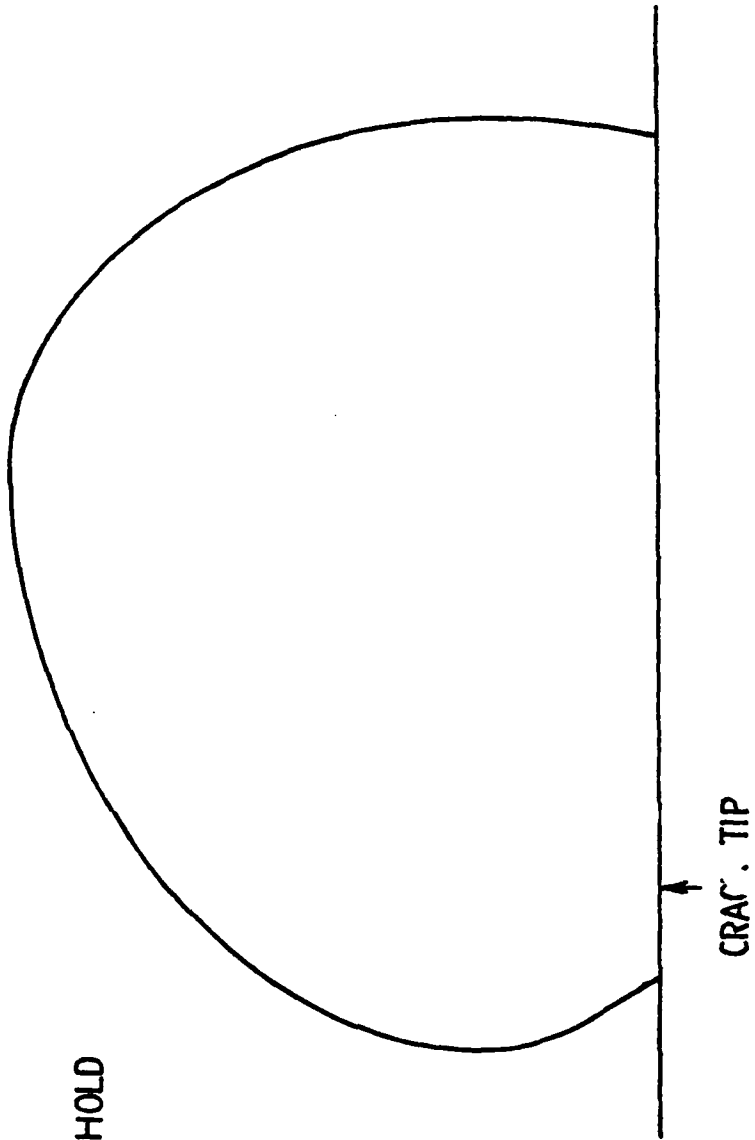


Fig 4.50 Plastic Zone After 15 Minute Hold

$K=35\text{KSI}\sqrt{\text{in}}$

SCALE
INCHES
0 .002 .004

$K = 35 \text{ KSI}\sqrt{\text{IN}}$

PLASTIC ZONE

AFTER NODE RELEASE

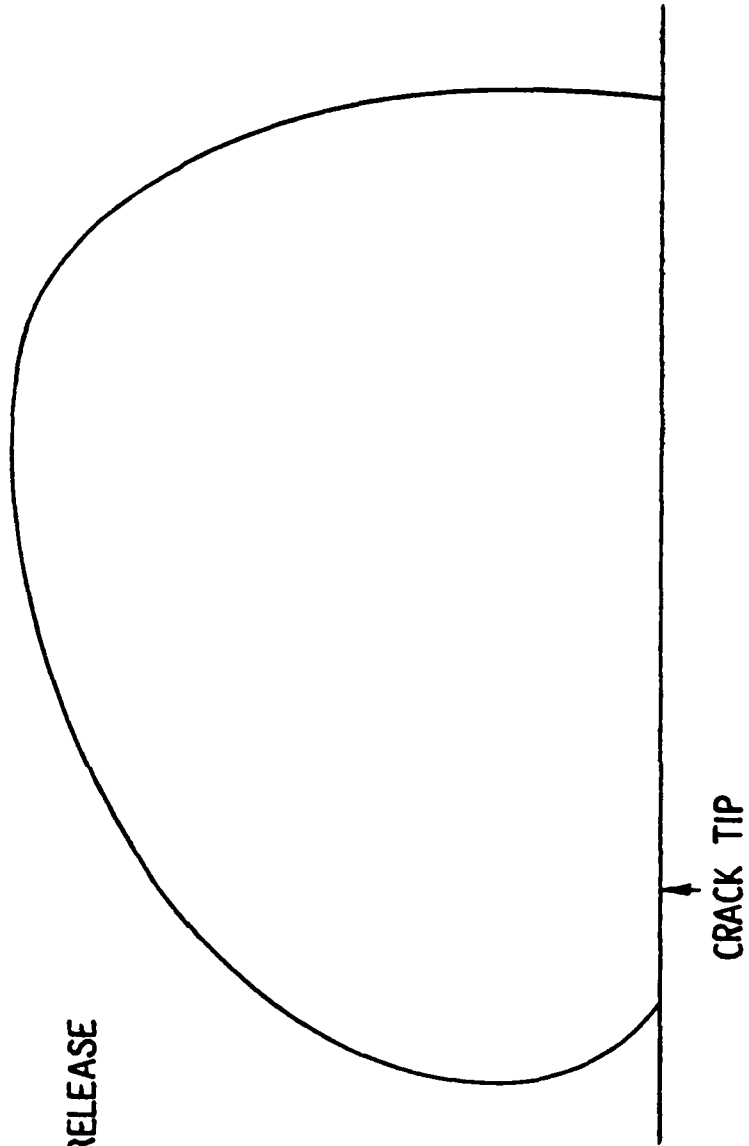


Fig 4.51 Plastic Zone After Node Release

$K=35\text{KSI}\sqrt{\text{in}}$

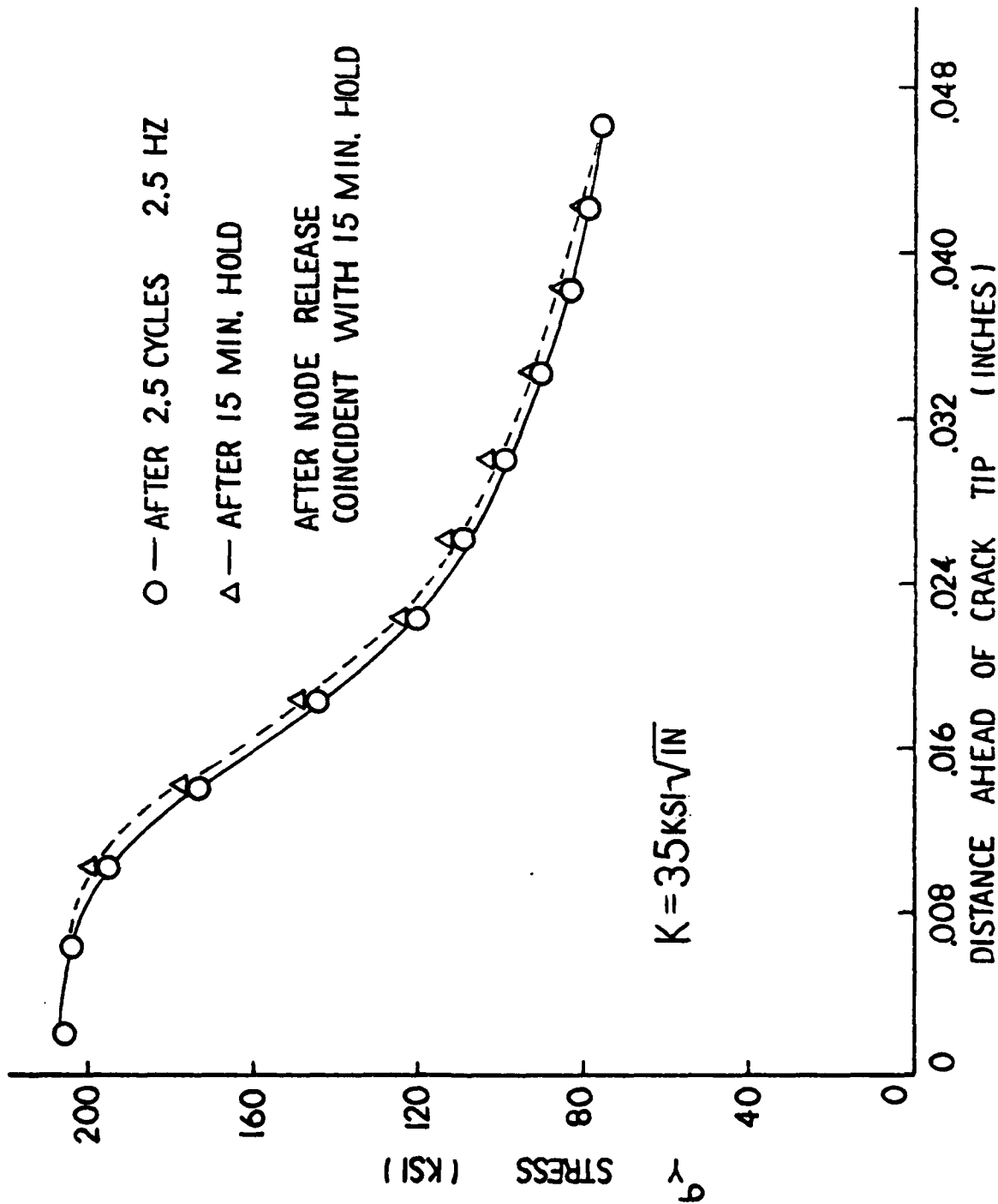


Fig 4.5² Y Stress vs Distance Ahead of Crack Tip
After 15 Minute Hold $K=35\text{KSI}\sqrt{\text{IN}}$

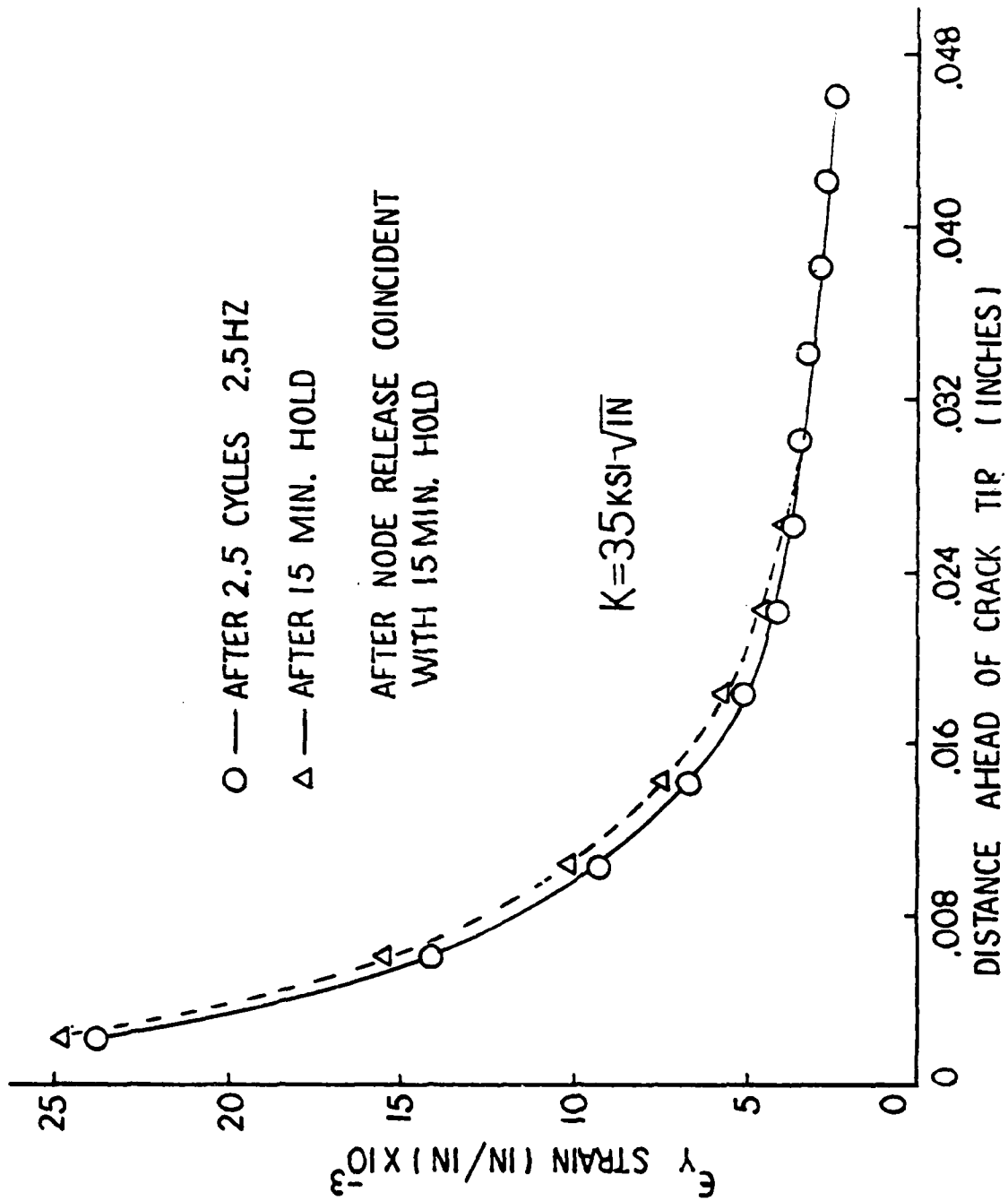


Fig 4.53 Y Strain vs Distance Ahead of Crack Tip
 After 15 Minute Hold $K=35\text{KSI}\sqrt{\text{in}}$

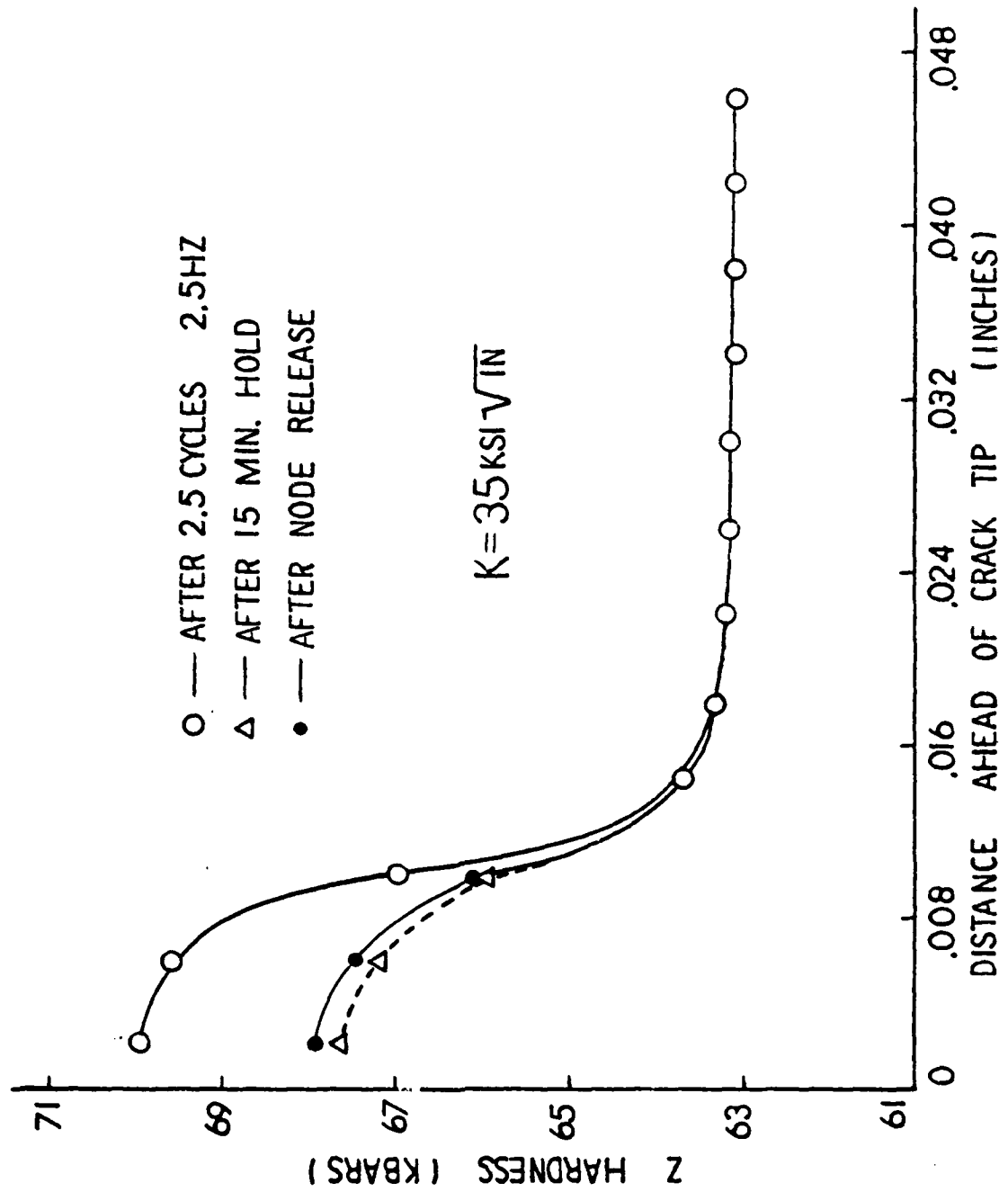
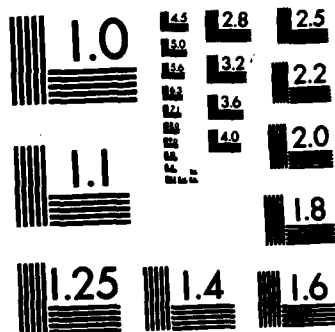


Fig 4.54 Z Hardness vs Distance Ahead of Crack Tip
 After 15 Minutes Hold $K=35\text{KSI}\sqrt{\text{in}}$



MICROCOPY RESOLUTION TEST CHART
NATIONAL BUREAU OF STANDARDS-1963-A

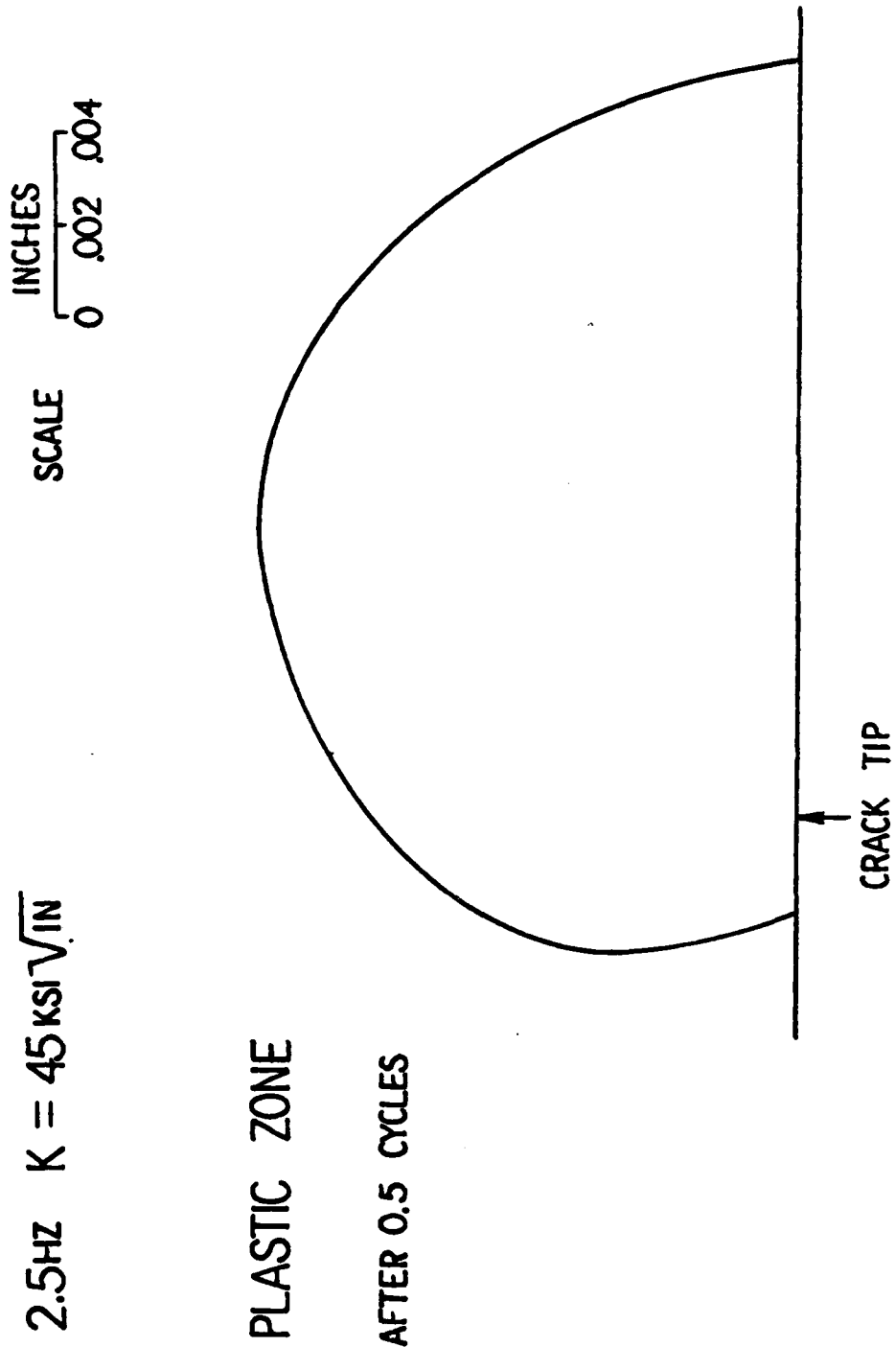


Fig 4.55 Plastic Zone After 0.5 Cycles 2.5Hz

$K=45\text{KSI}\sqrt{\text{in}}$

SCALE
INCHES
0 .002 .004

2.5HZ $K = 45 \text{ KSI} \sqrt{\text{IN}}$

PLASTIC ZONE
AFTER 2.5 CYCLES

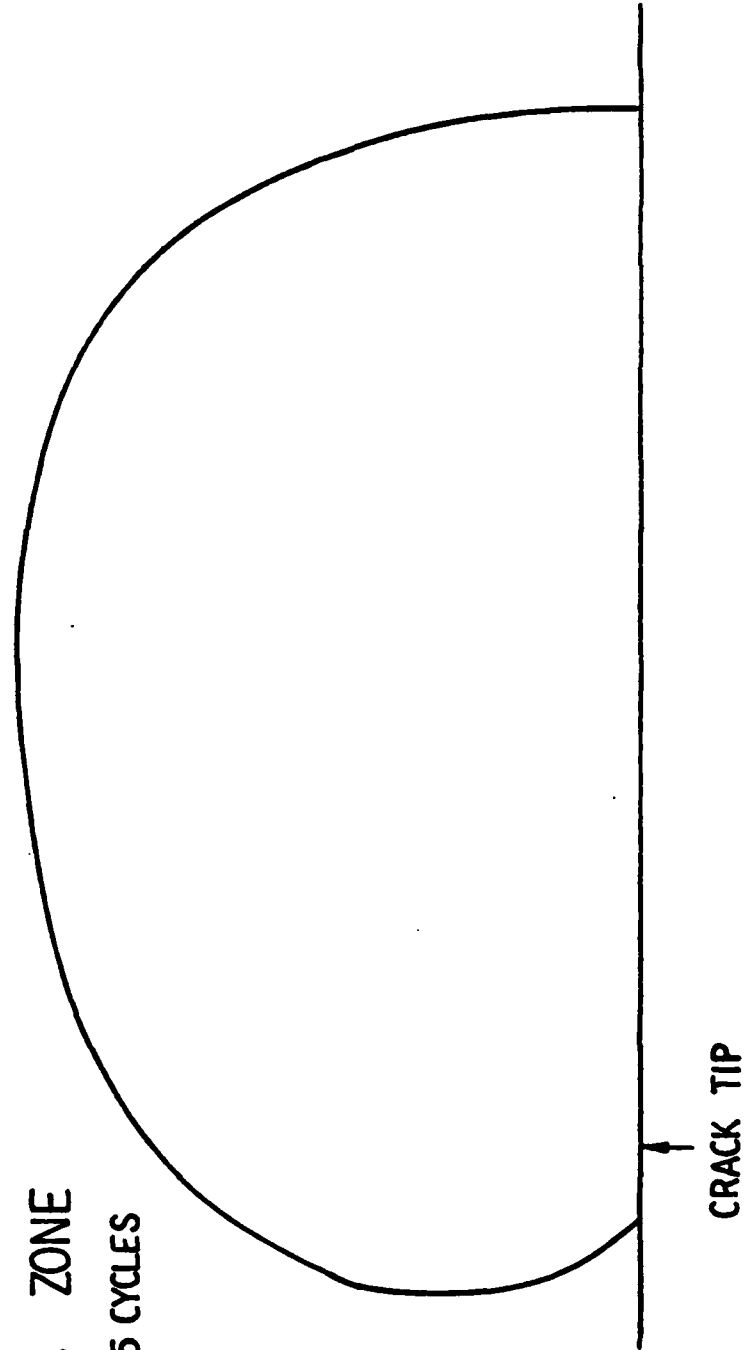


Fig 4.56 Plastic Zone After 2.5 Cycles 2.5Hz

$$K = 45 \text{ KSI} \sqrt{\text{IN}}$$

SCALE INCHES
0 .002 .004

.167HZ $K = 35 \text{ KSI} \sqrt{\text{IN}}$

PLASTIC ZONE
AFTER 0.5 CYCLES

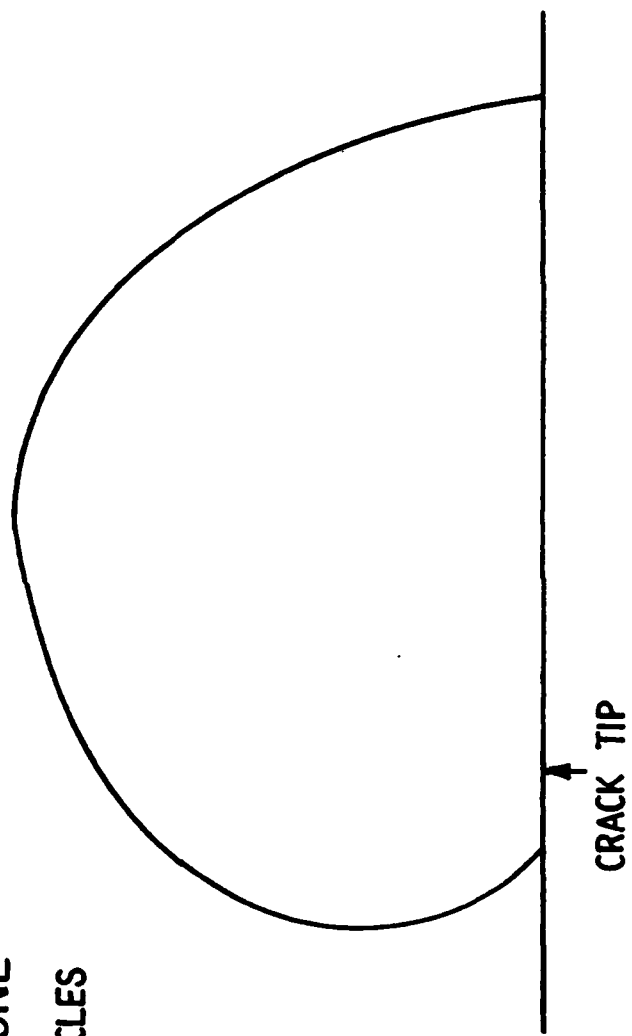


Fig 4.57 Plastic Zone After 0.5 Cycles

.167Hz $K=35\text{KSI}\sqrt{\text{IN}}$

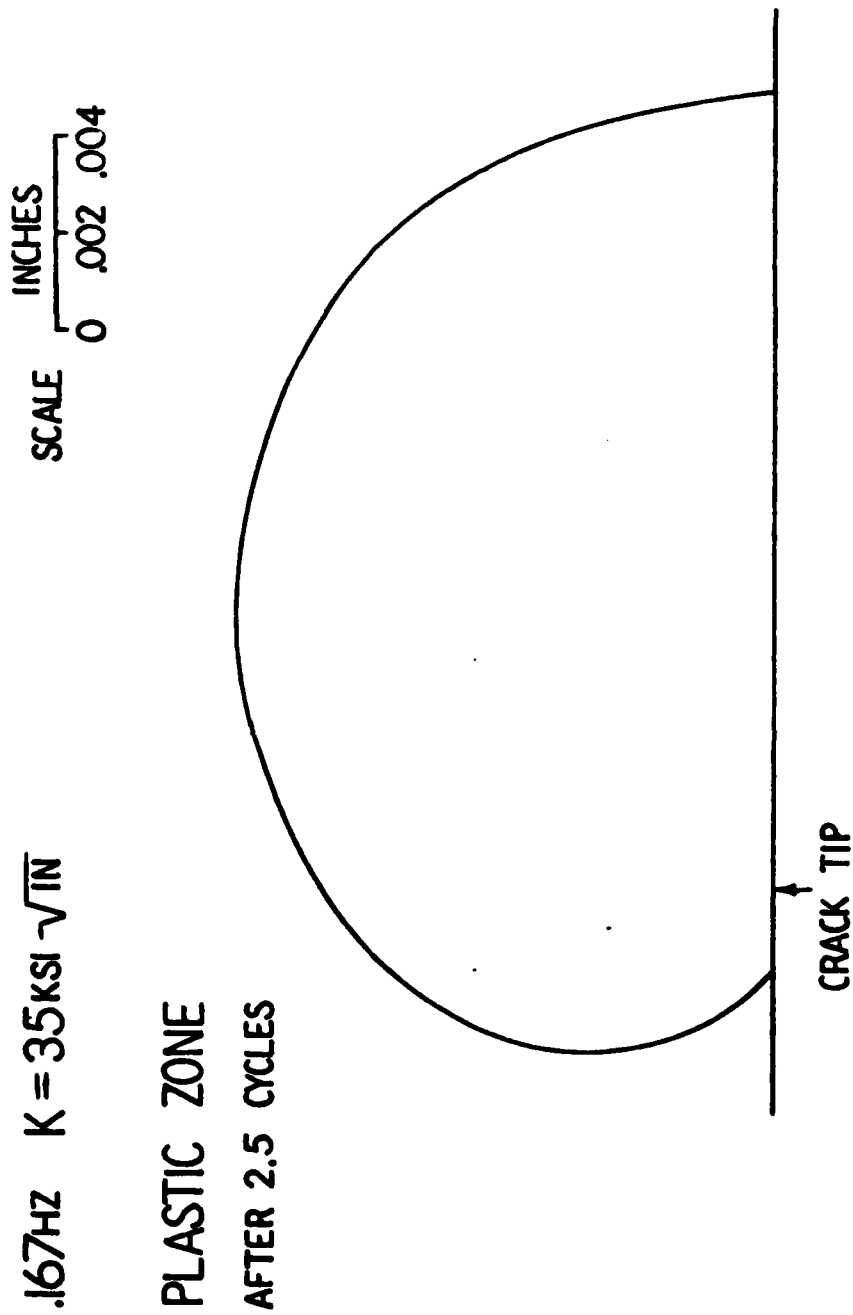


Fig 4.58 Plastic Zone After 2.5 Cycles

.167 Hz $K=35\text{KSI}\sqrt{\text{In}}$

.03HZ $K=35\text{KSI}\sqrt{\text{IN}}$

PLASTIC ZONE
AFTER 0.5 CYCLES

SCALE
INCHES
0 .002 .004

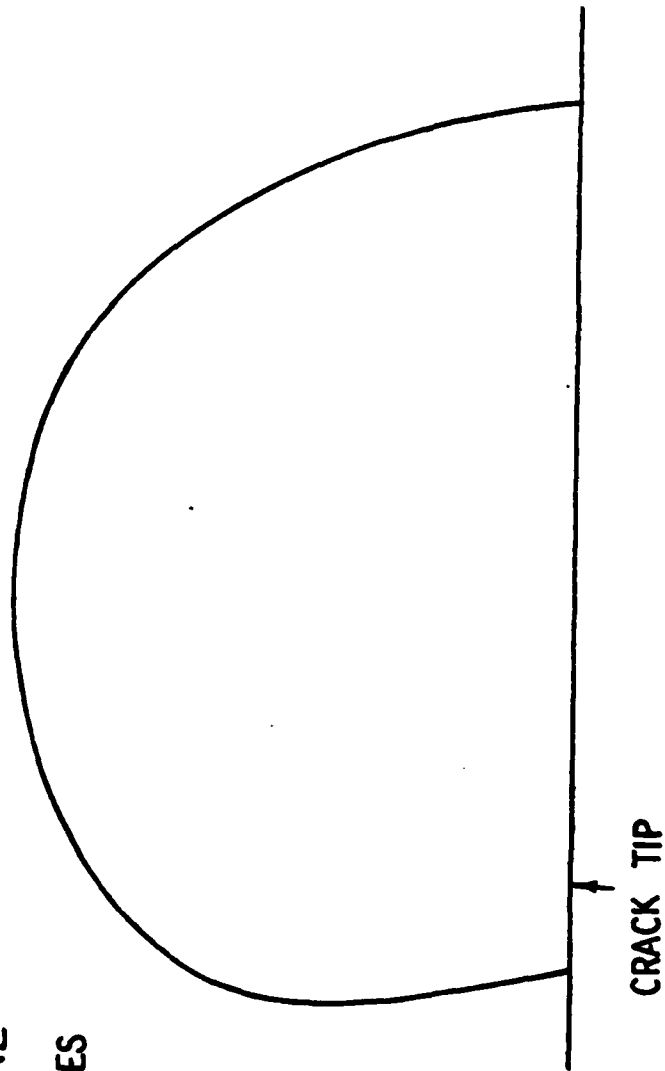


Fig 4.59 Plastic Zone After 0.5 Cycles .03 Hz

$$K=35\text{KSI}\sqrt{\text{IN}}$$

.03HZ $K = 35 \text{ KSI} \sqrt{\text{IN}}$

PLASTIC ZONE
AFTER 2.5 CYCLES

SCALE INCHES
0 .002 .004

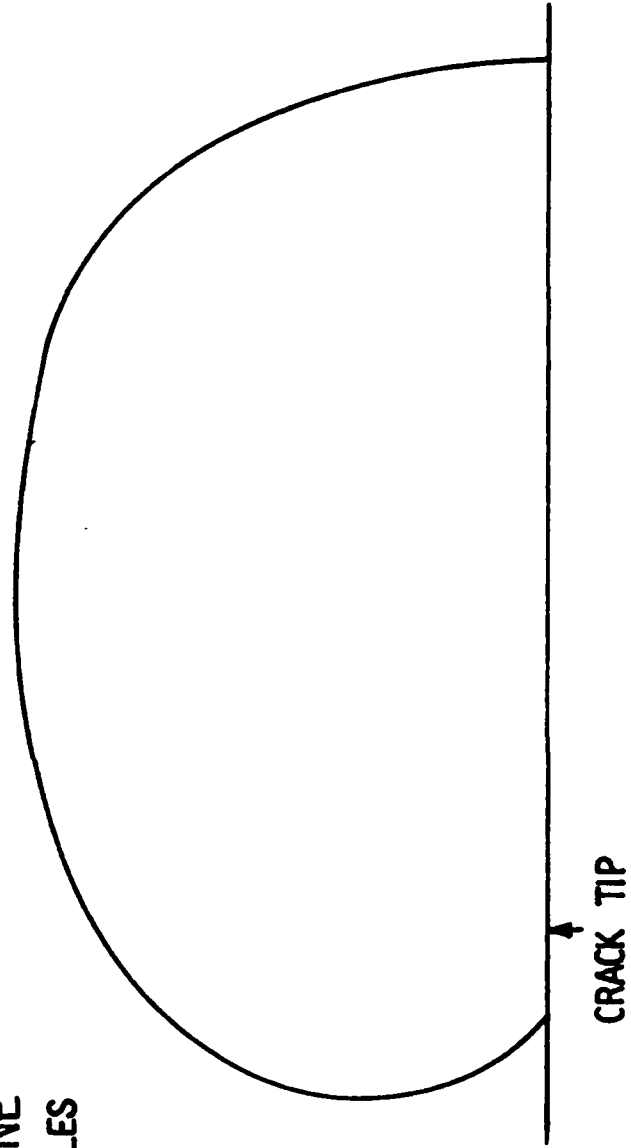


Fig 4.60 Plastic Zone After 2.5 Cycles .03Hz

$$K = 35 \text{ KSI} \sqrt{\text{IN}}$$

stress intensity factors. The results show (Fig's. 4.61-4.64) that the compact tension specimen behaves elastically at points on the specimen boundary and does not see the localized inelastic behavior near the crack tip.

To check the finite element compliance data, elastic modulus (E) calculations were made using compliance data from Fig's. 4.61-4.64, and the load and crack length data from Table 3.2 with the experimentally derived equation (5.1) for elastic compliance calculations for a compact tension specimen [16]:

$$\frac{27.2}{BC} = E \quad (5.1)$$

where B is the specimen thickness, C is the compliance and E is the elastic modulus for the material. Using the specimen thickness of .2154 inches and compliance of 4.4842×10^{-6} in/lb, the calculated modulus was 28.1×10^6 PSi. By comparing the calculated elastic modulus to the experimental elastic modulus (Table 2.1), it can be seen that the calculated elastic modulus is 7 percent greater than experimentally determined elastic modulus.

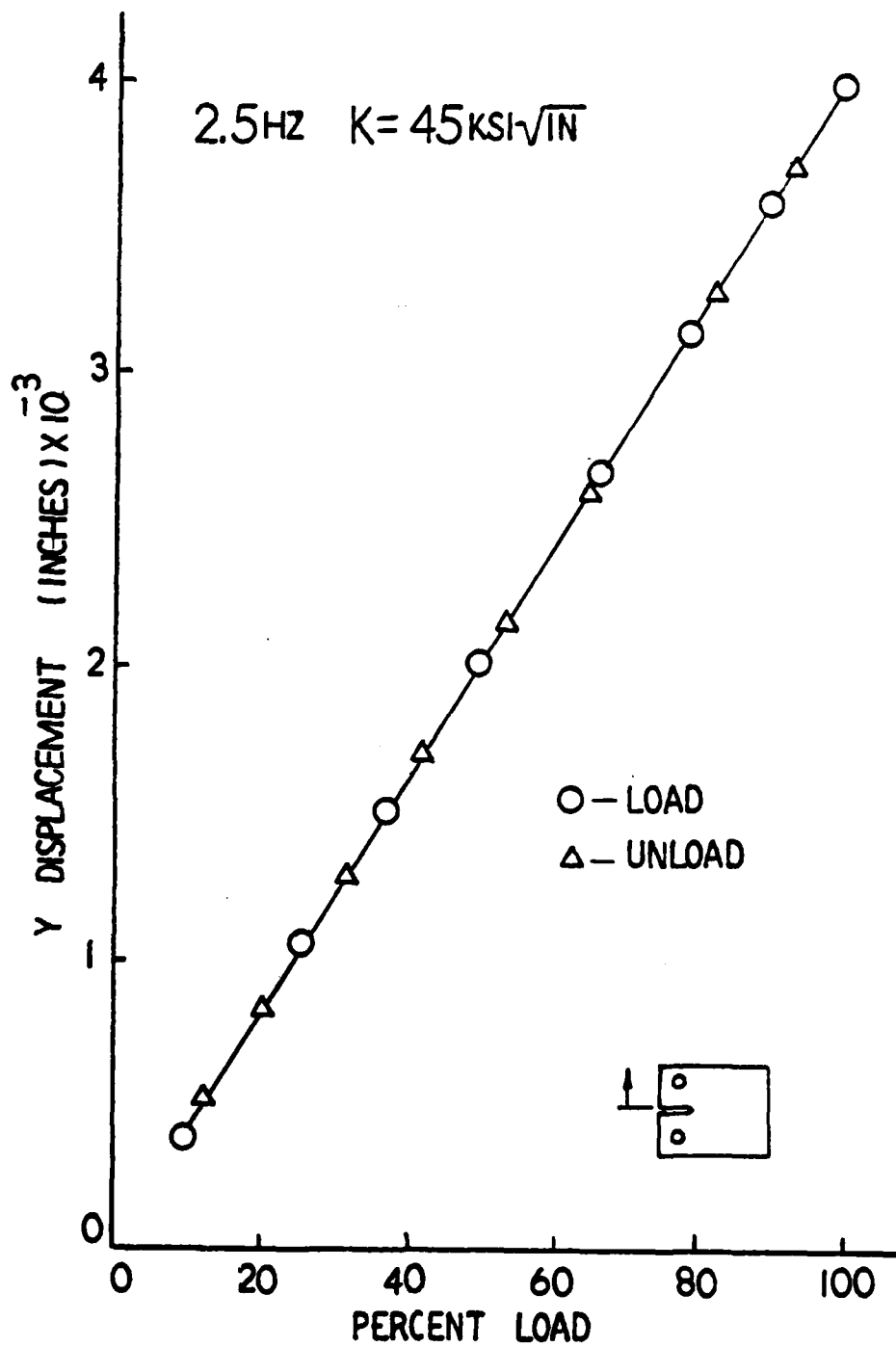


Fig 4.61 Crack Mouth Displacement vs Percent Load

2.5Hz $K=45\text{KSI}\sqrt{\text{IN}}$

Normalized to $K=35\text{KSI}\sqrt{\text{IN}}$

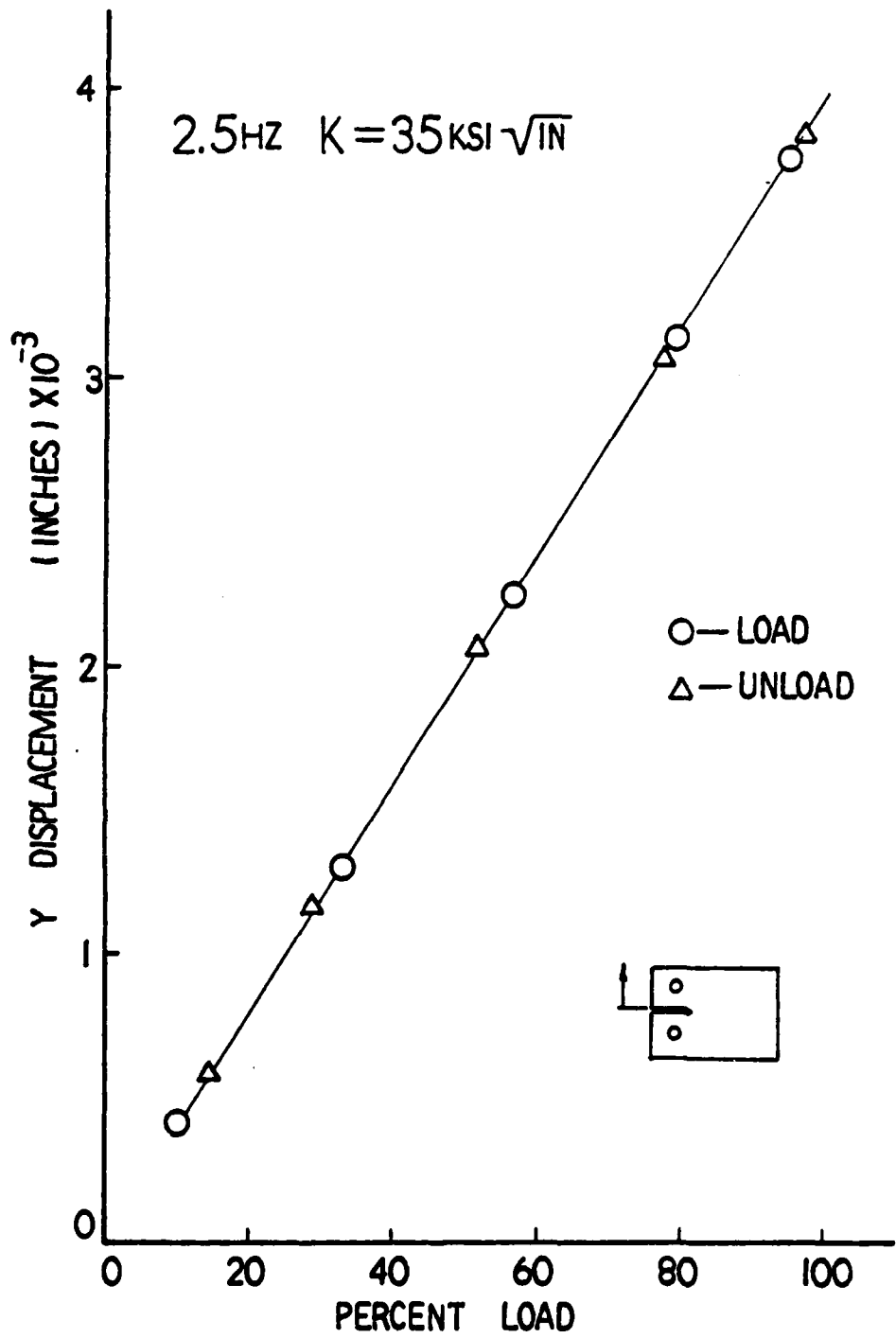


Fig 4.62 Crack Mouth Displacement vs Percent Load

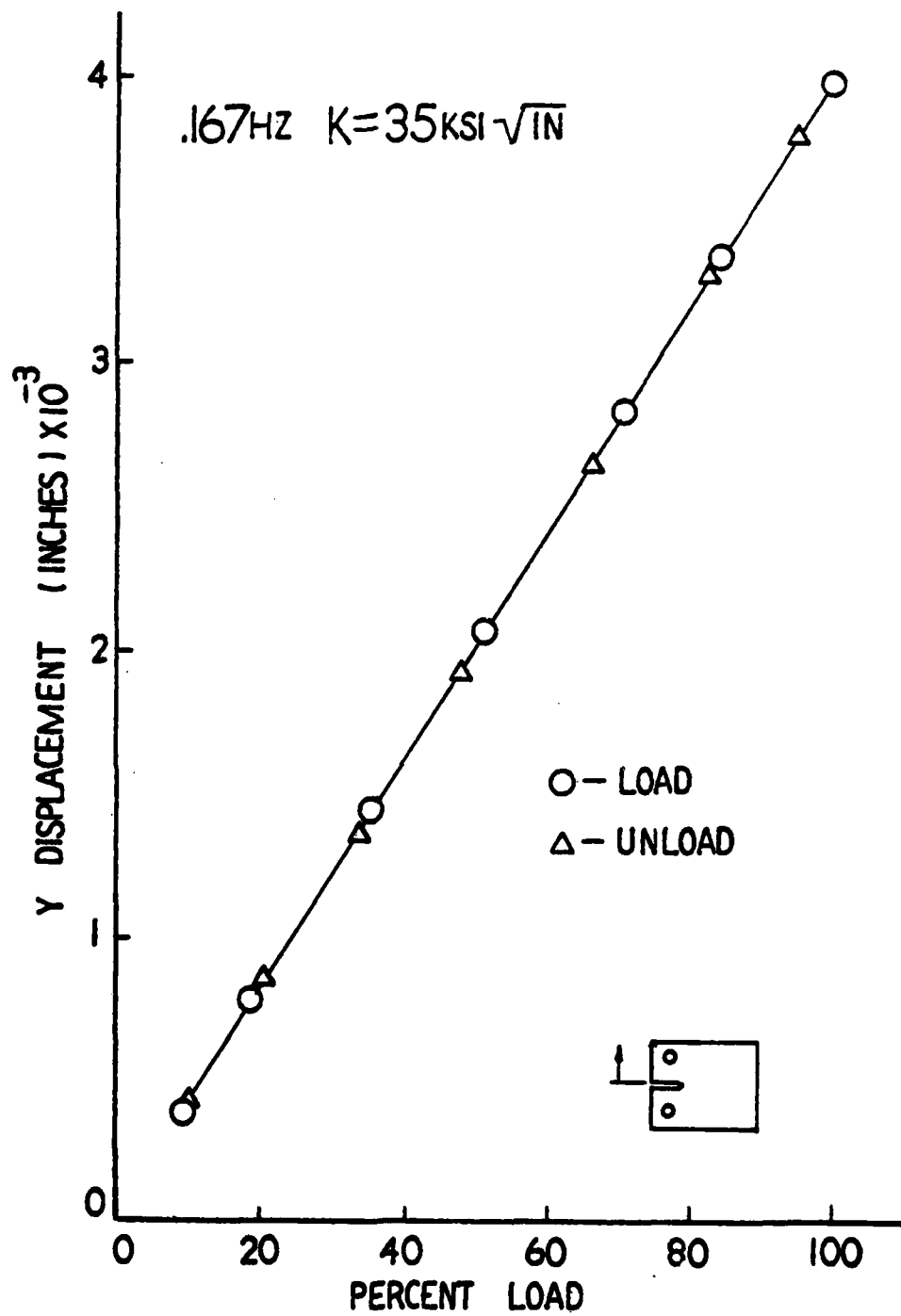


Fig 4.63 Crack Mouth Displacement vs Percent Load

.167Hz $K=35\text{KSI}\sqrt{\text{in}}$

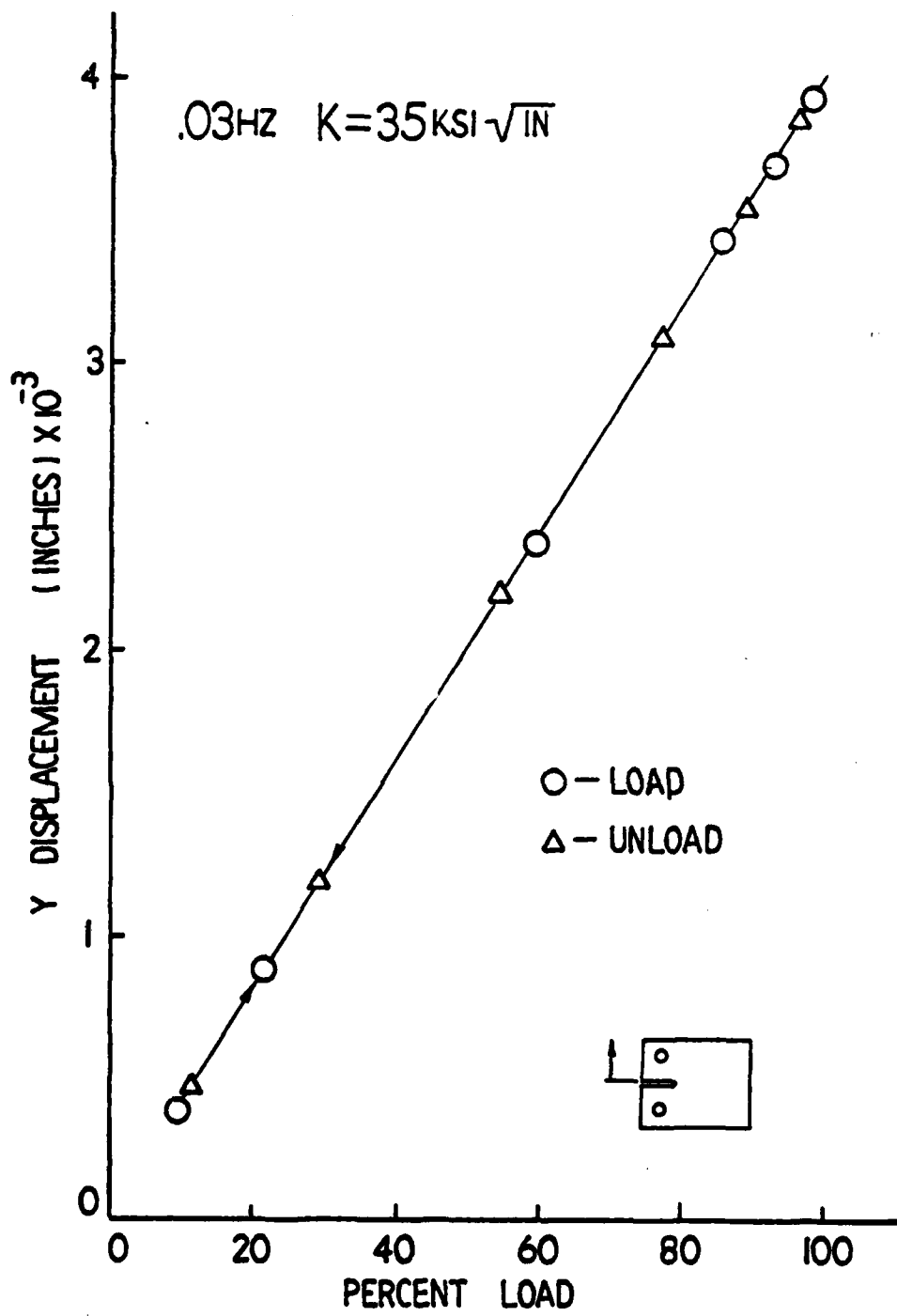


Fig 4.64 Crack Mouth Displacement vs Percent Load

V. CONCLUSIONS

The foregoing computations are based on the Bodner constitutive equations which model the real behavior on IN-100 at elevated temperatures in which experimental tests have been made. Computations show that this material has a significant amount of time dependent inelastic behavior as evidenced by computational results for both uniaxial and compact tension specimens.

1. There is close correlation between uniaxial cyclic behavior and the material behavior near the crack tip.
2. At frequencies above .167Hz and at stress levels below 165KSI, inelastic behavior is negligible with respect to total material behavior for both uniaxial and compact tension tests.
3. At high stress levels,(independent of frequency) large amounts of plastic deformation occur in the first load cycle. Subsequent load cycles produce constant amounts of plastic deformation per cycle.
4. The stress field and plastic zone size ahead of the crack tip remains relatively constant after one to three load cycles in the compact tension geometry.
5. Linear Elastic Fracture Mechanics overestimates the stress field directly ahead of the crack tip and underestimates it at larger distances.

6. The stress field ahead of the crack tip becomes more uniform during sustained hold periods.
7. The size of the plastic zone remains relatively constant during sustained hold periods.
8. After node release from a sustained hold period, the size of the plastic zone ahead of a crack tip remains essentially constant and only shifts forward to the new crack tip.
9. The size of the plastic zone after cycling is frequency and load dependent. For a given load, the plastic zone increases in size as the frequency decreases.
10. The cyclic behavior near the crack tip for compact tension geometry is stress controlled.
11. The far field overall behavior of the compact tension specimen is elastic and independent of frequency and load level.

Bibliography

1. Collins, J.A., Failure of Materials in Mechanical Design, New York: John Wiley & Sons, 1981.
2. Harris, J.A., Jr., Sims, D.L., Annis, C.G., Jr., "Concept Definition: Retirement for Cause of F-100 Rotor Components," AFWAL-TR-80-4118, Wright-Patterson AFB, Ohio, 1980.
3. Bodner, S.R., and Partom, Y., "Constitutive Equations for Elastic-Viscoplastic Strain Hardening Materials," Journal of Applied Mechanics Trans., 42: 385-389 (1975).
4. Bodner, S.R., "Representation of Time Dependent Mechanical Behavior of Rene 95 By Constitutive Equations," AFML-TR-79-4116, Wright-Patterson AFB, Ohio, 1979.
5. Stouffer, D.C, and Bodner, S.R., "A Relationship Between Theory and Experiment for a State Variable Constitutive Equation," AFWAL-TR-80-4194, Wright-Patterson AFB, Ohio, 1981.
6. Stouffer, D.C., "A Constitutive Representation for IN-100," AFWAL-TR-81-4039, Wright-Patterson AFB, Ohio, 1981.
7. Hinnerichs, T.D., "Viscoplastic and Creep Crack Growth Analysis by the Finite Element Method," PhD Dissertation, Department of Aeronautics and Astronautics, Air Force Institute of Technology, Wright-Patterson AFB, Ohio, 1980.
8. Zienkiewicz, O.C., The Finite Element Method (Third Edition), Chapter 24, pp. 724-726, New York: McGraw-Hill Book Company, 1977.

Bibliography (Cont'd.)

9. Bridgman, P.W., "The Effect of Hydrostatic Pressure on the Fracture of Brittle Substances," Journal of Applied Physics, 18: 246 (1947).
10. Bridgman, P.W., Studies in Large Plastic Flow and Fracture with Special Emphasis on the Effects of Hydrostatic Pressure, New York: McGraw-Hill Book Company, 1952.
11. Rolfe, S.T., and Barsom, J.M., Fracture and Fatigue Control in Structures, Chapter 2, pp. 30-47, Englewood Cliffs, NJ: Prentice-Hall Inc., 1977.
12. Ugural, A.C., and Fenster, S.K., Advanced Strength and Applied Elasticity, Chapter 12, pp. 363-364, New York: Elsevier North Holland Publishing Co., Inc., 1975.
13. Owen, D.R.J., and Hinton, E., Finite Elements in Plasticity Theory and Practice, Chapter 7, pp. 215-270, Swansea, U.K.: Pineridge Press Limited, 1980.
14. Larsen, J.M. and Nicholas, T., "Load Sequence Crack Growth Transients in a Superalloy at Elevated Temperature," Presented at the 14th National Symposium of Fracture Mechanics, July, 1981, Los Angeles, CA. To be published in ASTM STP.
15. Smail, J.W., "The Viscoplastic Crack Growth Behavior of a Compact Tension Specimen Using the Bodner-Partom Flow Law," Master of Science Thesis, Dept of Aeronautics and Astronautics, Air Force Institute of Technology, Wright-Patterson AFB, Ohio, December 1981.

Bibliography (Cont'd.)

16. Hudak, S.J., Jr., et. al., "Development of Standard Methods of Testing and Analyzing Fatigue Crack Growth Rate Data," AFWAL-TR-78-40, Wright-Patterson AFB, Ohio, May 1978.

Appendix A

The computer program VISCO was modified for cyclic loading by adding a subroutine named CYCLIC and appropriate call statements in the Load Subroutine. CYCLIC uses a constant sloped ramp to simulate the input. The slope of the ramp is computed using the half-cycle period of the input frequency. A local time variable is used to locate position on the input cycle. At the peak load the slope is reversed and the local time frame shifted to the input peak. During each timestep, (passed from the main program) subroutine CYCLIC calculates the percentage of total load. The calculated load percentage is then passed back to the Load Subroutine. Nodal loads were computed and used to calculate appropriate displacements, and stresses and strains. The process is repeated for each timestep.

Variables read into the program in statements labeled one and two control load cycling and stop times.

The variable STOPCY is the time variable used to stop load cycling. NC dictates whether subroutine CYCLIC is called from the Load Subroutine (statement labeled 3). If NC equals one, cyclic loads are applied. Any other number causes a monotonic load to be applied. Variables PMAX, P0, and PERIOD control the input load cycle. PMAX is the peak load percentage (100%), while P0 is the stress ratio for the load cycle. The variable PERIOD is the cycle period of the input frequency in seconds.

PROGRAM WILSON(INPUT=0,OUTPUT=0,TAPE5=INPUT,TAPE6=OUTPUT,TAPE7=1,
1TAPE=,TAPE1,TAPE2,TAPE3,TAPE4,TAPE3)

C
C FINITE ELEMENT ANALYSIS PROGRAM OF TWO DIMENSIONAL
C PLANE STRESS & PLANE STRAIN OPTIONS
C GAUSS-SEIDEL ITERATION SOLUTION ROUTINE
C ELEMENT NODES I,J,K, MUST BE NUMBERED COUNTER CLOCKWISE
C DIMENSION AND COMMON STATEMENTS
C

COMMON /A/AREA(543)
COMMON /NPIV/DXX(327,9),DXY(327,9),SYX(327,9),DYY(327,9)
COMMON /HC/HP(327),NPIV(327),SLOPE(327)
COMMON /AP/AP/NP(543,9),AP(327)
COMMON /DISPL/DX(327),DXY(327)
COMMON /LOAD/XLOAD(327),YLOAD(327),FX(10),FY(10),F,FRATE,WF(10)
COMMON /MAT/MAT/KORD(327),YORD(327),NPI(543),NPJ(543),NPK(543)
COMMON /STRESS/DSIGXX(543),DSIGXY(543),DSIGYY(543),DSIGZZ(543)
COMMON /TCL/DSIGXX(543),DSIGXY(543),DSIGYY(543),DSIGZZ(543)
COMMON /VISCO/EVPX(543),EVPY(543),EVPZ(543),EPEFF(543),
1OPEFF(543)
COMMON /D/DX(543),DY(543),DXY(543),DT(543)
COMMON /WCPK/WPP(543),WPC(543),WPE(543)
COMMON /PROP/ET(543),XU(543),T4(543),PS,MAT
COMMON /JINT/JEL(10),JL(10,543),KN(10,543),YV(10,543),CJINT,JPATH
COMMON /BODVER/DZ2,EN,Z1,Z0,ZI,EMO,PN,AC
COMMON /CFACK/ICR,ICR,ICP(29),SXXC(29),SYXC(29),
1SYXC(29),TOL(29),YLD(29)
COMMON /COSTA/DXDT(327),DYDT(327),DDT
COMMON/HARD/HKPLAS(543)
DIMENSION L*(3),B(6,6),D(6,6),S(6,6)

C
C READ AND PRINT OF DATA
C

WRITE(6,99)
READ(5,*)NDATA,MESHE,MESHN,MESHOLD,TCL,MPRINT
PRINT(6,*)"NUMBER OF MESH DATA SETS=",NDATA
PRINT(6,*)"ADDED ELEMENTS=",MESHE,"ADDED NODES=",MESHN
PRINT(6,*)"OLD ELEMENTS REUSED=",MESHOLD
PRINT(6,*)"PLOT SCALE FACTOR IS ",SCAL
READ(5,*)PS,MAT
IF(PS.EQ.0)PRINT(6,*)"PLANE STRESS SOLUTION"
IF(PS.GT.0)PRINT(6,*)"PLANE STRAIN SOLUTION"
IF(MAT.EQ.0)PRINT(6,*)"VISCOS SUBROUTINE BEING USED"
IF(MAT.GT.0)PRINT(6,*)"BODVER'S SUBROUTINE BEING USED"
IF(MAT.GT.0)READ(5,*)DZ2,EN,Z1,Z0,ZI,EMO,PN,AC
IF(MAT.GT.0)PRINT(6,*)"DZ2=",DZ2,"EN=",EN,"Z1=",Z1,"Z0=",Z0,
1"ZI=",ZI,"EMO=",EMO,"PN=",PN,"AC=",AC
READ(5,*)NUMHC,NCPIN,NOPIN,NCYC,TOL,XFAC
WRITE(6,103)NUMHC
WRITE(6,104)NCPIN
WRITE(6,105)NOPIN
WRITE(6,106)NCYC
WRITE(6,107)TOL
WRITE(6,108)XFAC
READ(5,*)VP,YIELD,HP,VC,ALPHA,RAN,BERG,DTINIT,DTMAX,TMAX
DT=DTINIT
① READ(5,*)TPRINT,STORCY,XMOVE1,XMOVE2,TMOVES

```

2 READ (5,*)INC,PMAX,PC,PERIOD)
PRINT(6,*)"CYCLIC LOAD CODE: 1=IN;0=OUT, IN USE ",NC
PRINT(6,*)"CYCLIC MAX AMPLITUDE OF LOAD REQUIRED ",PMAX
PRINT(6,*)"STATIC AMPLITUDE ",PO
PRINT(6,*)"CYCLIC PERIOD VALUE IN SECONDS ",PERIOD
PRINT(6,*)"FLUIDITY CONSTANT= ",VP
IF(MAT .EQ. 1)PRINT(6,*)"YIELD= ",YIELD," PLASTIC SLOPE= ",MP
PRINT(6,*)" CREEP EXPONENT=",ALPHA," CREEP COEFF=",VC
PRINT(6,*)"RAMBERG-OSGD COEFF=",RAM,"RAMBERG-OSGD EXPON=",BERG
PRINT(6,*)"TIME STEP= ",DT
PRINT(6,*)"MAXIMUM TIMESTEP=",DTMAX
PRINT(6,*)"PRINT TIME= ",YPRINT
PRINT(6,*)"MAX TIME = ",TMAX
READ(5,*)STRLES,TEPS,VM,PE,SLOPEA
PRINT(6,*)"STRAIN TOLERANCE IS ",TEPS
PRINT(6,*)"STRESS TOLERANCE IS",TSTRESS
N=1
CALL MESH(NUMNP,NUMEL,NDATA,SCAL,MESHE,MESHN,MPRINT,MESHOLD)
WRITE(6,112)
- EAD(5,4)(NPH(L),NFX(L),SLOPE(L),L=1,NUMBC)
WRITE(6,4)(NPB(L),NFX(L),SLOPE(L),L=1,NUMBC)
- EAD(5,*)NF,FRATE,NODE,OPE,CEPT,RT,CONV
PRINT(6,*)" LOADED NODES=",NF," FORCE RATE=",FRATE
PRINT(6,*)" NODE PT OF INTEREST=",NODE,"SLOPE=",OPE
PRINT(6,*)" TIME CONVERSION FOR SHARP=",CONV
PRINT(6,*)" INTERCEPT=",CEPT,"RELEASE TIME=",RT
PRINT(6,*)"MALVERN VERSION CODE LINE=-1,EXP=0,POW=+1. IN USE ",VM
PRINT(6,*)"POWER VERSION EXPONENT VALUE IS",PE
PRINT(6,*)"THE A VALUE USED IN EXPMALVERN IS",SLOPEA
- EAD(5,*)(NFA(I),I=1,NF)
PRINT(6,*)"LOADED NODES=",NFA(I),I=1,NF)
DO 40 I=1,NF
J=NFA(I)
- EAD(5,*)FX(I),FY(I)
40 PRINT(6,*)"NODE ",J," XLOAD=",FX(I)," YLOAD=",FY(I)
- EAD(5,*)ICR,"CRACK(I)
PRINT(6,*)"THE NUMBER OF NODES TO BE CRACKED=",ICR
IF (ICR .EQ. 0)GO TO 940
DO 200 I=1,ICR
READ(5,*)(ICR(I,K),K=1,4)
200 PRINT(6,*)(ICR(I,K),K=1,4)
- EAD(5,*)(TCRACK(I),I=1,ICR)
DO 930 I=1,ICR
PRINT(6,*)"NODE ",ICR(I,1),"POPS AT TIME ",TCRACK(I)
930 CONTINUE
940 CONTINUE
- EAD(5,*)JPATH
PRINT(6,*)"NUMBER OF J INTEGRAL PATHS=",JPATH
IF (JPATH .EQ. 0)GO TO 910
DO 900 I=1,JPATH
- EAD(5,*)JEL(I)
PRINT(6,*)"NUMBER OF ELEMENTS IN PATH",I,"EQUALS",JEL(I)
M=JEL(I)
- EAD(5,120)(JN(I,K),XN(I,K),YN(I,K),K=1,M)
120 FORMAT(15,2E10,2)
DO 905 K=1,M
905 PRINT(6,*)"JN=",JN(I,K)," XN= ",XN(I,K)," YN= ",YN(I,K)

```

```

SUBROUTINE LOAD (NT, T, NUMEL, NUMNP, PI, AT, P*AX, P2, PERIOD, C,
1 CYCNO, STPCY)
COMMON /LOAD/ XLOAD(327), YLOAD(327), FX(13), FY(10), F, FRATE, FA(10)
COMMON /MAT/ XCRD(327), YCRD(327), MPI(543), NPJ(543), PK(543)
COMMON /VISC/ EVPX(543), EVPXY(543), EVPY(543), EVZ(543), EPEFF(543),
1 DPEFF(543)
COMMON /PROP/ ET(543), XU(543), TH(543), PS, *AT
COMMON /CRACK/ ICR, ICRP, ICP(29,4), SXXC(29), SYXC(29), SYXC(29),
1 SYXC(29), *CRACK(29), YLOAD(29)
DIMENSION D(6,6), B(6,6)
DO 100 L=1, NUMNP
XLOAD(L)=0.
100 YLOAD(L)=0.
IF (ICR .EQ. 0) GO TO 300
IM=ICRP-1
IF (IM .LE. 0) GO TO 300
M=NC*(IM,1)
DO 200 L=1, NUMNP
IT=*CRACK(IM)+AT-T
IF (L .EQ. M) YLOAD(L)=YLOAD(IM)+IT/(AT)
IF (L .EQ. M .AND. IT .LT. 0) YLOAD(L)=0.
IF (L .EQ. M) P=INT(6,*)*YLOAD "L" EQUALS "L", YLOAD(L)
200 CONTINUE
300 CONTINUE
IF (T.EQ.0.0) T=0.001
P=FRATE*T
PP=P+PI
IF (PP .GT. 1.) PP=1.

IF (T.GE. STPCY) GO TO 25
IF (NC.EQ.1) CALL CYCLIC (T, P*AX, P2, PERIOD, PP, CYCNO)
PRINT(6,*) PP= "PP"
25 IF (T.GE. STPCY) PP=1.
DO 110 I=1, N
J=NFA(I)
XLOAD(J)=FX(I)+PP
110 YLOAD(J)=FY(I)+PP
DO 10 N=1, NUMEL
IF (EPEFF(N) .EQ. 0.) GO TO 13
I=MPI(N)
J=NPJ(N)
K=NPK(N)
CALL DMATRIX(N, J)
SX=D(1,1)*EVPX(N)+D(1,2)*EVPY(N)
SY=D(2,1)*EVPX(N)+D(2,2)*EVPY(N)
SKY=D(3,3)*EVPXY(N)
CALL BMATRIX(N, H)
XLOAD(I)=XLOAD(I)+H(1,1)*SX+H(2,1)*SY+H(3,1)*SKY
YLOAD(I)=YLOAD(I)+H(1,2)*SX+H(2,2)*SY+H(3,2)*SKY
XLOAD(J)=XLOAD(J)+H(1,3)*SX+H(2,3)*SY+H(3,3)*SKY
YLOAD(J)=YLOAD(J)+H(1,4)*SX+H(2,4)*SY+H(3,4)*SKY
XLOAD(K)=XLOAD(K)+H(1,5)*SX+H(2,5)*SY+H(3,5)*SKY
YLOAD(K)=YLOAD(K)+H(1,6)*SX+H(2,6)*SY+H(3,6)*SKY
10 CONTINUE
RETURN
END

```

```

SUBROUTINE CYCLIC (T,PMAX,P0,PERIOD,PP,CYCNO)
PRINT(6,*)"IN CYCLIC SUBROUTINE"
PRINT(6,*)"T=      ",T,"PERIOD=    ",PERIOD
TLOC=T-INT(T/PERIOD)*PERIOD
IF(TLOC.LE.PERIOD/2.0) PP=TLOC/(PERIOD/2.0)*(PMAX-P0)+P0
IF(TLOC.GT.PERIOD/2.0) PP=(PERIOD-TLOC)/(PERIOD/2.0)*(PMAX-P0)+P0
PRINT(6,*)"% LOAD=    ",PP,"AT TIME    ",T
CYCNO=T/PERIOD
PRINT(6,*)"NUMBER OF LOAD CYCLES=    ",CYCNO
PRINT(6,*)"LEAVE CYCLIC SUBROUTINE"
RETURN
END

```

VITA

James E. Keck was born on 12 March 1947 in Kansas City Missouri. He graduated from Shawnee Mission North High School in 1965 and attended Kansas State University, where he received his B.S. in Mechanical Engineering. Upon graduation he was commissioned as a second lieutenant in the USAF. He attended undergraduate pilot training at Vance AFB, Oklahoma earning his wings in September 1971. He then served as a KC-135 pilot, aircraft commander, instructor pilot and wing flying safety officer for the 100th Air Refueling Wing, Beale AFB, California until June 1979. He was then transferred to Grand Forks AFB, North Dakota where he served as a KC-135 standardization/Evaluation Instructor Pilot for the 319th Bombardment Wing. He entered the School of Engineering, Air Force Institute of Technology in June 1981.

Permanent address: 5229 Delrey

Las Vegas, NV 89102

REPORT DOCUMENTATION PAGE		READ INSTRUCTIONS BEFORE COMPLETING FORM
1. REPORT NUMBER AFIT/GAE/AA/82D-17	2. GOVT ACCESSION NUMBER A124 68A	3. RECIPIENT'S CATALOG NUMBER
4. TITLE (and Subtitle) The High Temperature Viscoplastic Fatigue Behavior of a Compact Tension Specimen Using the Bodner-Partom Flow Law		5. TYPE OF REPORT & PERIOD COVERED MS Thesis
7. AUTHOR(s) James E. Keck Major USAF		6. PERFORMING ORG. REPORT NUMBER
9. PERFORMING ORGANIZATION NAME AND ADDRESS Air Force Institute of Technology (AFIT/EN) Wright-Patterson AFB, Ohio 45433		8. CONTRACT OR GRANT NUMBER(s)
11. CONTROLLING OFFICE NAME AND ADDRESS Air Force Institute of Technology (AFIT/EN) Wright-Patterson AFB, Ohio 45433		10. PROGRAM ELEMENT, PROJECT, TASK AREA & WORK UNIT NUMBERS
14. MONITORING AGENCY NAME & ADDRESS (if different from Controlling Office)		12. REPORT DATE December 1982
		13. NUMBER OF PAGES 118
		15. SECURITY CLASS. (of this report) Unclassified
		15a. DECLASSIFICATION/DOWNGRADING SCHEDULE
16. DISTRIBUTION STATEMENT (of this Report) Approved for public release; distribution unlimited.		
17. DISTRIBUTION STATEMENT (of the abstract entered in Block 20, if different from Report)		
18. SUPPLEMENTARY NOTES <p style="text-align: right;">Approved for public release; LAW AND LYNN E. WOLVER Dean for Research and Professional Development Air Force Institute of Technology Wright-Patterson AFB, Ohio 45433</p> <p style="text-align: left;">JAN 1983</p> <p style="text-align: center;">Wright-Patterson AFB OH 45433 Air Force Institute of Technology (AFIT) Dean for Research and Professional Development LYNN E. WOLVER</p>		
19. KEY WORDS (Continue on reverse side if necessary and identify by block number) Viscoplasticity Bodner-Partom Flow Law Finite Element Modeling		
20. ABSTRACT (Continue on reverse side if necessary and identify by block number) Few studies have been made concerning the effects of low cycle fatigue on the stress/strain field or the plastic zone size ahead of a crack tip in a high temperature environment. Experiments using a superalloy IN-100 at 732°C have shown crack growth during fatigue is slower than the growth rate during long periods of sustained load. These investigations also show that crack growth rates during hold periods after fatigue cycling are dependent on the cycle frequency.		

This study focuses on fatigue as it effects the changing stress field and plastic zone ahead of a crack tip. Finite element modeling was accomplished using an in-house computer program named VISCO, which was modified to incorporate load cycling. A compact tension specimen geometry was modeled using the Bodner-Partom viscoplastic constitutive equations to describe the material behavior. Load spectra consisted on constant amplitude saw toothed patterns with non-zero mean load having a ratio of minimum to maximum load of 0.1.

Results show that material behavior near a crack tip closely correlates to uniaxial material response data under stress controlled loading. During cyclic loading, the greatest plastic deformation near the crack tip occurs in the first load cycle. Computations show that IN-100 displays significant amounts of time dependent inelastic behavior.

3-8

DT